HARVARD UNIVERSITY
Graduate School of Arts and Sciences

DISSERTATION ACCEPTANCE CERTIFICATE

The undersigned, appointed by the

Department of Physics

have examined a dissertation entitled

Nanoscale Investigations of High-Temperature Superconductivity
in a Single Atomic Layer of Iron Selenide

presented by Dennis Huang

candidate for the degree of Doctor of Philosophy and hereby certify that it is worthy of acceptance.

Signature ____
Typed name: Professor Jenny Hoffman, Chair

Signature ____
Typed name: Professor Efthimios Kaxiras

Signature ____
Typed name: Professor Philip Kim

Date: April 19, 2016

Nanoscale Investigations of High-Temperature Superconductivity in a Single Atomic Layer of Iron Selenide

A DISSERTATION PRESENTED
BY
DENNIS HUANG
TO
THE DEPARTMENT OF PHYSICS

IN PARTIAL FULFILLMENT OF THE REQUIREMENTS
FOR THE DEGREE OF
DOCTOR OF PHILOSOPHY
IN THE SUBJECT OF
PHYSICS

HARVARD UNIVERSITY
CAMBRIDGE, MASSACHUSETTS
APRIL 2016

Thesis advisors: Jennifer E. Hoffman, Efthimios Kaxiras Dennis Huang

Nanoscale Investigations of High-Temperature Superconductivity in a Single Atomic Layer of Iron Selenide

ABSTRACT

The potential of interface engineering to enhance electronic properties is exemplified in a single atomic layer of FeSe grown on $SrTiO_3$ [1], which exhibits an order-of-magnitude increase in its superconducting transition temperature (T_c up to 110 K [2]) compared to bulk ($T_c = 8$ K [3]). Since this discovery in 2012, efforts to reproduce, understand, and extend this finding continue to draw both excitement and scrutiny. In this thesis, we report the use of a combined molecular beam epitaxy (MBE) and scanning tunneling microscopy (STM) system to grow and image films of superconducting FeSe/$SrTiO_3$. In particular, we investigate and harness atomic defects in as-grown films to derive microscopic insights in two directions. First, we image quasiparticle interference (QPI) patterns generated around defects in order to reconstruct the electronic structure of the unperturbed system, and uncover pieces of the puzzle of high-T_c superconductivity in a monolayer of FeSe. Second, we characterize the atomic structure of defects using density functional theory (DFT), with possible implications on film quality and nanostructuring.

Contents

Listing of figures

Listing of tables

Citations to Previously Published Work

Chapter 2 is largely based on the following preprint:

> "Chromium tip etching and spin-polarized imaging of antiferromagnetic terraces in the bilayer manganite $La_{2-2x}Sr_{1+2x}Mn_2O_7$ ($x = 0.30$)", Stephen Liu*, Dennis Huang*, Ilija Zeljkovic, J. F. Mitchell, and Jennifer E. Hoffman, arXiv:1310.6733 (2013).

Chapter 3 will appear in the eighth volume of *Annual Review of Condensed Matter Physics*:

> "FeSe Monolayers", Dennis Huang and Jennifer E. Hoffman, Annu. Rev. Cond. Mat. Phys. **8**, XXX (2017).

Chapter 4 appears in its entirety as

> "Revealing the Empty-State Electronic Structure of Single-Unit-Cell FeSe/$SrTiO_3$", Dennis Huang, Can-Li Song, Tatiana A. Webb, Shiang Fang, Cui-Zu Chang, Jagadeesh S. Moodera, Efthimios Kaxiras, and Jennifer E. Hoffman, Phys. Rev. Lett. **115**, 017002 (2015).

Chapter 5 appears in its entirety as

> "Bounds on Nanoscale Nematicity in Single-Layer FeSe/$SrTiO_3$", Dennis Huang, Tatiana A. Webb, Shiang Fang, Can-Li Song, Cui-Zu Chang, Jagadeesh S. Moodera, Efthimios Kaxiras, and Jennifer E. Hoffman, Phys. Rev. B **93**, 125129 (2016).

Chapter 6 is under review as

> "Dumbbell Defects in FeSe Films: A Scanning Tunneling Microscopy and First-Principles Investigation", Dennis Huang, Tatiana A. Webb, Can-Li Song, Cui-Zu Chang, Jagadeesh S. Moodera, Efthimios Kaxiras, and Jennifer E. Hoffman, submitted (2016).

Acknowledgments

While the primary purpose of graduate school may be to receive training and perform scientific research, the people we meet and the relationships we develop are just as meaningful. To this end, I am grateful for all the mentors and companions that have helped me along the way.

First off, I would like to thank my advisor, Jennifer Hoffman, for being my strongest advocate, instilling confidence in me, and believing in my abilities more than I do myself. This became most apparent in my final year of graduate school, when Jenny gave me opportunities that are not usually available to graduate students to travel internationally in her place and develop some visibility in our field. I also appreciate Jenny for giving me the opportunity to learn a diverse set of techniques within her lab, forge my own research path with her guidance, and accomplish something of which I can be proud. Throughout the years, her words and actions have shown that she truly wants the best for each of her students, and I am very thankful for that.

I would also like to thank Efthimios Kaxiras for giving me a chance to learn DFT within his group and providing me a desk in his Cruft office spaces. Tim's expertise in a wide range of topics in solid-state physics was reflected in the diversity of his group, which provided a great learning atmosphere. I am also indebted to Tim's generosity in helping me arrange many of the administrative details in my final year of graduate school.

In the Hoffman lab, I have truly enjoyed working with all the members of the SPSTM/MBE-STM team. First is Ilija Zeljkovic, who showed me the ropes and taught me the important lessons of positive thinking and visualizing success (especially during sample transfers). He has remained a mentor since he left, always available for advice, and I'm sure he will do great things at Boston College. Next is Can-Li Song, who was instrumental in moving and setting up the new MBE extension to our STM. I am grateful for his perseverance and our eventual success in growing FeSe films. Then there are Jing Shi, Tatiana Webb, Harris Pirie, Jason Hoffman, and Mohammad Hamidian. I am especially grateful for all the hard work Tatiana has put in, working together with me to collect the FeSe data presented in this thesis. Given her talent, knowledge, and work ethics, I am sure she will bring the MBE-STM instrument to the next level.

Then there are the rest of the Hoffman lab members, whom I consider to be mentors and friends: Anjan Soumyanarayanan, Michael Yee, Yang He, Jason Zhu, Oliver Yam, and Pengcheng Chen from the STM1 team, and Adam Pivonka, Magdalena Huefner, Cun Ye, Martin Blood-Forsythe, Maoz Ovadia, Sarah Schlotter, and Eddie Ji from the SFM team. I'm grateful to have spent much time with Mike and Yang, who have provided so much support and comic relief throughout the years. All those dinners at Hong Kong and Le's and late nights in the labs will definitely be a memorable part of my graduate school experience.

In the Kaxiras group, I have to firstly thank Dogus Cubuk for being so hospitable, encouraging me to join the group, and getting me started with DFT and VASP. I also have to thank Shiang for showing so much interest and enthusiasm in our FeSe work, slugging through tight-binding models and QPI papers, sorting out minus signs, and helping develop the theoretical models presented in Chapter 5 of this thesis. Then there are the rest of my office mates in Cruft 402, who have made it a pleasant place to work: Rodrick Kuate, Wei Chen, Daniel Massatt, and Stephen Carr. I've also enjoyed being a part of the MURI collaboration on 2D materials, involving Georgios Tritsaris, Sharmila Shirodkar, Marios Matthaiakis, Paul Cazeaux and Mitchell Luskin, in addition to Shiang, Rodrick, Daniel, Stephen, and Tim. Working with mathematicians has truly been an interesting and fruitful experience. Finally, I have to thank the rest of the Kaxiras group members for making the group both a pleasant and intellectually-stimulating place to work: Brad Malone, Dmitry Vinichenko, Grigory Kolesov, Berk Onat, Oscar Granas, Matthew Montemore, Robert Hoyt, and Tian Lan.

In addition to the members of the Hoffman and Kaxiras groups, I'd like to thank Barbara Drauschke and Lisa Cacciabaudo for working tirelessly to take care of all my administrative needs. I'm also grateful to Jacob Barandes and Masahiro Morii for providing advice and moral support throughout the years. I also very much enjoyed my teaching experiences with Philip Kim, Matthew Schwartz and Cora Dvorkin. I have to especially thank Philip, as a committee member, for taking interest in my research career and offering plenty of advice.

Finally, I'd like to thank my friends from the Christian community, my parents Peter and Christine, and my brothers Jeffrey and John. Without your support, I could not be where I am today.

Part I

Instrumentation and Techniques

This part of the thesis is organized as follows: Chapter 1 describes the assembly of a molecular beam epitaxy and scanning tunneling microscopy system, used to grow and image thin films of superconducting FeSe on $SrTiO_3$. Chapter 2 describes ongoing efforts to perform spin-polarized scanning tunneling microscopy, using bulk antiferromagnetic Cr tips and magnetic bilayer manganites to characterize the tip spin polarization. Experiments investigating the effects of various etch parameters on the Cr tip apex geometry, as imaged by scanning electron microscopy, were carried out by an undergraduate researcher, Stephen Liu.

1

Assembly of a Molecular Beam Epitaxy and Scanning Tunneling Microscopy System

1.1 Overview

In this chapter, we outline the assembly of a combined molecular beam epitaxy and scanning tunneling microscopy (MBE-STM) system in 2013. Much credit goes to Dr. Can-Li Song, who designed the initial MBE interface and was involved with the assembly efforts.

We deconstructed an existing STM system (built by Elizabeth Main, Adam Pivonka, and Ilija Zeljkovic), repaired and modified various components, then reassembled the instrument in a larger floating room (double-wall soundproofed, six pressurized air springs) with sufficient clearance to fit a customized Lab10 MBE chamber from Omicron (Fig. 1.1). The entire process is documented in a set of slides that can be found on the lab FAS server: \\fas-home\hoffmanlab\SPSTM Working folder\Moving SPSTM and MBE installation 2013.

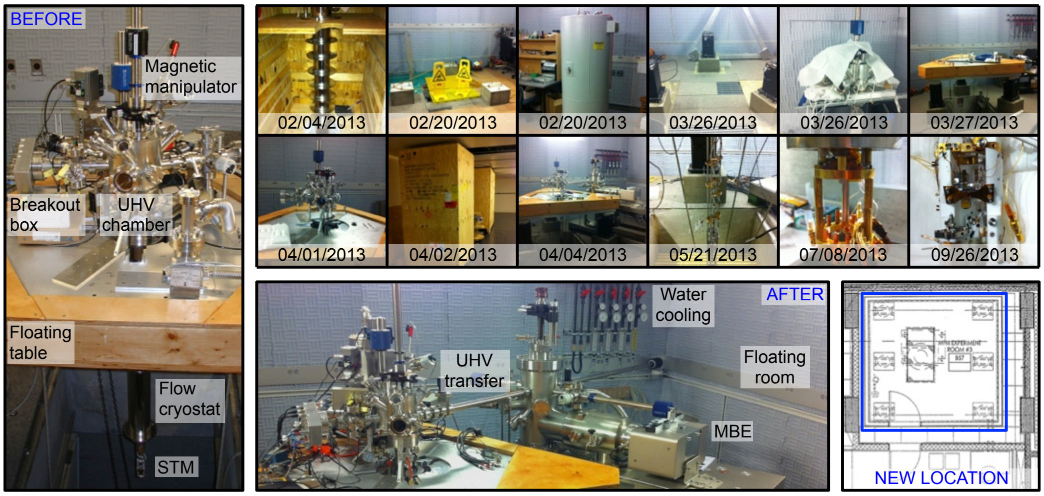

Figure 1.1: Assembly of a molecular beam epitaxy and scanning tunneling microscopy (MBE-STM) system in the Hoffman lab. The STM system was modified from a preexisting instrument built by Elizabeth Main, Adam Pivonka, and Ilija Zeljkovic (left panel). The MBE chamber is a customized Lab10 model from Omicron (bottom middle panel). The dated photos in the top right panel depict intermediate stages in the deconstruction, move, and assembly of the new system in a larger floating room (bottom right panel, basement of LISE building).

1.2 Scanning Tunneling Microscopy

Figure 1.2 presents a photo of the microscope head, designed and built by Elizabeth Main. Key components, including the sample tray holding the film of interest and an atomically-sharp tip for scanning, are labeled in the figure. The overall diameter of the microscope is constrained to be 1.7” in order for it to fit inside the bore of a magnet. Its design is inspired by models from the Wiesendanger group in Hamburg, Germany [4, 5]. Further details can be found in Elizabeth Main’s thesis [6], or in a set of updated slides on the lab FAS server: \\fas-home\hoffmanlab\SPSTM Working folder\MBE Lab Book.

The primary distinctive feature of the microscope is its rotating sample stage. It consists of a sapphire body with two polished conical ends, each pressed against three shear piezoelectric stacks. Rotation is actuated by stick-slip motion of the cones against the piezoelec-

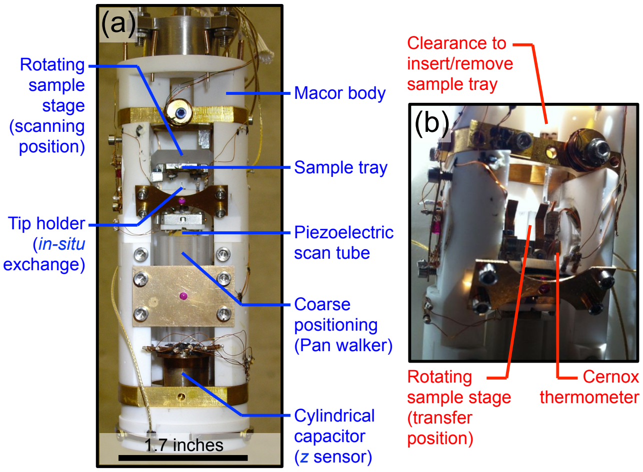

Figure 1.2: (a) Photo of the STM head, designed and built by Elizabeth Main (2010). Selected components and functionalities are highlighted. A scale bar is marked by a black line. (b) Updated photo of the microscope (2014), with a new Cernox thermometer installed to improve sample temperature readings.

tric stacks, and monitored by the overlap of concentric, half-cylindrical capacitor plates. In principle, the sample stage can be rotated to three positions, two of which are shown in Figs. 1.2(a) and (b):

1. *Sample tray horizontal, facing the tip* - this configuration is used for STM imaging.
2. *Sample tray vertical* - this configuration is used when exchanging either the sample or tip *in situ*, through a magnetic manipulator whose end piece enters the microscope head through a top clearance. For spin-polarized STM, this configuration also allows the sample and tip to be magnetized along orthogonal axes.
3. *Sample tray horizontal, facing away from the tip* - this configuration allows adatoms to be deposited on a cold film with the tip blocked from the line of sight.

In the original Wiesendanger design [4], a viewport afforded optical access of the rotating sample stage, at the cost of a higher cryogenic base temperature (~17 K). We lack optical access in our instrument (thus gaining a lower base temperature typically ~4.3 K), and have instead installed stoppers to limit the range the rotating sample stage between configurations (1) and (2).

To properly monitor the sample temperature, a thermometer needs to be mounted directly on the sapphire sample stage [5]. As part of the instrument upgrade, we installed a new Cernox thermometer on the right face of the rotating sample stage [Fig. 1.2(b)]. Care and testing were required to ensure that the extra leads from the thermometer did not add significant torque and impeding the rotary motion of the sample stage.

The STM head is suspended from a Janis flow cryostat (base temperature ∼2 K when pumping), which in turn is attached to a ultra-high-vacuum (UHV) chamber resting on a wooden table. The wooden table is filled with lead bricks (total ∼1 ton) and floated on three pressurized air springs to maximize vibration isolation. For cyrogenic imaging and spectroscopy, a dewar is hoisted up and bolted to the bottom side of the wooden table. During our instrument upgrade in 2013, we had the flow cryostat repaired of a leak, installed a new ruthenium oxide thermometer on the cryostat heat exchanger, installed a new ion getter pump (300 L/s pumping speed) for UHV operation, and modified our magnetic manipulator end piece to aid sample transfer.

1.3 Molecular Beam Epitaxy

Figure 1.3 presents a photo of a customized Lab10 MBE chamber from Omicron. Detailed documention can be found on the lab FAS server: \\fas-home\hoffmanlab\SPSTM Working folder\MBE manual, and \\fas-home\hoffmanlab\SPSTM Working folder\MBE-related.

The main modification to the commerical model involved redesigning the heating stage to accomodate a smaller sample tray, due to the small microscope head. We switched the sample tray material from Ti to Ta, a commonly-used refractory metal, for it to maintain structural integrity at elevated temperatures. Rather than gluing our growth substrate to the sample tray with some epoxy that could outgas when heated, we implemented a new clamping mechanism to fix the substrate to the sample tray. The present heating mechanism uti-

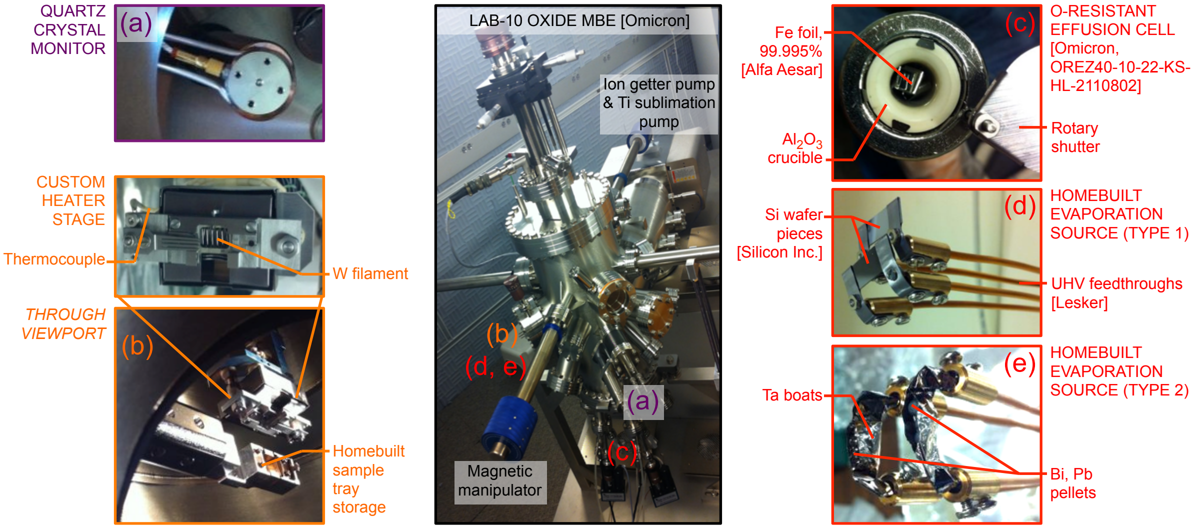

Figure 1.3: Photo of customized Lab10 MBE chamber from Omicron, with selected components and functionalities higlighted in panels (a)-(e).

lizes radiation from a W filament. More work, as well further modifications to the sample tray, are required to implement current-induced heating.

Presently, we have two oxygen-resistant effusion cells, holding elemental Fe and Se sources. This resistance enables a potential future upgrade of the chamber to grow oxide heterostructures. In addition, we have several homebuilt evaporation boats for Si (to flux-etch SiC) and various other metals (Bi, Pb, Sb, Cu, Ni, Co). Beam fluxes can be monitored by a water-cooled quartz crystal monitor, but ultimately we characterize a grown film through STM imaging.

Sample transfer throughout the MBE and into the STM is achieved through magnetic manipulators with keyhole and lock mechanisms. Two sample trays can be stored within the MBE, with base pressure down to 10^{-10} Torr. The present interface between the MBE and STM system involves nipples and bellows, which detract from the vibration isolation of the STM system, but is adequate as a temporary workaround.

Details related to film growth and imaging of FeSe thin films will be presented in later chapters.

2

Chromium Tip Etching and Non-UHV Spin-Polarized Imaging of Cleavable Materials

We report the preparation of bulk Cr tips for spin-polarized scanning tunneling microscopy by direct current drop-off etching, and we detail the role of etch parameters on the tip apex geometry. We present a method to evaluate the tunneling characteristics of the Cr tips using cleaved crystal planes, circumventing the need for ultra-high vacuum preparation of clean surfaces or films. We image layered antiferromagnetism on nanoscale terraces in the bilayer manganite $La_{1.4}Sr_{1.6}Mn_2O_7$ at 6.5 K. Atomic-resolution imaging is also obtained on $Bi_2Sr_2CaCu_2O_{8+\delta}$.

2.1 INTRODUCTION

Spin-polarized scanning tunneling microscopy (SP-STM) is a powerful technique for real-space imaging of atomic-scale spin features [7, 8]. Its implementation, starting from a conventional scanning tunneling microscope (STM) setup, requires careful preparation of (1) a tip with a well-defined magnetic termination and (2) a test sample with nanoscale magnetic structure.

Tips for SP-STM have been fabricated using bulk ferromagnetic (FM) [9, 10] or antiferromagnetic (AF) [11, 12] materials, or by evaporating a thin magnetic film on a nonmagnetic tip [13, 14]. While FM tips afford larger spin contrast, AF tips produce negligible stray fields and are better suited for nondestructive imaging. AF tips etched from bulk Cr are one emerging candidate for SP-STM, ideal for their monatomic composition and high Néel temperature of 311 K. They typically exhibit a canted tip magnetization which is rotatable in a 2 T field [15], sensitive to all 3D spatial components [16], and capable of atomic-resolution imaging [12]. However, the extent to which the electrochemical preparation influences these characteristics is poorly understood. Systematic studies have been mostly limited to nonmagnetic W tips [17, 18].

A major practical advantage of bulk Cr tips is that they circumvent the need for complex ultra-high vacuum (UHV) cleaning and evaporation procedures, as well as *in-situ* tip exchange [16]. However, the test magnetic systems commonly used (e.g. Cr(001) [12], Fe/W(110) [16], Co/Cu(111) [15]) still involve extensive surface preparation in a UHV environment. It is natural to ask whether an analogous simplification can be achieved by selecting a cleavable material with an appropriate magnetic landscape for spin-polarized imaging.

Here, we report a study of the SP-STM technique in two directions. First, we examine how *ex-situ* fabrication parameters affect Cr tip apex geometry, which in turn influences both atomic- and spin-resolution imaging. We etch over 70 Cr rods under various voltage sequences, and image the tips formed on both ends of the break junction. Second, we evaluate the tunneling characteristics of our tips using cleaved crystal planes as opposed to thin films. We demonstrate spin-polarized tunneling over antiferromagnetic terraces of the bilayer manganite $La_{1.4}Sr_{1.6}Mn_2O_7$, and also resolve single atoms in the cuprate $Bi_2Sr_2CaCu_2O_{8+\delta}$. These results provide a feasible approach for STM setups with *in-situ* cleavers to perform spin-polarized tunneling measurements.

2.2 Cr Tip Etching

We etch tips from square 0.5 mm × 0.5 mm polycrystalline Cr rods (99.99% purity)[*] using the standard direct current (DC) drop-off method [19]. Figure 2.1(a) gives a photograph of our setup.[†] One end of the rod is covered with a 7 mm polytetrafluoroethylene (PTFE) tubing [20] and immersed in a 5 M NaOH solution, such that the rod area in contact with the solution is minimized. Next, we apply a DC voltage to drive the anodic dissolution of Cr, eventually into CrO_4^-. The exposed portion of the rod is thinned until the weight below exceeds the tensile force and breaks off, leaving behind a work-hardened tip on both ends of the break. The voltage is immediately shut off and both the remnant tip above the break (called top) and below the break (called bottom) are rinsed in deionized water and retained for subsequent examination. We use a fresh solution (poured from the same stock) for each etch in order to standardize our tip preparation.

We evaluate the tips using a Zeiss Ultra Plus scanning electron microscope (SEM). Figures 2.1(b-e) present sample micrographs of two tips derived from the bottom and top rod ends of a single etch, at two different magnifications. We utilize two metrics to assess the tip apex geometry: (1) Aspect ratio (AR), defined as length over width measured 50 μm from the tip end [perpendicular lines in Fig. 2.1(b)], and (2) radius of curvature (RC), computed from a polynomial fit to the tip apex contour [circle in Fig. 2.1(d)]. Our results are robust across different definitions of AR with varying lengths from the tip end.

Fig. 2.2(a) displays the average tip apex AR for etch voltages of 7 V, 11 V and 15 V,

---

[*] The square 0.5 mm × 0.5 mm rods were cut from polycrystalline Cr foil purchased from Brooks Precision.

[†] See Section 2.4 for further details of the etching setup and procedure.

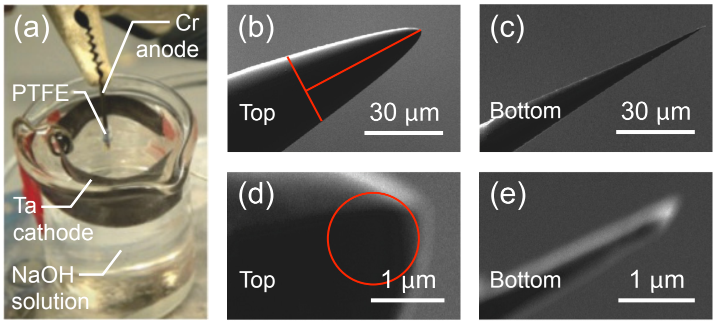

Figure 2.1: (a) Photograph of etching setup. (b-e) Scanning electron micrographs of two Cr tips derived from the (b) top and (c) bottom rod ends of a single etch. Higher magnification images of the same tips are shown in (d, e). The perpendicular lines in (b) illustrate the procedure used in computing the aspect ratio (AR), and the circle in (d) illustrates the radius of curvature (RC).

binned by top and bottom tips. The bottom Cr tips are statistically sharper than their top counterparts, because they are instantaneously disconnected at the break and do not sustain residual etching in the few seconds before the voltage is manually shut off. [21, 20, 10] Furthermore, the average ARs are largely uncorrelated with the etch voltage or sequence. No improvements are detected with a two-step process, whereby the voltage is reduced from 9 V to 3 V after a fixed time period [right end of axis break in Fig. 2.2(a)]. [12] In fact, the two-step process, with its longer etch time typically exceeding 30 minutes, is likely more susceptible to external perturbations (e.g. vibrations or solution evaporation), resulting in larger AR variability and unclear distinction between top and bottom tips. In the one-step processes, we also find the average RC of the bottom tips to be smaller than that of the top tips, but the trend is smaller and lacks the statistical significance of that of the AR.

We also consider the effect of the rod weight below the break junction on the tip apex geometry [17]. Figure 2.2(b) presents a comparison between a set of seven Cr rods covered with 7 mm long PTFE tubing and another set of seven covered with 10 mm long tubing, representing a 43% increase in combined weight (rod and tubing). The increased weight yields greater variability in the bottom tip AR despite an average 23% faster etch time, possibly because the larger weight induces an earlier and more uncontrolled break.

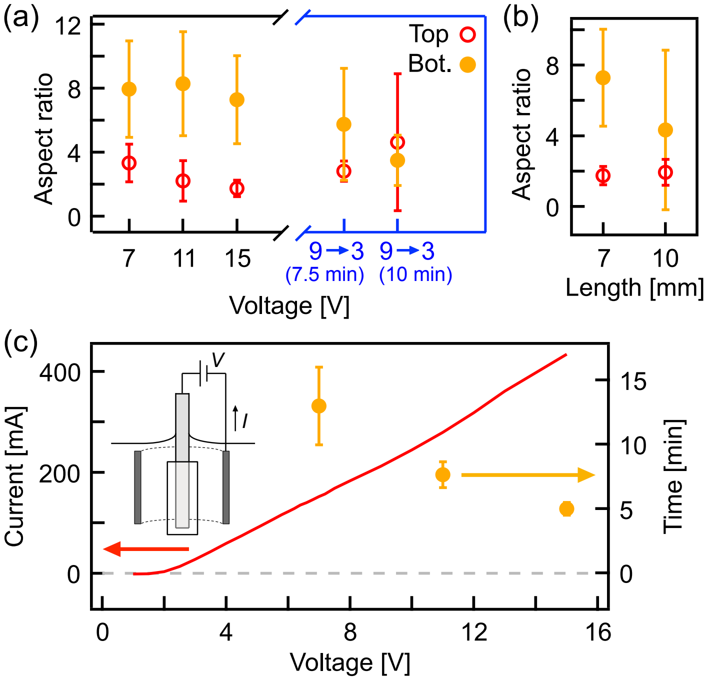

Figure 2.2: (a) Plot of aspect ratio (AR) for several etch voltages, binned by top and bottom tips. Each point represents the average of 6 tips. The right side of the axis break presents ARs associated with two-step etches – first at 9 V for the indicated time duration (7.5 min or 10 min), then at 3 V until the drop-off. (b) Plot of average AR for two different lengths of PTFE tubing, corresponding to a 43% difference in the combined weight of the Cr rod and tubing. Each point represents the average of 7 tips, etched at 15 V. (c) Potentiostatic polarization (I–V) curve (solid line) for our given etching setup (inset schematic). The onset of current near 2 V corresponds to the negative cell potential, which is dependent on the setup geometry. The circles denote corresponding average etch times.

To further understand the role of the etch voltage, we obtain a potentiostatic polarization (I–V) curve for our given setup, shown in Fig. 2.2(c) (solid line). A minimum of ∼2 V corresponding to the negative cell potential is required to drive a measurable reaction current. Above this threshold, the current rises approximately linearly with voltage, up to 15 V. Unlike previous reports on W tips [17, 22], we do not observe any saturation or upturn in the current that may be indicative of competing or secondary reactions. Figure 2.2(c) also depicts average etch times (circles) for the voltage settings used in Fig. 2.2(a), which are faster with increasing current. Taken together, Fig. 2.2 suggests the utility of larger voltages to decrease etch times without affecting tip sharpness or inducing additional reactions.

Prior to use for STM imaging, the Cr tips are cleaned by field emission onto a Cr or Au foil within the STM. Typically, we bring the tip into constant-current feedback with a set-point of 50-100 V and 0.5-3 μA for several minutes. This removes any oxides and restructures the terminal atoms on the tip apex, which allows atomic-resolution tunneling largely indepedent of the post-etch RC. A high post-etch AR, however, is still necessary to ensure a small RC after repeated field emission attempts, and probe surfaces with large corrugations and step edges. Following field emission, our resultant tips exhibit flat tunneling conductance spectra on the Cr or Au foils. This suggests a featureless tip density of states, consistent with previous experiments [16, 15] and simulations [23].

2.3 STM IMAGING

We evaluate the spin sensitivity of our Cr tips using the bilayer manganite $La_{2-2x}Sr_{1+2x}Mn_2O_7$. In this material, strong coupling of spin, orbital and lattice degrees of freedom underlies a colossal magnetoresistance effect [24], as well as a diverse display of magnetic orders [25, 26, 27]. Figure 2.3(a) shows a schematic structure of $La_{2-2x}Sr_{1+2x}Mn_2O_7$ in the Ruddlesden-Popper phase. Sr substitution alters the Mn^{3+}/Mn^{4+} valency and rapidly changes the magnetic ground state by a delicate tuning of double exchange and crystal field effects [28]. At $x = 0.30$ (and below 90 K), spins within a given bilayer are aligned parallel to the *c*-axis, but antiparallel to spins in the adjacent bilayers [Fig. 2.3(a)] [25, 26, 28, 27]. If cleavage in the *a*-*b* plane generates step edges spanning adjacent bilayers, then the AF coupling between terraces can be observed using a local probe [29]. Futhermore, we expect the spin contrast signal to be large due to the approximate half-metallic ferromagnetism within each bilayer. Figure 2.3(b) shows a schematic diagram of the projected Mn 3*d* density of states (DOS) that dominate the $La_{2-2x}Sr_{1+2x}Mn_2O_7$ electronic structure near the Fermi energy. [‡] For $0.30 \lesssim x \lesssim 0.40$, the occupied bands within $\sim$ 2 eV of the Fermi energy carry

---

[‡] See Section 2.5 for further details of the $La_{2-2x}Sr_{1+2x}Mn_2O_7$ electronic band structure.

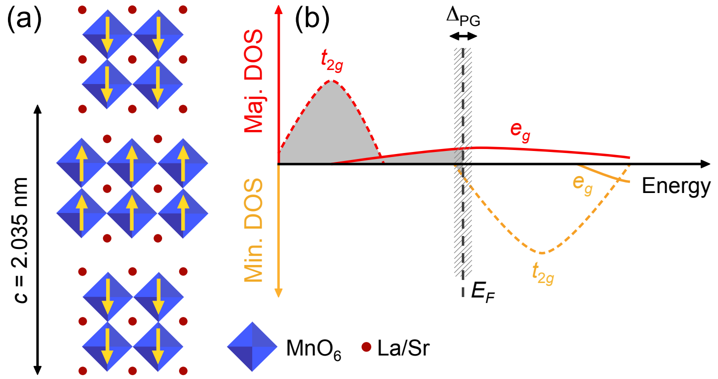

Figure 2.3: (a) Crystal structure of $La_{2-2x}Sr_{1+2x}Mn_2O_7$, depicting the interbilayer antiferromagnetic (AF) order at $x = 0.30$. (b) Schematic diagram of the projected Mn $3d$ density of states (DOS). The shading indicates the populated states below the Fermi energy. For $0.30 \lesssim x \lesssim 0.40$, the system is close to a half-metallic ferromagnet (intrabilayer), with possibly an electron pocket of minority spin t_{2g} character. The hatching represents a "pseudogap" detected by angle-resolved photoemission spectroscopy (ARPES) and scanning tunneling microscopy (STM).

majority spin [30], except for a small electron pocket of minority spin t_{2g} character that may be present at the Brillouin zone center [31, 32].

In Fig. 2.4(a), we present a constant-current image of cold-cleaved $La_{1.4}Sr_{1.6}Mn_2O_7$, obtained with a Cr tip at 6.5 K. [§] The cleavage occurs primarily between La/SrO buffer planes, as deduced from X-ray photoelectron spectroscopy (XPS) [33], and complemented by other STM studies that consistently found step edge heights to be integer multiples of the half-unit cell ($c/2$) [34, 33, 35]. Here, several terraces are evident over a 30 nm × 30 nm area, and we instead observe their heights to alternate ~14% above and below the mean value $c/2 \sim 1.05$ nm [line cut in Fig. 2.4(b)]. These apparent height differences come from a spin-valve contribution to the tunneling current that depends on the cosine of the angle subtended by the tip and sample magnetizations. Given that the tip magnetization is fixed across the scan, the apparent height modulations reflect the layered AF texture of $La_{1.4}Sr_{1.6}Mn_2O_7$.

Due to inferred in-plane screening, STM does not resolve atomic-scale features on the surface of $La_{2-2x}Sr_{1+2x}Mn_2O_7$, save for occasional nanometer-sized patches of square lattice

---

[§] The Cr tips used in Fig. 2.4 were etched at 10 V for ~7 minutes, then at 3 V until the drop-off.

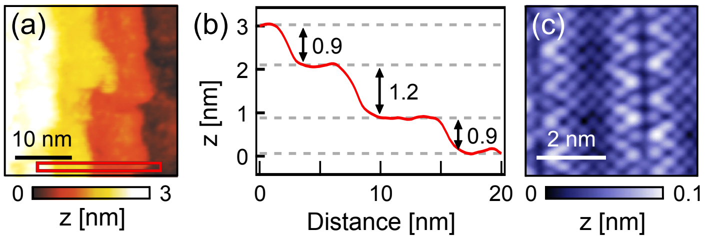

Figure 2.4: (a) Topographic image of $La_{1.4}Sr_{1.6}Mn_2O_7$, taken with a Cr tip at 6.5 K. Setpoint: -250 mV, 15 pA. (b) Averaged line profile across terraces enclosed by the rectangle in (a). The apparent ∼14% height modulations originate from the spin-polarized contribution to the tunneling current and reflect the layered AF texture. (c) Topographic image of $Bi_2Sr_2CaCu_2O_{8+\delta}$, also taken with a Cr tip at 7 K. Setpoint: 100 mV, 20 pA.

corrugations ascribed to trapped polarons [34, 36]. It has also been suggested that mobile oxygen defects obscure atomic-resolution tunneling in the layered manganites [37]. To demonstrate the spatial resolution capabilities of our Cr tips, we turn instead to the archetypical cuprate $Bi_2Sr_2CaCu_2O_{8+\delta}$, where STM on cleaved BiO planes is well established. Fig. 2.4(c) shows a 5 nm × 5 nm topographic image of $Bi_2Sr_2CaCu_2O_{8+\delta}$ taken with a Cr tip at 7 K. Both the unit cell and the structural supermodulation can be seen.

In summary, we detailed a simple method for SP-STM which does not require UHV preparation conditions. First, we investigated the preparation of bulk Cr tips by DC drop-off etching. Our findings indicate that (1) the bottom tips are statistically sharper than their top counterparts, and (2) large voltages for faster etches do not affect tip AR or produce additional reactions. Second, we have established spin- and atomic-resolution imaging with the Cr tips, on *in-situ*-cleaved $La_{1.4}Sr_{1.6}Mn_2O_7$ and $Bi_2Sr_2CaCu_2O_{8+\delta}$. Our work paves the way for the application of SP-STM to cleaved planes of strongly correlated or topological materials that are grown as high-quality single crystals, such as cuprate and Fe-based superconductors, colossal magnetoresistance materials, and topological insulators. Local spin mapping is desperately needed to unravel the exotic electronic behavior of these materials.

2.4 [Supplemental] Etching Setup and Procedure

Figure 2.5 provides additional photographic documentation of the etching setup and procedure used in this work. In Fig. 2.5(a), we present a larger scale image of our setup. A support jack raises a 10 mL beaker with 5 M NaOH solution towards a Cr rod, fixed in place by a clamp holder attached to a support stand. We use a set square [pictured in Fig. 2.5(a)] to ensure that the Cr rod axis is orthogonal to the solution interface. We also carefully cut the polytetrafluoroethylene (PTFE) tubing with a razor blade so that its top end is flat and minimally deformed from a circular cross-section. Its bottom end is pinched to prevent it from slipping off the Cr rod. To drive the etching reaction, we use a DC-regulated power supply (Tenma 72-6628). A 91 Ω resistor placed in series with the circuit stabilizes the etch speed.

We use a two-step rod immersion procedure to minimize the macroscopic tip aspect ratio, in order to reduce vibrations when scanning. The middle and right columns of Figs. 2.5(b-g) provide multiple depictions of each step. We gradually raise the level of the solution relative to the Cr rod until the instant the meniscus surpasses the PTFE tubing and re-forms around the rod, so as to confine the etching activity to a small region above the PTFE tubing.

2.5 [Supplemental] Electronic Structure of $\mathrm{La}_{2-2x}\mathrm{Sr}_{1+2x}\mathrm{Mn}_2\mathrm{O}_7$

The schematic electronic band structure of $\mathrm{La}_{2-2x}\mathrm{Sr}_{1+2x}\mathrm{Mn}_2\mathrm{O}_7$ presented in Fig. 2.3(b) is informed by simulations and experiments in literature. Figures 2.6(a, b) display the projected Mn $3d$ density of states (DOS) for the $x = 0.50$ compound, calculated by Huang *et al.* [30]. Their results indicate that $\mathrm{LaSr}_2\mathrm{Mn}_2\mathrm{O}_7$ is a half-metallic ferromagnet with a band gap in the minority spin channel of $1.7 - 1.9$ eV. Increasing electron doping (decreasing x) is modeled in the rigid band approximation, resulting in an upward shift of the Fermi level to populate some minority spin t_{2g} states. This is confirmed by angle-resolved photoemission spectroscopy (ARPES) and *ab-initio* calculations for the $x = 0.38$ (Figs. 2.6(c, d), reproduced from Sun *et al.* [32]) and $x = 0.40$ (Figs. 2.6(e, f), reproduced from Saniz *et al.* [31]) com-

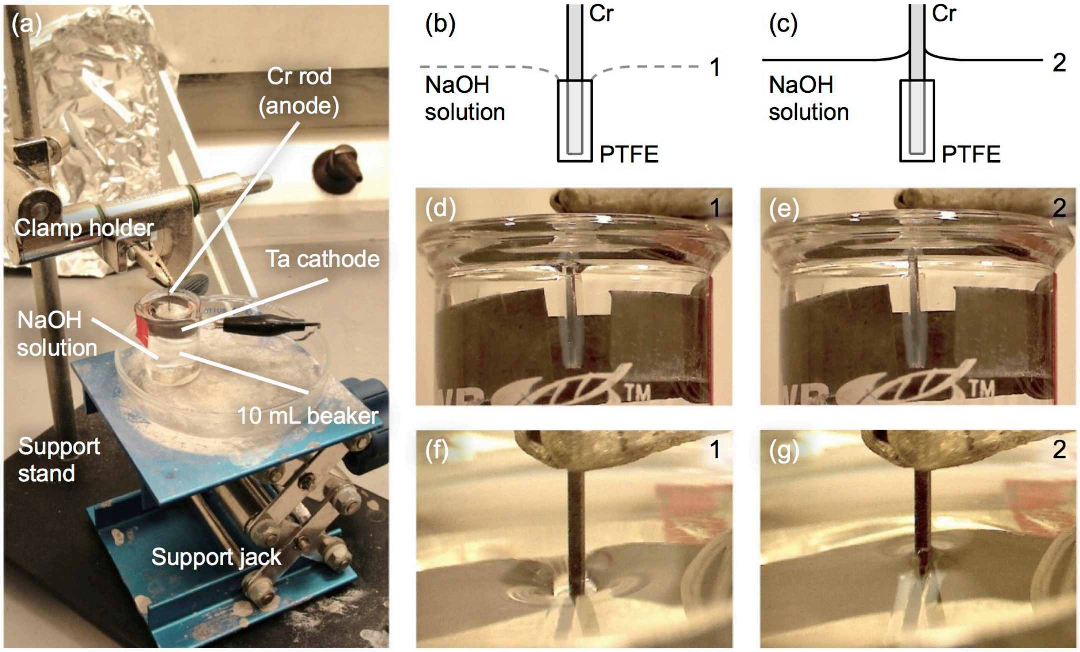

Figure 2.5: (a) Larger scale photograph of the etching setup. (b, c) Schematic and (d-g) photographic demonstration of a two-step rod immersion procedure. The figures labeled "1" (b, d, f) depict the initial entry of the bare Cr rod into the NaOH solution, during which the meniscus is bent towards the top of the polytetrafluoroethylene (PTFE) tubing. The figures labeled "2" (c, e, g) depict the second step, where the solution level is jacked up to an extent that the meniscus pops abruptly into place around the Cr rod. This sets the solution height used during the etch and minimizes the macroscopic tip aspect ratio for reduced vibrations when scanning.

pounds, which reveal an electron pocket of minority spin t_{2g} character around the Γ point.

An additional feature in the electronic structure of $\mathrm{La}_{2-2x}\mathrm{Sr}_{1+2x}\mathrm{Mn}_2\mathrm{O}_7$ is a "pseudogap" detected by ARPES [38, 39] and scanning tunneling microscopy (STM) [34, 33, 35]. For the $x = 0.30$ compound, STM extracts a gap magnitude of 196 ± 12 meV from a thermally activated transport fit [34]. Such a pseudogap is not the subject of our discussion, but we indicate its presence in Fig. 2.3(b) for completeness.

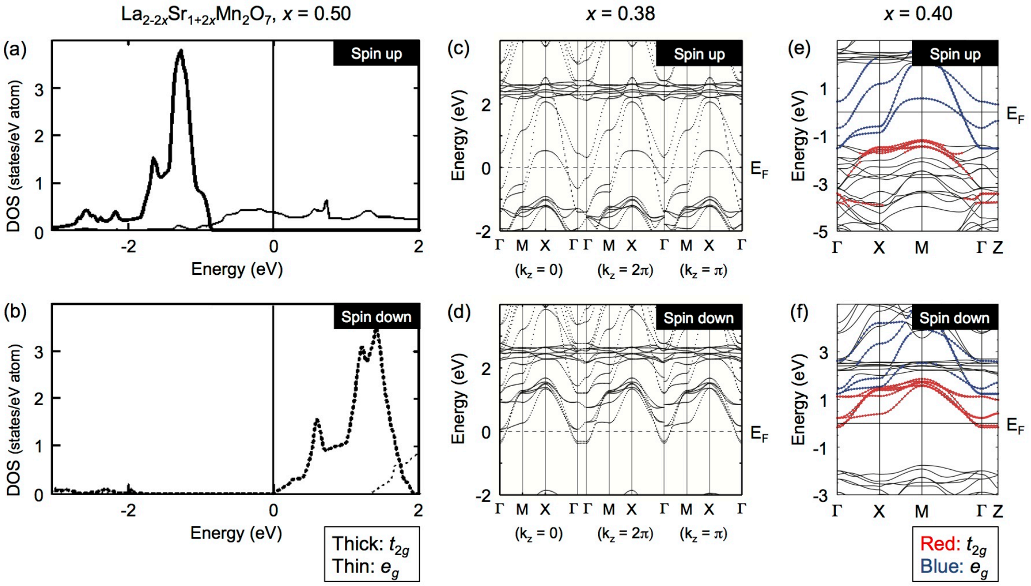

Figure 2.6: (a, b) Spin-resolved projected Mn 3*d* density of states (DOS) for $La_{2-2x}Sr_{1+2x}Mn_2O_7$, $x = 0.50$, calculated using the first-principles local density full-potential linear muffin-tin orbital (FLMTO) method. The thick (thin) lines represent the t_{2g} (e_g) states. Reprinted from Huang *et al.* [30]. (c, d) Majority and minority spin bands calculated for the $x = 0.38$ compound, using the all-electron full-potential Korringa-Kohn-Rostoker (KKR) and linearized augmented plane-wave (LAPW) methods. Reprinted from Sun *et al.* [32]. (e, f) Majority and minority spin bands calculated for the $x = 0.40$ compound, using the all-electron full-potential LAPW method with the generalized gradient approximation (GGA). The red (blue) circles represent states of dominant t_{2g} (e_g) character. Reprinted from Saniz *et al.* [31].

2.6 [Supplemental] Energy-Integrated Junction Polarization

We explain how the apparent step height modulation Δz observed in Fig. 2.4(b) can be used to extract an energy-integrated junction polarization $P_\perp$. In the Bardeen formalism [40], the spin-polarized tunneling conductance (at $T = 0$) is given by

$$\frac{dI}{dV} = 2\pi^2 G_0 |M_0|^2 (\rho_s \rho_t + m_s m_t \cos\theta), \tag{2.1}$$

where $\rho_{s,t} = \rho^{\uparrow}_{s,t} + \rho^{\downarrow}_{s,t}$ is the total density of states (DOS) of the sample/tip, $m_{s,t} = \rho^{\uparrow}_{s,t} - \rho^{\downarrow}_{s,t}$ is the spin-polarized difference, θ is the angle subtended by the sample and tip magnetizations, $G_0 = \frac{2e^2}{h}$ is the conductance quantum, and $M_0 \propto e^{-\frac{\sqrt{2m\Phi}}{\hbar}z}$ is the matrix element (Φ is the local barrier height) [19]. Assuming a sample bias of $-V$, the spin-polarized tunneling current can be written as

$$I = I_0(1 + P\cos\theta), \tag{2.2}$$

where I_0 is a non-magnetic contribution to the current and

$$P = \frac{\int_{-eV}^{0} m_s(\epsilon)m_t(\epsilon + eV)d\epsilon}{\int_{-eV}^{0} \rho_s(\epsilon)\rho_t(\epsilon + eV)d\epsilon} \tag{2.3}$$

represents a convolution of the sample and tip magnetizations. In obtaining Eq. 2.2, we have assumed that M_0 and $\cos\theta$ are independent of energy over the range considered.

The tunneling current between a Cr tip and antiferromagnetic (AF) terraces in $La_{1.4}Sr_{1.6}Mn_2O_7$ is given by $I_{\uparrow\uparrow} = I_0(1 + P\cos\theta)$ when the out-of-plane components of the sample and tip magnetizations are parallel, and $I_{\uparrow\downarrow} = I_0(1 - P\cos\theta)$ when they are antiparallel (here, θ is the tip magnetization angle relative to the surface normal). In constant-current feedback mode, this translates to a logarithmic increase $+\Delta z_1$ or decrease $-\Delta z_2$ in the tip-sample separation z, such that $I_{\uparrow\uparrow}(z + \Delta z_1) = I_{\uparrow\downarrow}(z - \Delta z_2)$. Solving for $P\cos\theta$ yields

$$P_\perp = P\cos\theta = \frac{e^{\frac{\sqrt{8m\Phi}}{\hbar}\Delta z} - 1}{e^{\frac{\sqrt{8m\Phi}}{\hbar}\Delta z} + 1}, \tag{2.4}$$

where $\Delta z = \Delta z_1 + \Delta z_2$ and Φ is approximated by the average of the tip and sample work functions [41].

Part II

Monolayer FeSe/$SrTiO_3$

This part of the thesis is organized as follows: Chapter 3 serves as an introduction, presenting a critical overview of key experimental and theroetical developments related to monolayer FeSe/SrTiO_3 since its discovery in 2012. The remaining chapters focus on the use of as-grown atomic defects in monolayer FeSe/SrTiO_3 to derive microscopic insights into its electronic and atomic structure. In Chapters 4 and 5, we report the use of STM quasiparticle interference imaging around defects to map the filled- and empty-state band structure of monolayer FeSe/SrTiO_3, as well as its low-energy orbital texture. In Chapter 6, we turn our attention to the defects themselves, using density functional theory (DFT) to identify the atomic structure of prevalent "dumbell" defects. The results shed light on the film growth process and lay the foundation towards possible nanostructuring applications with defects.

3

Monolayer FeSe/$SrTiO_3$: Overview

3.1 Introduction

3.1.1 Approaching the 2D limit with FeSe

FeSe posesses the simplest structure among the iron-based superconductors (Fe-SCs), consisting of stacked Se-Fe-Se triple layers interacting by van der Waals forces ($P4/nmm$ space group) [3]. Figure 3.1(a) shows the structure of one triple layer, which includes Fe atoms arranged in a square lattice and Se atoms staggered above and below the Fe-plane. Due to the staggering, the primitive unit cell (UC) contains two Fe atoms (and two Se atoms). However, since the low-energy bands of FeSe are dominated by Fe $3d$ orbitals, many theories or spectroscopies employ a 1-Fe UC convention.

FeSe should be the prototypical Fe-SC to investigate, except it proved difficult to synthesize in high quality at first. Its superconducting polymorph occupies a narrow region in the

Fe-Se alloy phase diagram [42], complicating common melt and self-flux growths. In 2011, Song *et al.* used molecular beam epitaxy (MBE) to grow pristine FeSe films on graphitized SiC [43, 44]. From scanning tunneling microscopy (STM) imaging, they resolved surface purity up to one atomic defect per 70000 Se sites and a V-shaped, superconducting gap of $\Delta =$ 2.2 meV [Fig. 3.1(b)]. Although MBE-grown films are not amenable to many bulk and thermodynamic probes, they have other advantages. Both the monolayer limit and interface interactions with different substrates can be readily examined.

Song *et al.* found that the FeSe films interacted weakly with the graphitized SiC substrate (islands could be displaced by an STM tip), and were thereby close to the free-standing limit [44]. Upon decreasing film thickness, T_c dropped from 7.8 K (8UC FeSe) to below 2.2 K (1UC FeSe), the base temperature of their experiment [Fig. 3.1(c)]. The drop exhibited a $1 - d_c/d$ dependence, where d is the film thickness and d_c is a critical value. This thin-film behavior was explained long ago as resulting from a general, surface boundary condition with the Ginzburg-Landau equation [45]. Thus in 2011, it did not appear that the 2D limit of FeSe would be a promising regime to explore, unless new microscopic effects could be introduced.

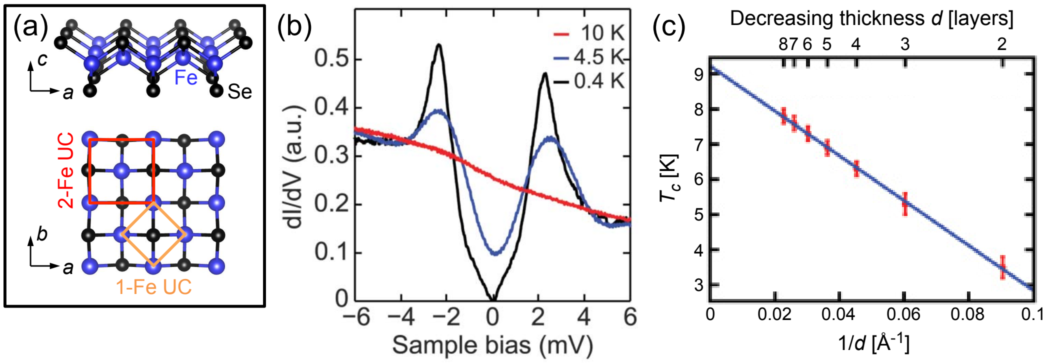

Figure 3.1: (a) Crystal structure of an FeSe monolayer; side and top views. The orange and red boxes delineate the 1-Fe UC and 2-Fe UC, respectively. (b) STM dI/dV spectra of multilayer FeSe/SiC, exhibiting a V-shaped gap of $\Delta = 2.2$ meV at $T = 0.4$ K. Adapted from Ref. [43]. (c) Gap-closing temperature T_c of multilayer FeSe/SiC as a function of inverse FeSe thickness, $1/d$. Adapted from Ref. [44].

3.1.2 Monolayer FeSe gets an oxide boost

It came as a great surprise an year later that monolayer FeSe could undergo an order-of-magnitude T_c enhancement when grown epitaxially on $SrTiO_3(001)$. The lattice mismatch between bulk FeSe (3.77 Å [46]) and $SrTiO_3$ (3.905 Å [47]) is roughly 3%. STM measurements by Wang *et al.* revealed a nodeless, double-gap structure (9.0 meV and 20.1 meV) in 1UC FeSe/$SrTiO_3$ [Figs. 3.2(a), (b)], with closing temperature T_c above their experimental limit of 42.9 K. Intriguingly, this superconductivity enhancement did not persist or even proximitize low-T_c superconductivity in a second UC of FeSe deposited on the heterostructure. STM dI/dV measurements, whose probing depth is likely limited to the surface FeSe layer, showed a semiconducting spectrum on the second FeSe layer [Fig. 3.2(c)]. This observation points to an underlying interface effect, one that is atomically-localized to the first UC of FeSe on $SrTiO_3$. Wang *et al.* speculated that electron-phonon coupling could be enhanced at the interface, based on their previous work with Pb/Si(111) and In/Si(111) films [48].

Due to technical challenges, Wang *et al.* could measure transport only in a Si-capped, 5UC FeSe/$SrTiO_3$ heterostructure. They measured zero resistance at some temperature lower than 30 K, and extrapolated a resistive onset temperature around 53 K. (As shown by STM spectroscopy in Figs. 3.2(b)-(c), the superconducting signal originates from the interface FeSe layer only.)

Angle-resolved photoemission spectroscopy (ARPES) measurements in the same year mapped band structure details, providing initial insights into the role of the interface. Liu *et al.* [49] found that the Fermi surface (FS) of 1UC FeSe/$SrTiO_3$ comprises nearly-circular electron pockets at the Brillouin zone (BZ) corner M [Figs. 3.2(d), (e)]. The usual hole pocket(s) at the zone center Γ, present in other Fe-SCs, is sunken 80 meV below the Fermi energy (E_F) [Fig. 3.2(f)]. Assuming doubly-degenerate electron pockets, a Luttinger count yields 0.10 electrons/Fe atom. Thus, 1UC FeSe appears to be electron-doped from the substrate. Liu *et al.* also resolved nearly-isotropic gaps on the electron pockets, of values 13±2 meV and 15±2 meV for two samples. They found the gap-closing temperature to be 55±5 K.

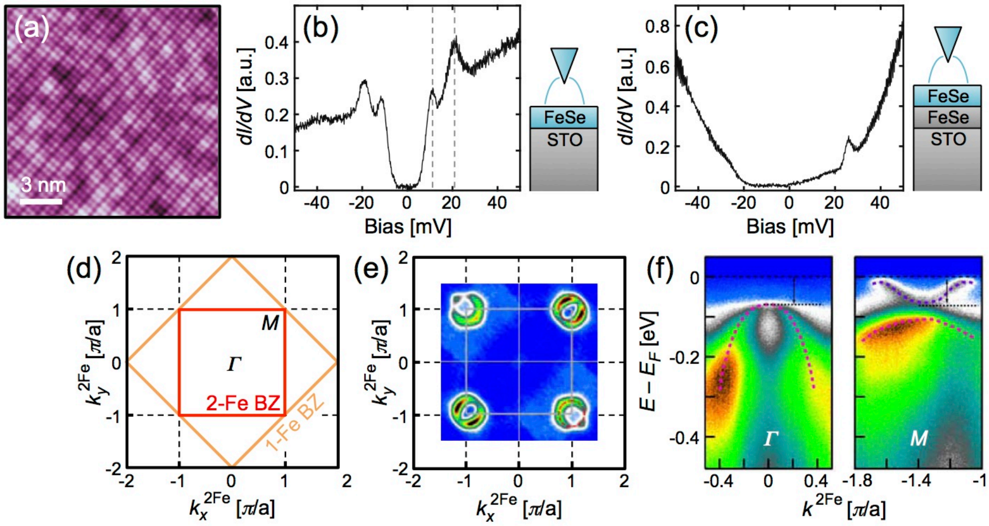

Figure 3.2: (a)-(c) Initial STM measurements of 1UC FeSe/SrTiO$_3$, adapted from Ref. [1]. (a) Atomically-resolved topography. Each bright spot represents a top-layer Se atom. (b), (c) dI/dV spectrum of 1UC and 2UC FeSe/SrTiO$_3$, respectively. The dashed vertical lines mark two gap edge peaks at 9 mV and 20.1 mV. The schematics illustrate that the tunneling depth is largely restricted to the surface FeSe layer. (d)-(f) Initial ARPES measurements of 1UC FeSe/SrTiO$_3$, adapted from Ref. [49]. (d) Brillouin zone (BZ) conventions. (e) Fermi surface map, revealing electron pockets at the BZ corner M. (f) High-symmetry cuts across the BZ center Γ and corner M, revealing sunken hole pockets.

Before proceeding, we reiterate that monolayer FeSe/SrTiO$_3$ is not monolayer FeSe. A giant T_c enhancement is present only in the former, due to some effect introduced by the SrTiO$_3$.

3.2 Experimental Challenges

A foremost and pressing challenge related to 1UC FeSe/SrTiO$_3$, even before attempting to understand the microscopic mechanism of its enhanced superconductivity, has been the characterization of its growth, atomic structure, and basic superconducting metrics. As a point of emphasis, traditional bulk tools do not work well for this system. Not only is the cross section of a single UC layer tiny, but FeSe also exhibits extreme air sensitivity, hampering *ex-situ* measurements. Thus, even the simplest question of determining T_c represents a highly nontrivial endeavor requiring customized and integrated instrumentation in ultra-high-vacuum (UHV). Example apparatuses include combined MBE-ARPES-STM systems, double chalcogen-MBE/oxide-MBE chambers, and customized *in-situ*, four-point-probe setups.

In this section, we review various experiments related to film characterization, categorized under four questions. We attempt to reflect the sentiments of the scientific community by conveying both the excitement related to the spectacular findings of *tour-de-force* experiments, and scrutiny related to the challenging nature of these feats and of film quality/homogeneity.

3.2.1 WHAT IS T_c?

Table 3.1 presents a comparison of T_c measurements across different probes, heterostructures, and laboratories. Among various *in-situ* ARPES measurements [50, 51, 52], there is consensus in a gap-closing temperature $T_c \sim 65$ K. Some variation exists with the degree of post-growth annealing [50] (see subsection 3.2.2 for details). Enhancement of T_c up to 75 K is possible if extra tensile strain is introduced through an additional $KTaO_3$ substrate [53].

More general and traditional observations of superconductivity include (1) a zero-resistance state and (2) the Meissner effect (perfect diamagnetism). Due to air sensitivity, *ex-situ* transport and thermodynamic measurements require film capping: amorphous Se [60], amorphous Si [1], or epitaxial FeTe [56]. In all cases, film characteristics were degraded. Transport measurements of capped heterostructures have found a zero-resistance state below $\sim$20 K, and a rough onset temperature possibly up to $\sim$50 K. Similarly, magnetization measurements of capped samples have suffered from weak signals, broadened onset temperatures, or low superconducting volume fractions.

Given that many potential applications require some degree of atmosphere exposure, it remains crucial to investigate why capping, particularly epitaxial FeTe, has not worked well. FeTe possesses the same crystal structure as FeSe and its layers interact via van der Waals forces, so naively it should not create a severe disturbance of the FeSe layer below. Several

Table 3.1: Comparison of T_c measurements across different probes, heterostructures, and laboratories. We distinguish measurements without (*in situ*) and with (*ex situ*) a capping layer.

Corresponding authors	Technique	Definition	Heterostructure	Value [K]	Ref.
	in-situ				
X.-C. Ma, Q.-K. Xue	STM	Gap-closing temp.	1UC FeSe/Nb:$SrTiO_3$	>42.9	[1]
L. Wang, X.-C. Ma	STM	Gap-closing temp.	1UC FeSe/$SrTiO_3$	>50.1	[54]
X.J. Zhou, Q.-K. Xue	ARPES	Gap-closing temp.	1UC FeSe/Nb:$SrTiO_3$	65±5	[50]
D.L. Feng	ARPES	Gap-closing temp.	1UC FeSe/Nb:$SrTiO_3$	60±5	[51]
B.P. Xie, D.L. Feng	ARPES	Gap-closing temp.	1UC FeSe/Nb:$SrTiO_3$/$KTaO_3$	70	[55]
B.P. Xie, D.L. Feng	ARPES	Gap-closing temp.	1UC FeSe/Nb:$BaTiO_3$/$KTaO_3$	75±2	[53]
Z.-X. Shen	ARPES	Gap-closing temp.	1UC FeSe/Nb:$SrTiO_3$	58±7	[52]
J.-F. Jia *et al.*	4-probe	Zero resistance	1UC FeSe/Nb:$SrTiO_3$	109	[2]
	ex-situ				
X.-C. Ma, Q.-K. Xue	Transport	Zero resistance	Si/5UC FeSe/$SrTiO_3$	<30	[1]
		Onset temp.		53	
Q.-K. Xue *et al.*	Transport	Zero resistance	Si/10UC FeTe/1UC FeSe/$SrTiO_3$	23.5	[56]
		Onset temp.		40.2	
Q.-K. Xue *et al.*	Magnetization	Onset temp.	Si/10UC FeTe/1UC FeSe/$SrTiO_3$	21	[56]
C.W. Chu	Magnetization	Onset temp.	Si/10UC FeTe/3-4UC FeSe/$SrTiO_3$	20−45	[57]
L. Wang, J. Wang	Magnetization	Onset temp.	10UC FeTe/1UC FeSe/Nb:$SrTiO_3$	85	[58]
D.L Feng, Y. Wang	Magnetization	Onset temp.	Se/2UC FeSe/2UC $Fe_{0.96}Co_{0.04}Se$/ 1UC FeSe/Nb:$SrTiO_3$	65	[59]

hypotheses have been put forward. Ultrafast spectroscopy revealed an acoustic phonon mode in FeTe that may relax phonon-mediated pairing in FeSe [61]. Alternatively, cross-sectional TEM revealed that intermixing with the capping layer can occur, whereby Te atoms substitute Se atoms in the FeSe monolayer [62]. As a third possibility, Zhao *et al.* proposed that FeTe may hole-dope FeSe, reducing T_c [63].

In Table 3.1, we distinguish heterostructures that have conducting, Nb-doped $SrTiO_3$ from those that do not (undoped, bulk-insulating $SrTiO_3$). In general, transport measurements require an insulating $SrTiO_3$ substrate, but there are speculations that Nb-doped $SrTiO_3$ produces higher quality films. Sun *et al.* [58] hinted that "high quality FeSe films are easier to be achieved by MBE growth on conductive STO [$SrTiO_3$] substrates comparing to insulating STO substrates since the conductive STO substrate shows more flat and homogeneous surface for sample growth." In anticipation of subsection 3.2.4, we advocate that a systematic investigation of such preparation details or trade secrets may uncover hidden variables that help decrease the spread of results exemplified in Table 3.1.

In-situ, MICRO-FOUR-POINT MEASUREMENTS

In late 2014, Ge *et al.* blew the field out of the water, so to speak, with their report of T_c above 100 K in 1UC FeSe/SrTiO$_3$ [2]. Here, we review their experiment in detail. The authors converted a commercial cryogenic STM into an *in-situ*, micro-four-point probe by replacing the single STM tip with a set of four Cu/Au wires, separated by 10-100 μm [Fig. 3.3(a)]. The four probes were brought towards the sample at a 20° incline using conventional STM approach, until one probe made contact. The probes were then collectively translated into the sample, until Ohmic contact with the sample was individually established for all four probes. Figure 3.3(b) shows a set of temperature-dependent, four-point I-V curves, transitioning from a linear (normal state, Ohmic) to non-linear (superconducting, zero resistance) dependence below T_c.

Due to sample inhomogeneity or film damage from probes, linear I-V curves were sometimes observed below T_c. As a result, Ge *et al.* compiled resistance vs. temperature (R-T) plots in two manners. First, they acquired four-point I-V measurements from separate locations for each temperature [Fig. 3.3(c)]. As long as one I-V curve per temperature showed signs of zero resistance, that temperature was deemed to be below T_c. With this method, Ge *et al.* determined T_c to be 109 K. Alternatively, they were also able to construct an R-T plot from measurements over one fixed location [Fig. 3.3(d)]. With this second method, the demonstrated a similar T_c of 99 K.

We enumerate several questions that have been raised about this experiment, and the authors' responses:

1. *Question:* SrTiO$_3$ undergoes a structural transition at 105 K. Could this be responsible for the purported resistive transition at 109 K?
   Response: The authors performed a control experiment on bare, Nb-doped SrTiO$_3$, and showed that the structural transition produced a negligible signature in the R-T plot (Fig. 3(b) of Ref. [2]).

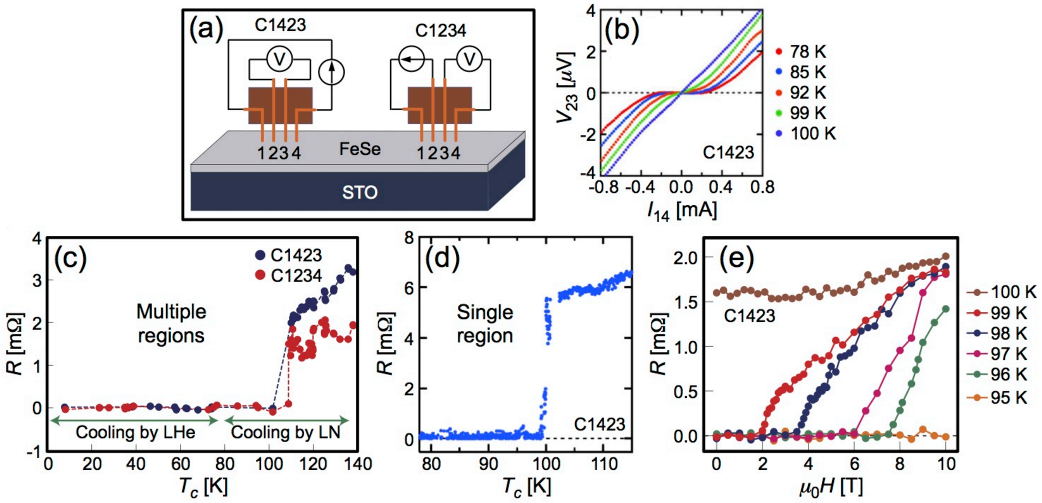

Figure 3.3: (a) Schematic of *in-situ*, micro-four-point measurements of 1UC FeSe/SrTiO$_3$. Two possible configurations are shown. (b) Four-point I-V curves, showing a metal-superconductor transition at a single location of the film. (c) Resistance vs. temperature plot, displaying a transition temperature T_c = 109 K. The data points are extracted from I-V curves acquired over different regions of the sample. (d) Resistance vs. temperature plot, with data points extracted from I-V curves acquired at a fixed point on the sample. (e) Magnetic-field dependent resistance at various temperatures. Adapted from Ref. [2].

2. *Question:* Don't the measured values of $T_c = 109$ K and $J_c = 1.3 \times 10^7$ A/cm^2 appear unexpectedly large?

   Response: The authors performed a control experiment on optimally-doped $Bi_2Sr_2CaCu_2O_{8+\delta}$, and found $T_c = 90$ K, $J_c \sim 6000$ A/cm^2, in line with expectations. Their J_c value is an order of magnitude higher than that of capped 1UC FeSe/SrTiO$_3$ films [56], but similar to that of $YBa_2Cu_3O_{7-x}$ films [64].

3. *Question:* Shouldn't there be a Berezinsky-Kosterlitz-Thouless (BKT) effect that broadens the resistive transition for a 2D superconductor? Why is the resistance drop so sharp [Fig. 3.3(c)], such that there are no data points within the transition [65]?

   Response: Below T_c, conduction is 2D and restricted the SC FeSe monolayer. Above T_c, conduction gets shorted through the Nb-doped SrTiO$_3$ substrate, which is 3D and has a much lower resistivity than normal-state FeSe. Thus, the BKT transition is masked by shorting through the metallic substrate. It is also possible that there could be a proximity effect downard into $SrTiO_3$, such that the total system is not entirely 2D. The authors were able to collect data points within this sharp transition [Fig. 3.3(d)].

4. *Question:* In light of the previous question, why not use an insulating $SrTiO_3$ substrate?
   Response: The authors cited practical challenges [2]: "Further limits exist for detecting films grown on an insulating substrate, as the feedback required to control the contact between the film and the tip is extremely difficult."

5. *Question:* Why doesn't the resistance change when the contact separation is increased tenfold [65]?
   Response: When the probe separation distances are uniform, the resistance should scale with probe separation in both an infinite 2D conductor and a half-infinite 3D conductor. However, when the probe distances are unequal, their relationship to the overall resistance is more complicated (see Supplemental Information of Ref. [2]).

6. *Question:* How could the resistive transition T_c be higher than the gap-closing temperature T_c measured *in-situ* by ARPES?
   Response: ARPES averages signal over a beam spot size, but the *in-situ* four-point probe may pick up filamentary superconductivity. Indeed, the authors found non-SC regions below T_c, but this could be attributed to both intrinsic sample inhomogeneity or film damage from probes. Alternatively, if the out-of-plane coherence length is short, superconductivity might be stronger at the bottom of the FeSe triple layer than at the top. ARPES and STM measure the top, but transport accesses the lowest-resistivity part, which may be at the buried interface.

Despite intense scrutiny, we remain unaware of fatal flaws with the experiment by Ge *et al.* To the authors' further credit, no one has offered an alternative, non-SC explanation for the magnetic-field-dependent R-T plots [Fig. 3.3(e)]. Nevertheless, there are increasing calls for duplication of this result, as well as complementary *in-situ* magnetization measurements of the Meissner effect [65, 66]. The latter will require new instrumentation, but will surely be an important piece of the puzzle.

3.2.2 What are the necessary growth conditions?

Understanding the interface atomic structure of 1UC FeSe/$SrTiO_3$ is prerequisite to any reliable modeling of electronic structure, and cannot be relegated as a secondary "materials" problem. Although $SrTiO_3$ is a workhorse substrate for MBE growth, it is notorious for its plethora of surface reconstructions that sensitively depend on preparation conditions. With the (001) surface alone, O deficiency can drive the following reconstructions: 2×1, 2×2, $c(4\times2)$, $c(4\times4)$, 4×4, $c(6\times2)$, $\sqrt{5}\times\sqrt{5}\ R26.6°$, $\sqrt{13}\times\sqrt{13}\ R33.7°$ [67]. Here, we review the daunting task of elucidating the interface structure and corresponding progress from two angles – clarifying/controlling film growth conditions (this subsection), and performing interface measurements of the final heterostructure (subsection 3.2.3).

Figure 3.4 presents a brief flowchart of typical growth procedures for 1UC FeSe/$SrTiO_3$. We focus on two of the more curious aspects of this procedure: (1) a novel 950 °C Se etch and (2) the post-growth annealing process that renders the FeSe monolayer SC.

As-bought crystals of $SrTiO_3$ have contaminated surfaces. In their original report, Wang *et al.* introduced a novel strategy to clean their Nb-doped $SrTiO_3$ substrates: they annealed the substrates in their MBE chamber at 950 °C for 30 minutes, under a Se flux. [1]. This treatment produced atomically-flat terraces amenable to STM imaging (albeit lacking atomic resolution). Subsequently, Bang *et al.* hypothesized through model density functional theory (DFT) calculations that the high-temperature Se etch could create Se substitutions of surface O atoms [68]. These Se_O substitutions could then nucleate the growth of the first FeSe monolayer, leaving behind O vacancies that stabilize binding and donate electron carriers.

Later films grown on insulating $SrTiO_3$ employed more conventional and documented preparation protocols, involving an *ex-situ* H_2O/acid etch followed by a high-temperature O_2

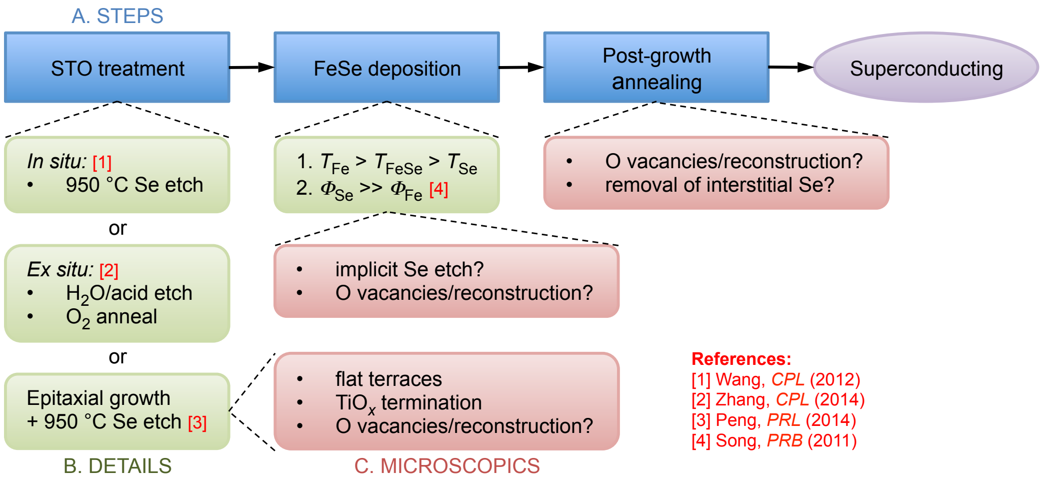

Figure 3.4: Flowchart of growth procedure. The blue boxes highlight the three primary steps that lead to SC 1UC FeSe/$SrTiO_3$. The green boxes describe the details of each step, and the red boxes describe speculations of the corresponding microscopic picture.

anneal in a tube furnace. The H_2O/acid etch is believed to preferentially remove SrO, which has ionic bonding character, and leave behind a TiO_2-terminated surface [69, 70, 71]. Despite the absence of an explicit Se etch, it is possible that Se_O substitutions are still generated during the deposition of 1UC FeSe. To grow stoichiometric FeSe, two conditions are typically employed [44]. First, since Se is significantly more volatile than Fe, one sets the substrate temperature between the source temperatures: $T_{Fe} > T_{FeSe} > T_{Se}$. At least for growth on "inert," graphitized SiC, this condition was rationalized as follows: Impinging Fe atoms with temperature $\sim T_{Fe}$ will ideally be adsorbed with sticking coefficient close to unity, while impinging Se atoms can stick only if they bind to free Fe on the substrate. Second, to compensate for high Se losses and to mitigate excess Fe clustering, typical molar flux ratios Φ_{Se}/Φ_{Fe} range from 5 to 20. With these two conditions, there may still be a sizeable Se chemical potential at the $SrTiO_3$ surface that can drive the kinds of Se reactions proposed by Bang *et al.* But this speculation remains open to experimental verification.

After deposition on $SrTiO_3$, the as-grown FeSe monolayer becomes SC only after an additional vacuum anneal, up to 550 °C for several hours. He *et al.* used ARPES measurements to show in this process, the FeSe monolayer is progressively doped with electron carriers [50]. The electron doping induces a non-rigid band transformation that eventually leaves the FS with only electron pockets and opens up a gap. The authors suggested that the electron doping could arise from O vacancies in $SrTiO_3$ created during annealing. Berlijn *et al.* investigated the possibility of Se vacancies, but their calculations revealed them to be hole dopants, not electron dopants [72]. More recently, cross-sectional TEM imaging by Li *et al.* suggested the presence of interstital Se atoms trapped at the FeSe/$SrTiO_3$ interface, which are subsequently released upon annealing. The authors proposed that the removal of these interstitial Se atoms allows O vacancies in $SrTiO_3$ to effectively donate electron carriers to the FeSe monolayer [73].

3.2.3 What is the interface structure?

Since the characterization of the interface atomic structure is presently a fast-paced, competitive endeavor, we simply present a chronological overview of various experimental developments, with the caveat that newer works may supersede older ones. Before reviewing specific measurements, we compare and contrast three tools that have been used to probe the interface.

1. Scanning tunneling microscopy (STM).
   Pro: An *in-situ* technique commonly integrated with a MBE chamber.
   Con: An indirect technique that requires additional modeling to make inferences about the buried interface.

2. Electron diffraction: reflection high-energy (RHEED) or low-energy (LEED).
   Pro: An *in-situ* technique that can also monitor real-time growth (RHEED).
   Con: Phase information is unavailable. Also, the interface signal is buried after FeSe deposition [52]. Structural changes to the interface that may occur during post-growth anneal are invisible to these techniques.

3. Transmission electron microscopy (TEM).
   Pro: Direct atomic-resolution imaging of the interface cross-section.
   Con: An *ex-situ* technique that requires capping (commonly FeTe). As evinced by Ref. [62], the capping may unintentionally produce intermixing, whereby the top-layer Se atoms of 1UC FeSe are substituted with Te atoms. The size mismatch between Se and Te can strain the monolayer film, possibly altering its original binding structure to $SrTiO_3$.

STM

The first hint of any interface structure was the appearance of dark stripes with 2×1 periodicity in STM topographic images [Fig. 3.5(a)] [1, 68]. To explain this structure, Bang *et al.* proposed an atomic model where half the O atoms on the surface TiO_2 layer are stripped off, and the bottom-layer Se atoms of the FeSe monolayer are laterally registered with the O vacancy sites [68]. The authors argued that such arrangement could increase the binding energy, electron-dope the FeSe monolayer, and cause the FeSe monolayer to relax with a 2×1 superstructure. As a caveat, the 2×1 stripes have not been universally observed. They are absent in AFM topographies [74], which might point to an electronic origin of the stripes, and are also absent in STM topographies of 1UC FeSe deposited on insulating $SrTiO_3$ [54].

Another STM observation related to the interface structure are half-UC phase shifts that occur either discontinuously at a trench [75], or continuously within a few nanometers of a domain boundary [76]. Since the domains that are shifted by half-UCs appear to be electronically equivalent, one could claim additional support that the bottom-layer Se atoms are laterally registered with O atoms, not Ti atoms, as there are two equivalent O sites within a TiO_2 UC.

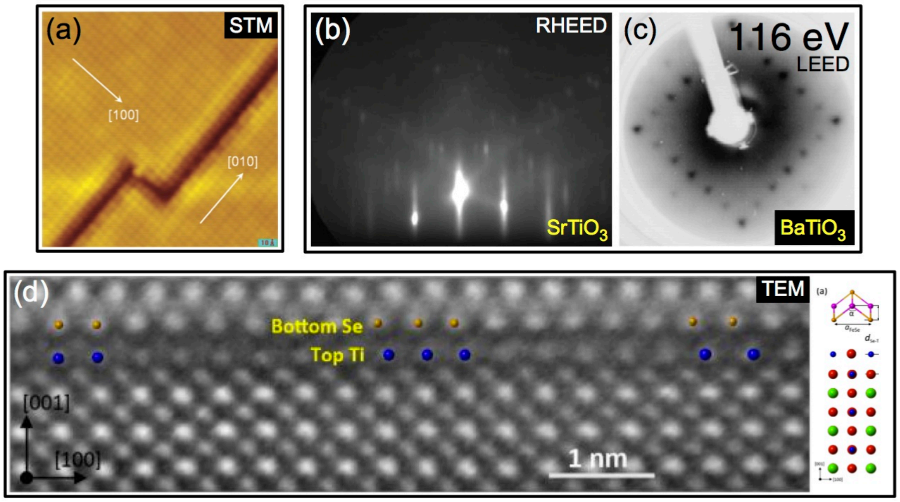

Figure 3.5: Measurements of interface structure. (a) STM topographic image showing orthogonal domains with dark stripes of 2×1 periodicity. Across the trench, there is a half-UC phase shift. Adapted from Ref. [68]. (b) RHEED diffraction patterns of treated $SrTiO_3$ prior to FeSe deposition, exhibiting reconstruction spots. Adapted from Ref. [52]. (c) LEED diffraction patterns of treated $BaTiO_3$ prior to FeSe deposition, exhibiting 3×3 spots. Adapted from Ref. [53]. (d) Cross-sectional TEM image of FeTe/1UC FeSe/$SrTiO_3$, revealing that the $SrTiO_3$ is terminated with a double TiO_x layer (inset depicts atomic model). In addition, due to lattice mismatch, the bottom-layer Se atoms and top-layer Ti atoms are incommensurate. Adapted from Ref. [73]

RHEED/LEED

Lee *et al.* grew 1UC FeSe on $SrTiO_3$ with neither *in-situ* Se etching nor *ex-situ* treatment [52]. They simply annealed as-bought substrates up to 830 °C in their MBE chamber, until RHEED measurements detected superstructure spots [Fig. 3.5(b)]. Subsequent deposition of FeSe and post-growth anneal resulted in SC samples with 1×1 diffraction spots. While the authors have yet to identify their specific $SrTiO_3$ reconstruction, they demonstrated at the least that their starting substrate was O deficient.

Peng *et al.* found a qualitatively different behavior in 1UC FeSe/$BaTiO_3$ [53]. After annealing $BaTiO_3$ at 950 °C under Se flux, their LEED images exhibited 3×3 spots. Curiously, growth of 1UC FeSe produced three distinct domains: one domain commensurate with the $BaTiO_3$ 1×1 UC, with expanded lattice constant 3.99 Å; two domains rotated by ±18.5°, commensurate with a $BaTiO_3$ 3×3 supercell, with smaller lattice constant 3.78 Å. Furthermore, ARPES detected SC gaps in all three regions, with closing temperature T_c ranging from 70–75 K. These observations may imply that neither lattice constant nor the lateral atomic registry between 1UC FeSe and its underlying substrate are critical factors behind the enhanced superconductivity of this heterostructure.

TEM

Using cross-sectional TEM, Li *et al.* [73] imaged a double-TiO_x termination at the interface of FeTe/1UC FeSe/$SrTiO_3$ [Fig. 3.5(d)]. Although such termination had long been proposed as a candidate model for the 2×1 surface reconstruction [77], it had largely been neglected in atomic models of 1UC FeSe/$SrTiO_3$ until this point. Roughly speaking, the extra TiO_x termination is half as polar as a bulk TiO_2 layer, and helps $SrTiO_3$ mitigate a divergence of the electrostatic potential towards its bulk [78]. Structural and ferroelectric properties are likely modified near this double-TiO_x termination, and more modeling is necessary to understand their implications.

In addition, Li *et al.* extracted structural parameters and found the 1UC FeSe to have a 9.5% reduced chalcogen height with 2.5% in-plane lattice strain (compared to bulk values). Furthermore, within a ∼10 nm cross section, the authors imaged a lateral half-UC shift between the bottom Se atoms and topmost Ti atoms. If this feature is characteristic of uncapped 1UC FeSe/$SrTiO_3$, then it suggests that the heterostructure has local bond disorder due to lattice incommensuration. Perhaps the vertical structure of the interface is more vital than its lateral structure.

3.2.4 What is the characteristic STM dI/dV line shape?

At the crux: inhomogeneity

In the closing subsection of this part of the chapter, which describes experimental challenges in characterizing film quality and superconducting parameters, we discuss a subtle issue of inhomogeneity in the STM dI/dV line shape. We draw attention to some more ambiguous observations that could become more meaningful if subject to further systematic investigation.

From the preceding subsections, we can conclude that 1UC FeSe/SrTiO$_3$ is fundamentally inhomogeneous on different levels. For example, a continuous range of SC gap sizes can be achieved by the extent of post-growth annealing [50], yet the corresponding stoichiometry (presumably 1UC FeSe/(Sr$_{1-x}$Nb$_x$)TiO$_{3-y}$) remains unknown. This hidden parameter adds some amount of variance across different film samples. As a second example, *ex-situ* TEM experiments suggest that the FeSe monolayer and SrTiO$_3$ substrate are laterally incommensurate, which introduces additional disorder. As a third example, and perhaps the most important, *in-situ* ARPES measurements resolve a gap closing temperature ∼65 K, whereas *in-situ* transport measurements observe a resistive transition up to 109 K. If there are no systematic errors with both experiments, then inhomogeneity is needed to reconcile this discrepancy. ARPES averages signal over the beam spot size, whereas micro-four-point measurements can pick up a filamentary SC path traversing the probes. In this light, uncovering and mitigating the sources of inhomogeneity are crucial.

STM dI/dV point spectroscopy probes atomic-scale inhomogeneity with extreme sensitivity. Given the aforementioned inhomogeneity in 1UC FeSe/SrTiO$_3$, it is unsurprising that there exists large variations in the dI/dV line shape within the same sample, or across different samples and different groups [Fig. 3.6]. But the peaks, dips, and kinks in the dI/dV line shape can also be challenging to interpret. This has generated some confusion as to whether 1UC FeSe/SrTiO$_3$ exhibits one gap, two gaps, or two bosons. In general, inhomogeneity is often relegated as an undesirable quality, or conveniently cited as a justification for discrepant results. Here, we propose that a principled investigation of dI/dV variations may prove to be a powerful probe of inhomogeneity, and uncover hidden insights. There are already indications of curious features, but more sampling and statistics would be useful.

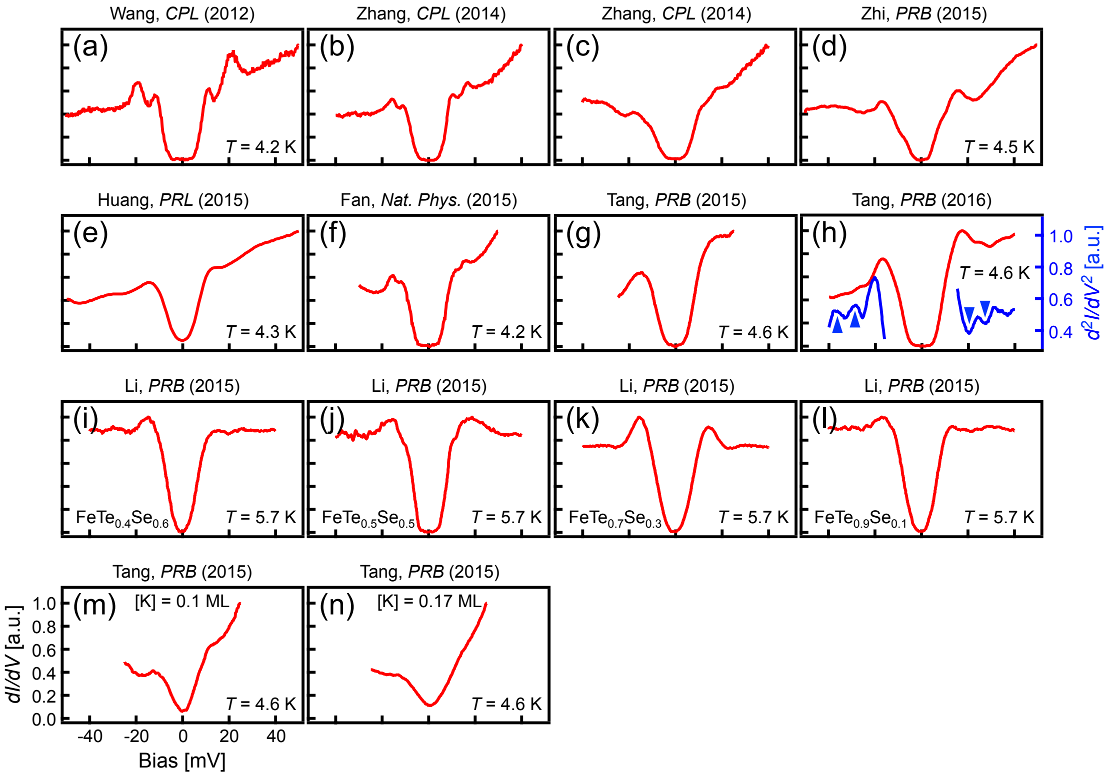

Figure 3.6: Compilation of dI/dV point spectra of 1UC FeSe/SrTiO$_3$ and related materials, across different films and laboratories. (h) Additional d^2I/dV^2 point spectrum, revealing two sets of peaks/dips corresponding to boson modes. While gap values close to 15 meV are roughly universal, double-gap or double-boson features are possibly more sensitive to inhomogeneity.

One gap, two gaps, or two bosons?

In their initial STM measurements of 1UC FeSe/SrTiO$_3$, Wang *et al.* reported two gaps in the dI/dV point spectrum, at 9 meV and 20.1 meV respectively [1]. This finding appeared to contradict early ARPES measurements of a single isotropic gap on the zoner corner electron pockets, of values $\Delta = 13\pm2$ meV in one film and 15 ± 2 meV in another film [49]. On the STM front, subsequent dI/dV measurements exhibited some degree of variation, with the double-gap structure not being universally visible (for example, Ref. [54]). On the ARPES front, higher-resolution measurements resolved some degree of gap anisotropy [55, 79], but never found more than a single gap. Thus, the second gap has proven elusive in detection and mysterious in identity.

Coh *et al.* offered an alternative explanation for the double-gap signature [80]. The authors calculated the DFT phonon spectrum of 1UC FeSe, using a modified exchange-correlation functional GGA+A. They found one phonon mode at 10 meV, corresponding to transverse, in-plane displacements, and another at 20 meV, corresponding to transverse, out-of-plane displacement of Fe atoms. They suggested that the double-peak structure could actually be fingerprints of these two phonon modes. Following this report, Tang *et al* examined d^2I/dV^2 point spectra of 1UC FeSe/SrTiO$_3$ and K-coated 2-4 UC FeSe/SrTiO$_3$ [81]. They identified positive-energy dips and negative-energy peaks as bosonic modes, and found that the features clustered at two characteristic energies: 11 meV and 21 meV. Comparing to the bulk FeSe phonon spectrum, they argued that these modes could be the E$_g$(Se) phonons at 12-13.1 meV, the A$_{1g}$(Se) phonons at 19.8 meV, or the SrTiO$_3$-TO2 phonon at 21.7 meV. Thus far, ARPES has not corroborated these results with corresponding kinks in the electron pocket dispersion.

Another inhomogeneous feature of the dI/dV line shape is the "flatness" of the gapped portion of the spectrum. In some cases dI/dV is flatly zero within the gap; in other cases, the gap is "filled in" to become more V-shaped. The V-shaped spectra may be correlated with disorder, as they appear more prominently in 1UC FeTe$_{1-x}$Se$_x$/SrTiO$_3$ films [62], K-coated 1UC FeSe/SrTiO$_3$ films [82], or 1UC FeSe "nanoflakes" on SrTiO$_3$ [62]. More recently, Song *et al.* demonstrated how the dI/dV line shape could evolve from having a V-shaped gap to a flat-bottomed gap by progressively depositing K atoms on multilayer FeSe/SiC [83]. A similar transformation was found in 1UC FeSe/SrTiO$_3$ upon post-growth annealing [84]. Such sensitivity to disorder may reveal hints of the gap symmetry, but more systematic investigation is required.

3.3 Electronic Structure and Pairing

Having reviewed the basic properties of 1UC FeSe/SrTiO$_3$ and challenges in their measurement, we turn to the subject of electronic structure and pairing. With the early discovered Fe-SCs, two observations inspired proposals of s_{+-} superconductivity. First, the SC phase emerged upon doping a parent antiferromagnetic (AFM) metal. Second, the generic FS of these systems comprised disparate electron pockets at the zone corner M and hole pockets at the zone center Γ. Mazin *et al.* [85] and Kuroki *et al.* [86] argued that repulsive AFM fluctuations, connecting electron and hole pocket states, could pair electrons if the order parameter reversed sign.

Though not without contenders [87], the aforementioned picture of s_{+-} superconductivity proved prevailing in the early years of Fe-SCs. This dominance met an abrupt end with the discoveries of alkali-doped FeSe (2011) and 1UC FeSe/SrTiO$_3$ (2012). In the "best" case, pairing theories involving spin fluctuations could be modified to stabilize d-wave gap symmetry in these compounds. In the "worst" case, new microscopic mechanisms would be needed, aspects of which appear oddly conventional (Bardeen-Cooper-Schreiffer). Again, two observations in 1UC FeSe/SrTiO$_3$ have created significant conundrum. First, like alkali-doped FeSe, its FS comprises only M electron pockets, apparently reducing the original multiband complexity. Second, the only bosonic mode to date with direct experimental support is an optical phonon mode at the SrTiO$_3$ interface.

In this section, we review complementary indications for phononic and electronic (spin/orbital) mechanisms of pairing. We then analyze ARPES and STM measurements that address superconductivity from the angle of gap symmetry and structure. Finally, we discuss multiband, multi-boson scenarios of pairing that enable phonons, spin fluctuations and nematic fluctuations (defined in subsection 3.3.2) to operate constructively and enhance T_c. These ideas are far from being a *fait accompli*, but embody an emerging theme in this field.

3.3.1 Phononic mechanisms

Phonons make a comeback?

Since the early 2008 days of Fe-SCs, phononic mechanisms of high-T_c in these systems have been largely discounted. DFT calculations suggested that the electron-phonon coupling λ in $LaFeAsO_{1-x}F_x$ was 5-6 times smaller than necessary to explain its T_c of 26 K [88, 85] (calculations with modified exchange-correlation functionals disagreed [80, 89]). In this light, it was somewhat ironic that 2014 ARPES measurements by Lee, Schmitt, Moore *et al.* [52] suggested a cross-interface, phonon-coupling mechanism of T_c enhancement in 1UC FeSe/$SrTiO_3$.

Replica bands

What Lee, Schmitt, Moore *et al.* discovered in their ARPES measurements was that each primary electronic band of 1UC FeSe/$SrTiO_3$ possessed a fainter replica band offset by 100 meV [52]. These faint bands were near-duplicates of their primary counterparts, even to the point of reproducing back-bending features induced by gap opening, without momentum offset or smearing [Fig. 3.7(a), (b)]. In addition, the replica bands persisted at least to 120 K, well above the gap-opening temperature ($T_c = 58 \pm 7$ K), and were absent in FeSe films two UC or thicker [Fig. 3.7(c), (d)].

In their interpretation of the replica bands, Lee, Schmitt, Moore *et al.* firstly excluded the possibility of quantum-well states arising from 2D confinement. There is no reason for such states to have identical dispersions or back-bending characteristics. Furthermore, quantum-well states exhibit a well-behaved dependence on layer, in contrast to the abrupt disappearance of replica bands in 2UC FeSe/$SrTiO_3$. Instead, the authors attributed the replica bands to bosonic shake-off, in analogy to vibrational shake-off observed in photoemission spectroscopy of H_2 molecules. They identified the boson with an optical O phonon band calculated for bulk $SrTiO_3$ [90]. Subsequent calculations of slab $SrTiO_3$ pointed to a surface phonon mode involving polar vibrations of vertical Ti-O bonds [91]. These theoretical comparisons were later corroborated by ARPES measurements [92] that also found replica bands on bare $\mathrm{SrTiO_3}$ [Fig. 3.7(e)]. However, for an electron-phonon coupling $g(\boldsymbol{q})$ to produce nearly-identical bands with no momentum smearing, it must be sharply peaked at $\boldsymbol{q} = 0$. This model assumption is nontrivial and will be assessed shortly.

Based on the shake-off interpretation, Lee, Schmitt, Moore *et al.* compared integrated intensities of the primary and replica bands and extracted a sizeable electron-phonon coupling constant of $\lambda = 0.5$. However, the procedure required a signifcant background substraction and was disputed by Peng *et al.*, citing matrix element effects [53].

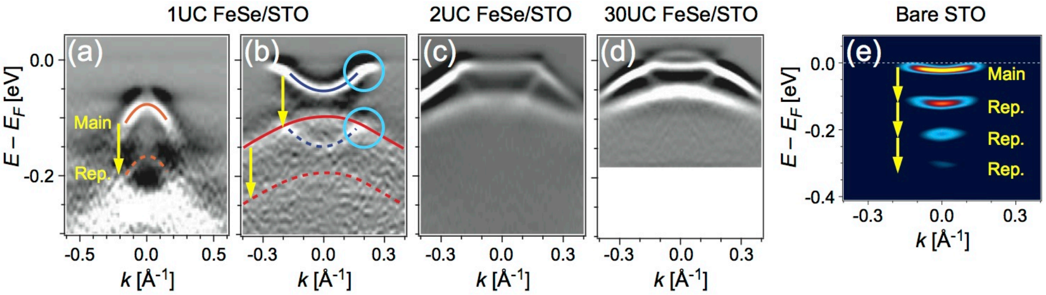

Figure 3.7: (a), (b) ARPES high-symmetry cuts of 1UC FeSe/$\mathrm{SrTiO_3}$ showing primary electronic bands and fainter replica bands offset by 100 meV (yellow arrows). These features suggest a $\boldsymbol{q} \sim 0$ coupling to a $\mathrm{SrTiO_3}$ phonon mode. The blue circles highlight the duplication of characteristic back-bending signatures due to SC gap opening. (c), (d) ARPES high-symmetry cuts of 2UC and 30UC FeSe/$\mathrm{SrTiO_3}$, showing the absence of replica bands. (a)-(d) are adapted from Ref. [52]. (e) ARPES curvature plot of bare $\mathrm{SrTiO_3}(001)$, displaying multiple replica bands offset by ∼100 meV. Adapted from Ref. [92].

Model of interface electron-phonon coupling

To explain how the electron-phonon coupling $g(\boldsymbol{q})$ could become sharply peaked at $\boldsymbol{q} = 0$, Lee, Schmitt, Moore *et al.* constructed the following model [52, 93]: Assume we have a 2D sheet of FeSe at $z = 0$, and a layer of dipole moments below at the $\mathrm{SrTiO_3}$ surface, $z = -h_0$. The dipole moments come from vertical displacements of surface Ti-O bonds and are represented by $\delta p_z(x, y, -h_0)$. These moments induce an electric potential at the FeSe layer,

$$\delta\Phi(x, y, 0) = \frac{\epsilon_{\|} h_0}{\epsilon_{\perp}^{3/2}} \int dx' dy' \frac{\delta p_z(x', y', -h_0)}{[\epsilon_{\|} h_0^2/\epsilon_{\perp} + (x - x')^2 + (y - y')^2]^{3/2}}, \tag{3.1}$$

where $\epsilon_{\|}$, $\epsilon_{\perp}$ are the in-plane and perpendicular dielectric constants in the interface region. Taking the Fourier transform yields

$$\delta\Phi(\boldsymbol{q}, 0) = \sqrt{\frac{\epsilon_{\|}}{\epsilon_{\perp}}} \frac{2\pi}{\sqrt{\epsilon_{\perp}}} \exp\left[- |\boldsymbol{q}| h_0 \sqrt{\epsilon_{\|}/\epsilon_{\perp}} \right] \delta p_z(\boldsymbol{q}, -h_0). \tag{3.2}$$

It follows that $g(\boldsymbol{q}) \propto \exp(-|\boldsymbol{q}|/q_0)$, where $q_0^{-1} = h_0\sqrt{\epsilon_{\|}/\epsilon_{\perp}}$. Intuitively, the $\boldsymbol{q} \sim 0$ coupling hinges upon (1) the FeSe monolayer being sufficiently removed from the dipole layer, and (2) the interface region screening lateral charge imbalance much more effectively than vertical charge imbalance.

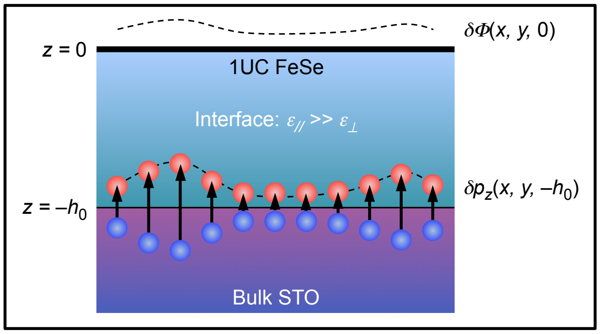

Figure 3.8: Model of interface electron-phonon coupling. We assume a 2D layer of FeSe at $z = 0$ and a layer of vertical dipole moments $\delta p_z(x, y, -h_0)$ at the SrTiO$_3$ surface, at $z = -h_0$. If the interface region has anisotropic dielectric constants, $\epsilon_{\|} \gg \epsilon_{\perp}$, then the induced electric potential $\delta\Phi$ is exponentially peaked at $\boldsymbol{q} = 0$.

Calculations by Rademaker *et al.* showed that a ratio of $q_0/k_F \sim 0.1$ was needed for replica bands to duplicate primary band features without significant momentum smearing [94]. If we take k_F to be 0.20 Å^{-1} [49] and h_0 to be 4.9 Å [73], the distance between the surface TiO$_2$ layer and the Fe-plane, then $1/(h_0 k_F) \sim 1$ and we require $\epsilon_{\|}/\epsilon_{\perp} \sim 100$ in the interface region. While one should be wary of interpreting the model interface too literally, an argument suggests that it should contain contributions from both $SrTiO_3$ and FeSe, with the former having $\epsilon_{\parallel}^{\text{STO}} \sim \epsilon_{\perp}^{\text{STO}}$ in its 3D bulk limit, and the latter having $\epsilon_{\parallel}^{\text{FeSe}} \gg \epsilon_{\perp}^{\text{FeSe}}$ due to its 2D nature [93]. In general, the anisotropy of the interface dielectric constant (suitably defined) remains challenging to verify experimentally or theoretically.

Alternative speculations regarding the replica bands include O impurity bands [95], or some form of Raman scattering involving $SrTiO_3$ phonon modes. No model details have been presented for impurity bands, and it is unclear whether there are sufficient cross-section and viable selection rules for Raman scattering involving the phonon mode in question. Peaks and dips have been detected in STM filled- and empty-state d^2I/dV^2 spectra (Supplemental Material of Ref. [96]), but the authors were unable to confirm their identity as replica bands.

3.3.2 Electronic mechanisms

Motivation

Are there any reasons to doubt a purely phononic mechanism of high-T_c superconductivity in 1UC FeSe/$SrTiO_3$? Experimentally, Lee, Schmitt, Moore *et al.* [52] observed distinct replica electronic bands that indicate a $\boldsymbol{q} \sim 0$ coupling to a $SrTiO_3$ phonon mode. Theoretically, Rademaker *et al.* show that such coupling can produce a quasi-linear scaling of T_c with the coupling constant λ, in contrast to the BCS scenario of an exponential decay $T_c \propto \exp(-1/\lambda)$ [94]. In this pure scenario, 1UC FeSe provides nothing essential. High-T_c superconductivity could possibly be realized in other 2D materials deposited on $SrTiO_3$, as long as they contribute to an anisotropic dielectric constant in the interface region.

Perhaps a more moderate viewpoint, which we now begin to explore, is that the interface phonons work in concert with some pre-existing electronic pairing mechanism in 1UC FeSe to boost T_c. The existence of an inherent electronic pairing glue is inferred from two foil systems. The first is an FeSe-intercalate, $(Li_{1-x}Fe_x)OHFeSe$, with a significant T_c of 40 K [97]. ARPES measurements resolved low-energy bands that are nearly identical to those of 1UC FeSe/$SrTiO_3$ and a nodeless gap of similar magnitude [98, 99]; however, no replica bands were visible. The second system is multilayer FeSe coated with K adatoms, which we next dicsuss in depth.

Potassium deposition on multilayer FeSe

Unraveling the microscopic role of $SrTiO_3$ has complications in that multiple effects may be present: electron doping from O vacancies, strain from lattice mismatch, and/or cross-interface phonon coupling. To isolate the role of electron doping, several groups instead examined the effects of depositing K adatoms on multilayer FeSe films [100, 101, 102]. They demonstrated that such films could become SC with gap-closing temperature as high as 48 K, close to 65 K for 1UC FeSe/$SrTiO_3$. Although details differed between experiments, two observations were unanimous: First, T_c followed a dome-shaped evolution over a narrow range of electron carrier densities ($n_e < 0.20$). Such domes are hallmarks of unconventional superconductivity, difficult to explain within a pure phononic scenario [95]. Second, T_c emerged upon suppression of a parent nematic phase [Fig. 3.9], characterized in multilayer FeSe by a small orthorhombic distortion [103] and a large splitting of the Fe $3d_{xz}$ and $3d_{yz}$ bands [51, 104, 105, 106, 107, 108]. By analogy to other unconventional superconductors, one might expect pairing in electron-doped multilayer FeSe to be mediated by fluctuations of the parent order; i.e., nematic fluctuations.

Nematic order breaks rotational symmetry while preserving translational symmetry. As a result of the latter, nematic fluctuations provide effective $\boldsymbol{q} \sim 0$ attractive interactions, much like the aforementioned interface phonons. Various theories have demonstrated the effectiveness of nematic fluctuations in boosting T_c irrespective of pairing symmetry, especially in 2D systems [112, 113, 114]. But are there signs of such fluctuations in (1) electron-doped multilayer FeSe or (2) 1UC FeSe/$SrTiO_3$? Ye *et al.* made a positive claim in the former [102]. During K deposition on multilayer FeSe, the authors resolved ARPES signals of both doped bands from the surface FeSe layer, and bulk bands from the undoped layers below. With the doped bands, a remnant nematic splitting persisted with the emergence of superconductiv-

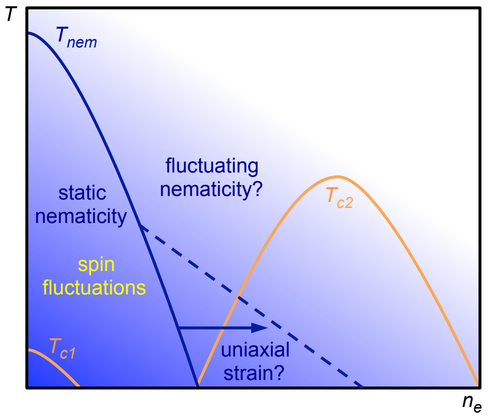

Figure 3.9: Schematic phase diagram of electron-doped multilayer FeSe, highlighting two disparate domes of superconductivity, and the possibility of nematic fluctuations. Adapted from Refs. [100, 101, 102, 83]. The existence of spin fluctuations in stoichiometric FeSe was detected by Ref. [109, 110, 111].

ity, up to 0.10 electron carriers per Fe. The authors suggested that the nematic fluctuations in the surface layer were being stabilized by uniaxial strain from the undoped, orthorhombic layers below (dashed line Fig. 3.9).

Before addressing the possiblity of nematic fluctuations in 1UC FeSe/SrTiO$_3$, we highlight additional features in the phase diagram of electron-doped multilayer FeSe, which remain open to theoretical investigation. The electron doping evolution is marked by non-rigid band transformations, including two Lifshitz transitions of a Γ hole pocket and an M electron pocket [102] respectively. STM experiments [83] also revealed two disparate domes of superconductivity (T_{c1} and T_{c2}). T_{c1} coexists with nematic order in stoichiometric FeSe. It has a nodal gap of magnitude $\Delta \sim 2$ meV. T_{c2} arises upon sufficient electron doping, and has a nodelss gap of magnitude $\Delta \sim 14$ meV.

Search for nematic fluctuations in 1UC FeSe/SrTiO$_3$

As a local probe, STM can clarify whether disorder or anisotropic perturbations pin nanoscale patches of otherwise-fluctuating nematicity. Previous measurements of other Fe-SCs have detected remnant, nematic electronic signatures above the spin-density-wave transition temperature in NaFeAs [115], or the nominally tetragonal phase of $FeSe_{0.4}Te_{0.6}$ [116].

To investigate the possibility of nematic fluctuations in monolayer $FeSe/SrTiO_3$, Huang *et al.* examined anisotropies in low-energy quasiparticle interference (QPI) patterns due to scattering between electron Fermi pocket states [117]. The authors developed a T-matrix model of multi-orbital QPI to disentangle scattering intensities from Fe $3d_{xz}$ and $3d_{yz}$ bands. By sampling multiple spatial regions of a 1UC $FeSe/SrTiO_3$ film, they excluded static xz/yz orbital ordering with domain size larger than $\delta r^2 = 20$ nm × 20 nm, xz/yz Fermi wave vector difference larger than $\delta k = 0.014\ \pi$, and energy splitting larger than $\delta E = 3.5$ meV. The lack of detectable ordering pinned around defects suggests that there is no proximate nematicity in 1UC $FeSe/SrTiO_3$, in contrast to electron-doped multilayer FeSe.

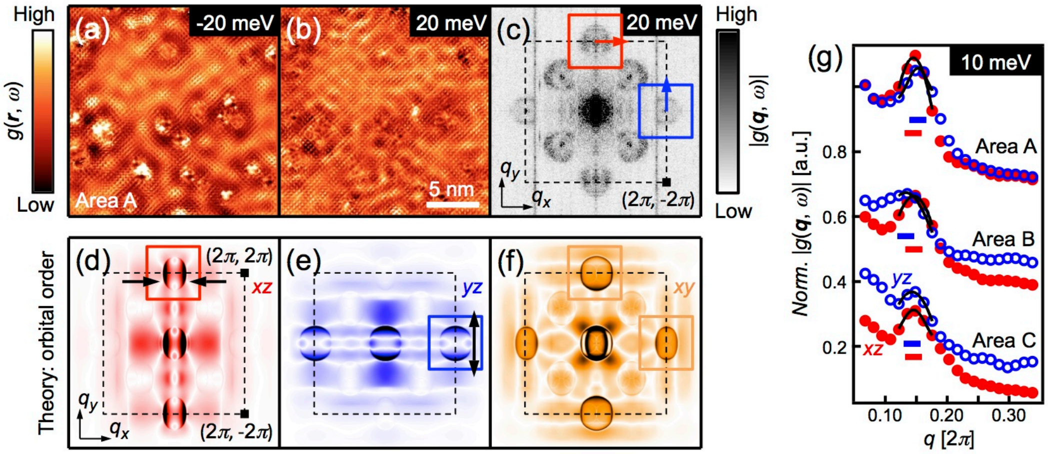

Figure 3.10: Nanoscale wave vector analysis of orbital nematicity via STM. (a), (b) Differential tunneling conductance maps $g(\boldsymbol{r}, \omega)$ over a defect region of 1UC $FeSe/SrTiO_3$, revealing dispersive QPI patterns. (c) Fourier transform amplitude $|g(\boldsymbol{q}, \omega)|$ of (b), revealing ring-like intensities that arise from scattering between Fermi electron pocket states. Note that fourfold rotational symmetrization has not been applied. The red and blue boxes enclose the ring-like intensities that arise primarily from scattering of Fe $3d_{xz}$ and $3d_{yz}$ states respectively. (d)-(f) T-matrix calculations of QPI patterns, decomposed into dominant orbital contributions. In the presence of xz/yz orbital ordering, the rings enclosed in the red and blue boxes contract and expand respectively, and are no longer 90° rotations of each other. (g) Line cuts across the arrows in (c), used to compare xz/yz scattering wave vectors. Measurements are acquired over a few distinct domains ($\delta r^2 = 20$ nm × 20 nm). The horizontal bars mark the peak locations determined from Gaussian fits (solid lines), with inherent resolution $\delta q = 0.028\ \pi$. Within these bounds, no signatures of nematicity were detected. Adapted from Ref. [117].

MAGNETISM: AN OPEN QUESTION

Besides nematic fluctuations, what are alternative electronic mechanisms of pairing that could operate in 1UC FeSe/SrTiO$_3$? Several inelastic neutron scattering (INS) measurements revealed that in stoichiometric FeSe, there are stripe spin fluctuations that are enhanced below the orthorhombic transition temperature [109, 110, 111]. However, magnetic order is absent, owing to some sort of frustration [118, 119]. The nature of spin excitations in 1UC FeSe/SrTiO$_3$ remains an important open question, especially since both doping and lattice strain may tune exchange interactions. Some experimental ingenuity is required, as *ex-situ* INS measurements are probably not feasible on 1UC films.

3.3.3 GAP SYMMETRY AND STRUCTURE

We shift gears and discuss pairing from the viewpoint of gap symmetry and structure. Unlike the cuprates, in which $d_{x^2-y^2}$ gap symmetry is universal and well-established, the Fe-SCs possess a variety of gap structures across their member compounds. In addition, many candidate gap functions share identical angular symmetries (for example, s_{+-}, s_{++}, and "bonding-antibonding" s), complicating the task of differentiating them [120]. In general, the interpretation of phase-sensitive measurements is dependent on modeling assumptions; thus, there is unlikely to be a "smoking gun" experiment, despite widespread and adamant claims of such. A more likely scenario is that through multiple experimental measurements, consensus begins to converge upon a candidate gap function.

THE CANDIDATES

Given the sunken hole pocket at the zone corner (see subsection 3.1.2), the primary gap symmetry candidates are "plain" s, "nodeless" $d_{x^2-y^2}$, "bonding-antibonding" s, and "incipient" s_{+-}. We proceed with two words of caution:

1. *"Definition basis"* - The comparison between the aforementioned gap symmetry can-

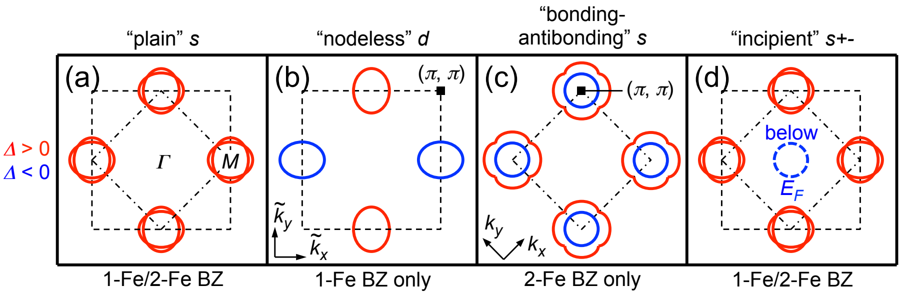

Figure 3.11: Pairing symmetry candidates for 1UC FeSe/SrTiO$_3$. Note that some structures are defined only within a 1-Fe BZ ($\tilde{\boldsymbol{k}}$) or 2-Fe BZ ($\boldsymbol{k}$), whereas others are indifferent to folding. "Incipient" s_{+-} suggests that a sunken hole pocket at the zone center can host an opposite-sign gap.

didates is not "apples to apples," since the candidates are not all defined in the same momentum space. For example, "nodeless" $d_{x^2-y^2}$ is strictly defined in a 1-Fe, pseudocrystal momentum BZ ($\tilde{\boldsymbol{k}}^{1\text{Fe}}$), where glide-plane symmetry is an exact symmetry of the system [Fig. 3.11(b)]. On the other hand, "bonding-antibonding" s, which hinges upon hybridization of the M electron pockets, is only well-posed in a 2-Fe, crystal momentum BZ ($\boldsymbol{k}^{2\text{Fe}}$) [Fig. 3.11(c)].

2. *"Measurement basis"* - ARPES and STM are leading probes of gap structure, since they provide momentum resolution. However, it is crucial to keep in mind what sort of momentum or basis they probe:

   (a) ARPES measures the free-space momentum $\boldsymbol{p}$ of final-state photons, which Ku argues is best approximated by the 1-Fe crystal momentum $\boldsymbol{k}^{1\text{Fe}}$ [121, 122]. Thus, the ARPES intensity $I(\boldsymbol{p}, \omega)$ most closely resembles the theoretical spectral function $A(\boldsymbol{k}^{1\text{Fe}}, \omega)$, even though quasiparticles are not defined in this momentum space.

   (b) STM momentum resolution is derived from applying a discrete Fourier transform $|g(\boldsymbol{q}, \omega)|$ to a conductance map $g(\boldsymbol{r}, \omega)$. The classic octet model for cuprates posits that $\boldsymbol{q}$ is the scattering wave vector connecting isoenergetic segments of band structure. The multi-orbital nature of Fe-SCs produces three pitfalls with

> a naive extension of the octet model: (1) Not all orbital combinations have equal scattering amplitudes, (2) not all orbitals have equal tunneling amplitudes, and (3) in a 2-Fe UC space, the symmetric and anti-symmetric combinations of orbitals on the two Fe sites do not have equal tunneling amplitudes. There is a disconnect between the Bogoliubov quasiparticles, which reside in band space, and their scattering and tunneling which are better described in orbital space [123, 117].

As already mentioned, “nodeless” $d_{x^2-y^2}$ is strictly defined in a 1-Fe, pseudocrystal momentum BZ [Fig. 3.11(b)]. Quasinodes will be created upon folding [124]. However, the nodal quasiparticle weight depends on the folding strength, which could be weak, possibly eluding spectroscopic detection [125, 126]. If significant hybridization at the 2-Fe BZ boundary is present, nodes may be avoided, leading to a “bonding-antibonding” s pairing symmetry candidate [Fig. 3.11(c)]. Incipient s_{+-} posits that an opposite-sign gap is formed on the sunken zone center hole pocket [Fig. 3.11(d)]. This can be sizeable, contrary to usual expectations, if there are additional intraband interactions operating within the FS electron pockets (subsection 3.3.4) [127].

Gap anisotropy (ARPES)

Early ARPES measurements of 1UC FeSe/SrTiO$_3$ reported an isotropic gap ($\Delta = 13{-}15$ meV) on nearly-circular electron pockets [49, 50, 51, 52]. Later, by expanding the lattice constant (1UC FeSe/SrTiO$_3$/KTaO$_3$) or by changing photon polarization, Peng *et al.* [55] and Zhang *et al.* [79] were able to resolve the ellipticity of the electron pockets, as well as their folded counterparts at each zone corner. Two observations were crucial. First, the authors in both cases observed no signs of hybridization, within their instrument resolution. Momentum distribution cuts across the overlap region of the main and folded pockets reveal a single band, with no splitting. Furthermore, gap measurements on corresponding segments of the main and folded pockets were nearly identical. The lack of sizeable hybridization may be somewhat unexpected, given that both spin-orbit coupling or the $SrTiO_3$ substrate might be expected to break glide-plane symmetry. The absence of hybridization would also rule out the “bonding-antibonding” *s* scenario. Second, the authors resolved an anisotropic gap on the elliptical pockets, with minima directed along the Fe-Se axes. These measurements will provide useful feedback for theoretical gap function calculations.

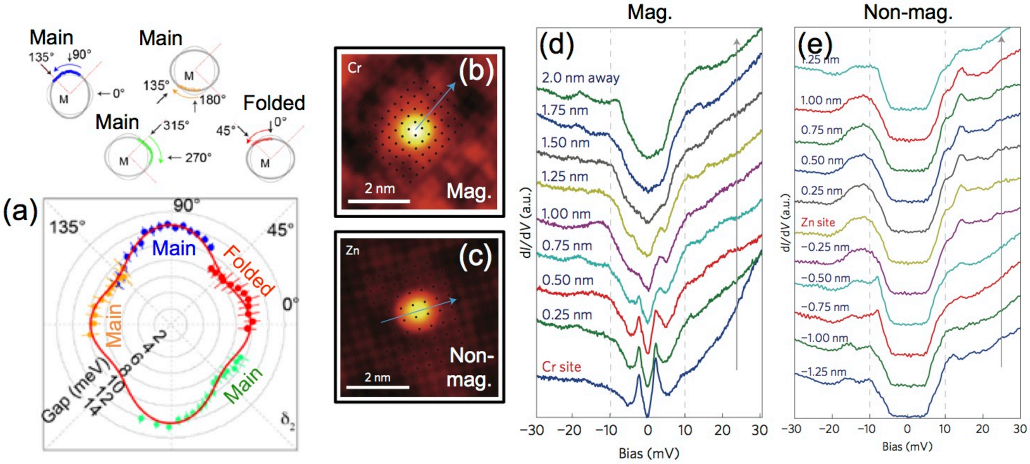

Figure 3.12: (a) ARPES measurements of gap anisotropy, on both the main and folded electron pockets. There are no signs of hybridization that would support a “bonding-antibonding” *s* scenario. Adapted from Ref. [79]. (b)-(e) STM dI/dV line cuts across magnetic (Cr) and non-magnetic (Zn) adatoms, revealing suppression of the SC gap and production of in-gap states in the former (Cr), but no changes in the latter (Zn). These observations are suggestive of *s*-wave superconductivity. Adapted from Ref. [76].

Phase-sensitive measurements (STM)

Fan *et al.* employed a multi-pronged STM approach to build support for “plain” *s*-wave superconductivity in 1UC FeSe/$SrTiO_3$ [76]. Their conclusion was based on the following three observations:

1. All observed scattering intensities in QPI measurements exhibited similar energy evolutions across the gap energy.

2. All observed scattering intensities in QPI measurements exhibited similar magnetic-field dependencies between 0 T and 11 T.
3. Deposited magnetic adatoms (Cr, Mn) induced in-gap bound states, while deposited non-magnetic adatoms did not (Zn, Ag, K).

As Fan *et al.* discuss, the interpretations of the first two observations are somewhat model-dependent. There are complexities related to proper signal normalization [128], or the nature of vortex scattering [129]. The third observation is apparently consistent with Anderson's theorem for a gap structure without sign changes, but not without a caveat. While the observation of in-gap states due to a non-magnetic impurity signals a sign-changing gap, the inverse is untrue: the lack of in-gap states due to a non-magnetic impurity does not imply that the gap has no sign changes [120, 130]. In the case of "nodeless" $d_{x^2-y^2}$ and "bonding-antibonding" s pairing symmetries, opposite-sign gaps arise from normal-state Fermi sheets with different orbital characters. Given that the impurities in the Fan *et al.* experiment were adatomic, they may have had insufficient interorbital scattering strength to produce a pair-breaking effect (*cf.* Ye *et al.* show that out-of-plane, non-magnetic impurities do not decrease quasiparticle lifetime [131]). Nevertheless, the sum total of all the observations presented by Fan *et al.* does favor s-wave gap symmetry.

3.3.4 Multiband, multi-boson scenarios

In this final subsection, we discuss possible pairing scenarios involving multiple bosons working cooperatively within a multiband environment to enhance T_c in 1UC FeSe/SrTiO$_3$ [52]. These scenarios represent a framework in which many different lines of thought can be unified, but also remain open to experimental verification. The critical question we consider is how to fit attractive interactions (e.g., mediated by phonons) and repulsive interactions (e.g., mediated by spin fluctuations) under the same roof. Here, we review an intuitive picture derived from the weak-coupling limit, but note that strong-coupling generalizations enabled by quantum Monte Carlo simulations are also possible [132, 133].

We begin with the Bardeen-Cooper-Schrieffer (BCS) gap equation:

$$\Delta_{\boldsymbol{k}} = -\sum_{\boldsymbol{k}'} \frac{V(\boldsymbol{k}-\boldsymbol{k}')\Delta_{\boldsymbol{k}'}}{2E_{\boldsymbol{k}'}}. \tag{3.3}$$

Any gap function $\Delta_{\boldsymbol{k}}$ must be a self-consistent solution to Eq. 3.3, where $V(\boldsymbol{k}-\boldsymbol{k}')$ is the effective pairing interaction and $E_{\boldsymbol{k}'} = \sqrt{\xi_{\boldsymbol{k}'}^2 + |\Delta_{\boldsymbol{k}'}^2|} > 0$, with $\xi_{\boldsymbol{k}'}$ being the normal-state quasiparticle dispersion. We can then arrive at the following conclusions:

1. Attractive interactions boost pairing if they connect segments of the FS hosting same-sign gaps.
2. Repulsive interactions boost pairing if they connect segments of the FS hosting opposite-sign gaps.
3. One can engineer a situation in which both attractive and repulsive interactions boost pairing, if the interactions connect different segments of the FS.

In this context, the multiband nature of Fe-SCs and their disparate Fermi pockets become advantageous. One can envision having attractive intraband interactions that stabilize a uniform-sign gap within a given Fermi pocket, then repulsive interband interactions that force two disparate Fermi pockets to have opposite-sign gaps. In the forward-scattering limit (i.e., $\boldsymbol{q} = (0, 0)$), attractive intraband interactions universally boost pairing irrespective of the gap function.

Figure 3.13 illustrates a pairing framework for 1UC FeSe/SrTiO$_3$ involving multiple bosons. We suppose that there exists a “primary” interband pairing interaction peaked around $\boldsymbol{q} = (\pi, \pi)$, which connects the disparate corner electron pockets and dictates the overall gap symmetry. This could be a repulsive antiferromagnetic spin fluctuation, stabilizing d-wave pairing, or an attractive antiferro-orbital fluctuation [132, 133], stabilizing s-wave pairing. (For simplicity, we restrict ourselves to the 1-Fe, pseudocrystal momentum BZ.) Then in addition, there may be “enhancer” intraband interactions that are necessarily attractive and peaked around $\boldsymbol{q} = (0, 0)$. These interactions universally boost pairing and can come in the form of $\mathrm{SrTiO_3}$ interface phonons, or nematic fluctuations.

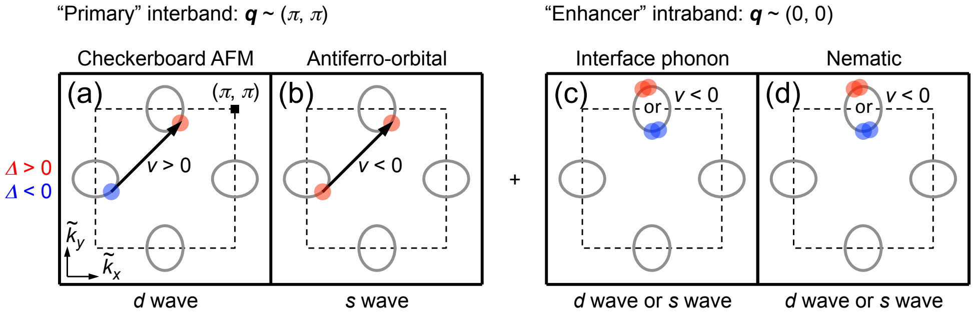

Figure 3.13: Multiband, multi-boson scenarios of pairing in 1UC $\mathrm{FeSe/SrTiO_3}$. For simplicity, we work in a 1-Fe, pseudocrystal momentum BZ. (a), (b) In this picture, the pairing symmetry is determined by a "primary" interband interaction, peaked at $\boldsymbol{q} = (\pi, \pi)$. (c), (d) In addition, there are "enhancer" intraband interactions that can further boost T_c irrespective of gap function, due to their forward scattering nature (peaked at $\boldsymbol{q} = (0, 0)$).

We reiterate that the pairing interactions in 1UC $\mathrm{FeSe/SrTiO_3}$ remain largely unknown at this point. No experiments have uncovered any interband pairing interactions. INS, a powerful probe of spin excitations, is difficult to impossible for a monolayer film. STM has not found any signatures of nematic fluctuations. ARPES has detected replica electronic bands, which is best explained in terms of coupling to an interface phonon mode.

PAIRING INVOLVING INCIPIENT BANDS

We review another multiband, multi-boson scenario proposed by Chen *et al.* [127]. The authors were motivated by ARPES measurements in LiFeAs that resolved a SC gap on a "incipient" hole pocket 10 meV below E_F [134]. Although several strong-coupling interpretations of this observation were put forth, Chen *et al.* developed a simpler, weak-coupling explanation. In isolation, interactions between a Fermi sheet and an incipient band do not open up a SC gap. However, if there is a pre-existing interaction that stabilizes a small gap on that sheet, then its interactions with incipient bands can enhance pairing.

Based on this finding, Chen *et al.* proposed a "dark horse" pairing symmetry candidate for 1UC FeSe/SrTiO$_3$: "incipient" s_{+-}. First, there is an intraband, interface phonon that opens up a small SC gap on the corner electron pockets. Second, a presumed $\boldsymbol{q} = (\pi, 0)$ spin fluctuation that exists in stoichiometric FeSe can then "bootstrap" to the pre-existing gap and produce an opposite-sign gap on the sunken hole pocket. From their model calculations, this spin fluctuation can boost T_c by an order of magnitude, although numbers are sensitive to estimates of interaction strengths and cutoff. Importantly, Chen *et al.* also argued that an "incipient" s_{+-} pairing symmetry could be consistent with impurity experiments by Fan *et al.* [76]. Since defects primarily induce elastic scattering, there is not much mixture of quasiparticles from the electron Fermi pockets and sunken hole pockets with opposite-sign gaps.

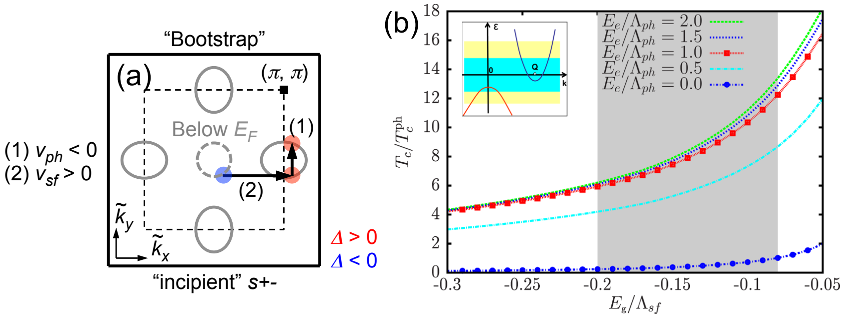

Figure 3.14: (a) Schematic of a multi-boson, "bootstrap" mechanism of pairing. First, there are attractive intraband interactions, such as a $\boldsymbol{q} \sim 0$ phonon coupling, which stabilize a same-sign gap within the Fermi pockets. Second, repulsive interband interactions, such as $\boldsymbol{q} = (\pi, 0)$ stripe fluctuations, can "bootstrap" to the existing gap and open an additional gap on the sunken hole pocket below E_F. (b) Model calculations of T_c enhancement within the "incipient" s_{+-} scenario. Inset: the cutoff ranges for model phonons and spin fluctuations are indicated by the shaded blue and yellow regions. Adapted from Ref. [127].

Recently, Huang *et al.* uncovered a Γ electron pocket 80 meV above E_F, using empty-state STM measurements [96]. This pocket may be similar to one discovered in bulk FeSe$_{0.55}$Te$_{0.45}$ [135], or a shallow Z-electron Fermi pocket in 3D (Tl, Rb)$_y$Fe$_{2-x}$Se$_2$ [136]. Given that this pocket lies within the interface phonon cut-off, it may be interesting to explore whether it has any positive contribution to T_c in 1UC FeSe/SrTiO$_3$.

4

Revealing the Empty-State Electronic Structure of Single-Unit-Cell FeSe/SrTiO$_3$

We use scanning tunneling spectroscopy to investigate the filled and empty electronic states of superconducting single-unit-cell FeSe deposited on SrTiO$_3$(001). We map the momentum-space band structure by combining quasiparticle interference imaging with decay length spectroscopy. In addition to quantifying the filled-state bands, we discover a Γ-centered electron pocket 75 meV above the Fermi energy. Our density functional theory calculations show the orbital nature of empty states at Γ and explain how the Se height is a key tuning parameter of their energies, with broad implications for electronic properties.

4.1 INTRODUCTION

The extraordinary potential of interface engineering to generate novel electronic properties is exemplified by a single unit cell (1UC) of FeSe deposited on $SrTiO_3$ [1], which exhibits an order-of-magnitude increase in its superconducting transition temperature (T_c up to 110 K [2]) compared to bulk FeSe ($T_c = 9.4$ K [137]). Not only does this finding elevate the T_c of iron-based superconductors (Fe-SCs) above the liquid nitrogen temperature, it also opens the door to designing Fe-SC/oxide heterostructures with novel phases and yet higher T_c. A key to understanding and realizing these phases is a complete measurement of the electronic structure of filled and empty states.

Electronic band structure is pivotal in determining the pairing symmetry of Fe-SCs. The generic Fermi surface (FS) of Fe-SCs consists of electron pockets at the Brillouin zone (BZ) corner M and hole pockets at the zone center Γ [138]. A prevalent spin-fluctuation model suggests that repulsive antiferromagnetic excitations of wave vector (π, π) can give rise to pairing between the electron and hole pockets if the order parameter reverses sign, resulting in s_{+-} superconductivity [85, 86]. However, in 1UC FeSe/$SrTiO_3$, the Γ hole pocket sinks entirely below the Fermi energy (E_F) due to electron doping [49]. This challenges the s_{+-} picture; nevertheless, functional renormalization group (FRG) calculations have shown that electronic bands lying within the spin fluctuation energy scale below E_F can still influence the pairing channel. In fact, the energy of the sunken Γ hole pocket is predicted to toggle the relative stability between sign-preserving s_{++} and sign-changing d pairing symmetries [139, 140].

A natural question is whether low-lying bands above E_F can similarly renormalize the effective interaction. In general, the landscape of empty states in Fe-SCs remains largely unexplored by experiment. A full band structure mapping is particularly crucial in 1UC FeSe/$SrTiO_3$, where in addition to the usual Coulomb repulsion and spin fluctuations, even higher energy phonon modes may be at play [140, 52, 80], and the magnitudes of their energy scales relative to the near-E_F bands determine the superconducting ground state.

Here we map the multiband electronic structure of 1UC FeSe/$SrTiO_3$ by two complimentary scanning tunneling microscopy (STM) techniques: (1) quasiparticle interference (QPI) imaging [141] and (2) decay length spectroscopy [142]. In the first technique, impurity scattering of quasiparticles generates interference patterns with characteristic dispersive wave vectors $\boldsymbol{q}(\omega)$ that can be inverted to reconstruct the band structure. Since $\boldsymbol{q}$ is the momentum transfer, QPI imaging resolves only *relative* momentum coordinates between two states. In the second technique, the *absolute*, in-plane momentum $k_{||}$ of quasiparticles can be extracted from the decay of their tunneling current with increasing sample-tip separation. By combining the two momentum-resolved techniques, we discover a Γ electron pocket 75 meV above E_F. Our density functional theory (DFT) calculations reproduce the presence of empty states at Γ, and furthermore explain how their energies are tuned by the Se height h_{Se}.

4.2 Experiment

We grew films of FeSe on Nb-doped $SrTiO_3(001)$ (0.5%) via molecular beam epitaxy (MBE). The substrates were pretreated with deionized water for 90 min at 80 °C, followed by an O_2-anneal for 3 h at 1000 °C. We then transferred the substrates into our MBE chamber (base pressure 1×10^{-10} Torr) and degassed them at 670 °C. We deposited FeSe by co-evaporating Fe (99.995%) and Se (99.999%) with a molar flux ratio of 1:6 and substrate temperature 520 °C. Afterwards, we typically annealed the samples for an additional 2 h between 500–600°C before transferring them through ultra-high vacuum to a home-built STM for imaging at ∼4.3 K.

Figure 4.1(a) shows a typical film topography, with regions of bare $SrTiO_3$ and 1UC or 2UC of FeSe. We discriminate these regions based on their terrace heights. From the line cut in Fig. 4.1(b), we observe a 3UC $SrTiO_3$ step to be 1.19 ± 0.05 nm (bulk c-axis lattice constant is 0.3905 nm [47]), the 1–2UC FeSe step to be 0.57 ± 0.05 nm, and the bare $SrTiO_3$–1UC FeSe step to be 0.34 ± 0.02 nm (all measured at 4 V sample-tip bias). We will hereafter focus on the 1UC FeSe terraces. Figure 4.1(c) presents an atomically-resolved topography of 1UC

FeSe, with lattice constant $a = 3.9$ Å. Each bright spot corresponds to a surface Se atom in a Se-Fe-Se triple layer. A representative dI/dV spectrum on a clean area exhibits a gap of $\Delta = 14$ meV [Fig. 4.1(d)], similar in magnitude to other reports of superconducting gaps in this material [49, 54]. We note appreciable spectral inhomogeneity in 1UC FeSe/SrTiO$_3$, but further study is needed to quantify its correlation with substrate disorder.

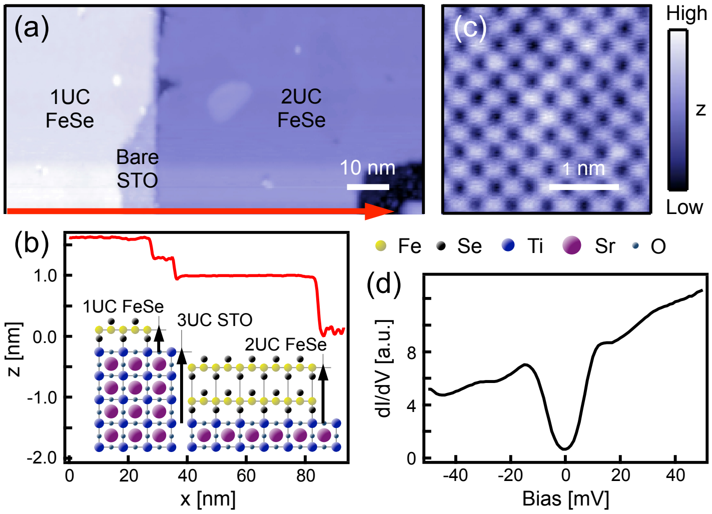

Figure 4.1: (a) Typical topography of *in-situ*-grown FeSe/SrTiO$_3$. Setpoint: 4 V, 5 pA. (b) Line cut along the arrow in (a). The inset illustrates the underlying crystal structure. (c) Atomically-resolved topography of single-unit-cell (1UC) FeSe/SrTiO$_3$. Setpoint: 50 mV, 250 pA. (d) dI/dV spectrum of 1UC FeSe/SrTiO$_3$, T = 4.3 K. Bias oscillation $V_{\text{rms}} = 0.7$ mV.

To image QPI, we acquired conductance maps $g(\boldsymbol{r}, \omega) = dI/dV(\boldsymbol{r}, eV)$ over flat regions of 1UC FeSe/SrTiO$_3$ with moderate concentrations of as-grown defects [Fig. 4.2(a)]. Several energy maps of one representative region are presented in Figs. 4.2(b)-(e), displaying clearly dispersive interference patterns. To identify the momentum-space origin of the scattered quasiparticles, we compared the Fourier transform amplitudes $|g(\boldsymbol{q}, \omega)|$ to simulated autocorrelations of the spectral function $A(\boldsymbol{k}, \omega) = -\frac{1}{\pi}\sum_\alpha \mathrm{Im}[G_\alpha(\boldsymbol{k}, \omega)]$ [143]. For simplicity, we used the bare Green's function $G_\alpha^{-1}(\boldsymbol{k}, \omega) = \omega + i\delta - \varepsilon_\alpha(\boldsymbol{k})$, with parabolic bands $\varepsilon_\alpha(\boldsymbol{k})$ and broadening $\delta = 5$ meV. The main result is presented in Figs. 4.3(a)-(i), which compare $|g(\boldsymbol{q}, \omega)|$ to theoretical predictions for three representative energies. We discuss each in turn:

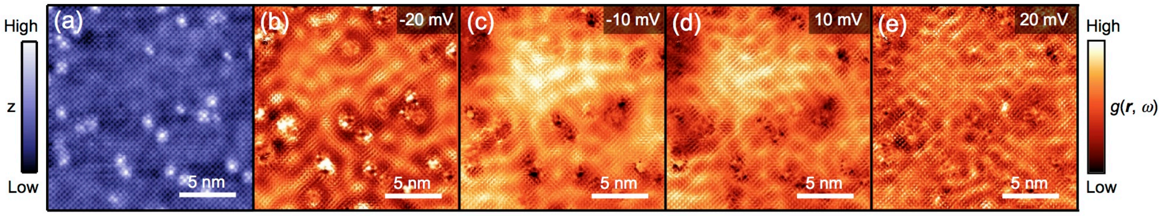

Figure 4.2: Quasiparticle interference imaging, real space. (a) Topography (setpoint: 50 mV, 500 pA) and (b)-(e) conductance maps $g(\mathbf{r},\omega)$ (setpoint: 100 MΩ, $V_{\mathrm{rms}} = 1.4$ mV) of a 20 nm x 20 nm field of view with as-grown defects. Images were drift-corrected following Ref. [144].

$\omega = 10$ meV, Figs. 4.3(b), (e), (h): Close to E_F, we observe 9 ring-like intensities in $|g(\boldsymbol{q},\omega)|$, centered about reciprocal lattice vectors $\boldsymbol{G} = (0, 0)$, $(\pm 2\pi/\mathrm{a}, 0)$, $(0, \pm 2\pi/\mathrm{a})$, and $(\pm 2\pi/\mathrm{a}, \pm 2\pi/\mathrm{a})$. These intensities arise from scattering, modulo $\boldsymbol{G}$, within electron Fermi pockets at the zone corner M (labeled 1 in Fig. 4.3) [49].

$\omega = -66$ meV, Figs. 4.3(c), (f, (i): Sufficiently below E_F, we observe additional scattering channels pointing to the emergence of the Γ hole pocket seen by angle-resolved photoemission spectroscopy (ARPES) [49]. Intrapocket scattering between Γ pockets is labeled 2 in Fig. 4.3, while interpocket scattering between Γ and M pockets is labeled 1–2 in Fig. 4.3.

$\omega = 80$ meV, Figs. 4.3(a), (d), (g): Above E_F, we discover a third pocket. Intrapocket scattering (labeled 3 in Fig. 4.3) is clearly resolved in $|g(\boldsymbol{q},\omega)|$, but interpocket scattering with the M electron pockets (expected intensity at $(\pi/a, \pi/a)$ modulo $\boldsymbol{G}$) appears to be suppressed. In general, the autocorrelation of $A(\boldsymbol{k},\omega)$ yields the set of all possible scattering channels, but more complex theories that encode spin [145] or orbital [146] selectivity in the scattering T-matrix are needed to explain their relative intensities. In this case, the empirical suppression of Γ–M scattering leaves some ambiguity as to the absolute momentum ($\boldsymbol{k}$) location of the new pocket.

To visualize the full QPI evolution, Fig. 4.3(j) shows an azimuthally-averaged intensity plot of $|g(q_r,\omega)|$, where q_r is measured relative to $\boldsymbol{G} = (2\pi/a, 0)$ as shown in Fig. 4.3(h). In total, we observe three dispersing branches: two electron-like (labeled 1 and 3) and one hole-like (labeled 2). Branches 1 and 2 correspond to a M electron pocket and a Γ hole pocket,

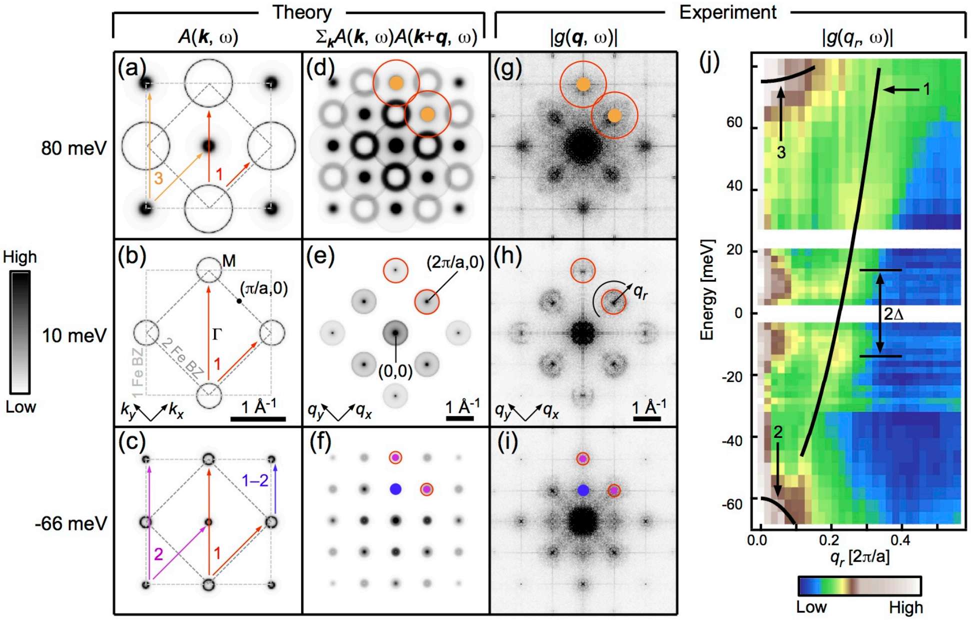

Figure 4.3: Quasiparticle interference imaging, momentum transfer ($\boldsymbol{q}$) space. (a)-(f) Theoretical simulations, $A(\boldsymbol{k},\omega)$ and its autocorrelation, for three representative energies. (g)-(i) Fourier transform amplitudes $|g(\boldsymbol{q},\omega)|$ of conductance maps (four-fold symmetrized for increased signal). (j) Azimuthally-averaged intensity plot of $|g(q_r,\omega)|$, where q_r is measured relative to $\boldsymbol{G} = (2\pi/a, 0)$. The superconducting gap is marked by 2Δ.

while branch 3 awaits further identification. A parabolic fit to branch 1 over the given energy range in Fig. 4.3(j) yields an effective mass enhancement $m^*/m = 2.0 \pm 0.1$ and a carrier concentration of 0.08 e^- per Fe from a Luttinger count, assuming a degenerate pocket [49].

To determine the absolute momentum $\boldsymbol{k}$ of QPI branch 3, a complimentary momentum-resolved STM technique is needed. Here we utilize decay length spectroscopy [142, 147, 148], a general tool which allows the full reconstruction of $\boldsymbol{k}$-space band structure from STM. Tersoff and Hamman [149] showed that a sample state of in-plane momentum $\boldsymbol{k}_{||}$ has density which decays towards the vacuum with length λ given by

$$\frac{1}{(2\lambda)^2} = \frac{2m\Phi}{\hbar^2} + k_{||}^2, \qquad (4.1)$$

where Φ is the average of the sample and tip work functions. Figures 4.4(a), (b) show the energy dependent decay length $\lambda(\omega)$, extracted from exponential fits to the tunneling current as the sample-tip distance is increased at a fixed bias. Near E_F, the sample states have large momentum near M and smaller decay length. Below E_F, a steep increase in $\lambda(\omega)$ accompanies the onset of a hole pocket at Γ, as states with low momentum become available for tunneling. The fact that a similar rise in $\lambda(\omega)$ occurs above E_F indicates that branch 3 in Fig. 4.3(j) is also located at Γ. If we interpret the large-$|\omega|$ value of $\lambda = 0.462 \pm 0.001$ Å as arising from states with $\boldsymbol{k} \approx 0$, we find $\Phi = 4.46 \pm 0.03$ eV from Eq. (4.1), then we can compute the expected $\lambda(\omega) = 0.318 \pm 0.001$ Å for energies where the only states come from momenta near M. Indeed, the measured $\lambda(\omega)$ at small $|\omega|$ closely matches the expected value of $\lambda(|\boldsymbol{k}| = \sqrt{2}\pi/a)$. Step-like features associated with the onsets of these pockets are also detected with dI/dV spectroscopy [Fig. 4.4(c)]. From extrema in the numerical derivative d^2I/dV^2, which closely match those of $d\lambda/d\omega$ [vertical shaded guides in Figs. 4.4(b), (c)], the band edges of the Γ hole and electron pockets are -65 meV and 75 meV.

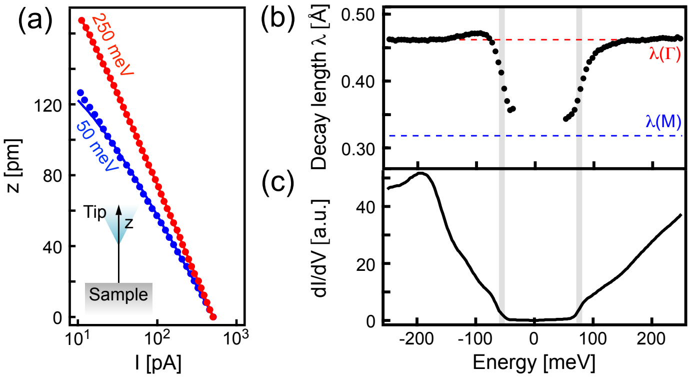

Figure 4.4: (a), (b) Energy dependent decay length $\lambda(\omega)$, extracted from exponential fits to the tunneling current as the tip is retracted from the sample at a fixed bias (inset schematic). Fits were performed in the current range [10 pA, 500 pA], two of which (250 meV and 50 meV) are shown in (a). Dashed horizontal lines indicate calculated values of λ at the Γ and M. (c) dI/dV spectrum. $V_{\mathrm{rms}} = 2.8$ mV. Vertical lines mark extrema in the numerical derivatives of $\lambda(\omega)$ and dI/dV.

4.3 Theory and Discussion

A consistent band structure for 1UC FeSe/SrTiO$_3$ is now established, comprising M electron pockets spanning E_F and Γ hole and electron pockets lying below and above E_F. For further insight, we use DFT to compute the band structure of free-standing 1UC FeSe via the generalized gradient approximation (GGA) [150] and projector augmented wave (PAW) method as implemented in the Vienna Ab-Initio Simulation Package (`VASP`) [151, 152]. We use a BZ sampling of 9×9×1 and an energy cutoff of 450 eV. We apply Methfessel-Paxton smearing [153] with $\sigma = 0.1$ eV. Figure 4.5(a) shows the calculated bands with structural parameters $a = 3.90$ Å, $h_{\mathrm{Se}} = 1.45$ Å. Due to electron doping, E_F should be adjusted to intersect only the M pockets. Typical band renormalization factors range from 4–5 in 1UC FeSe/SrTiO$_3$ [53], but for the qualitative discussion that follows, we do not rescale the bands.

Experimentally, h_{Se} is unknown. Simulations show that the binding geometry of 1UC FeSe/SrTiO$_3$ varies with TiO$_2$ oxygen deficiency, which creates electropositive sites that distort Se positions [68]. Without microscopic knowledge of the buried interface, we calculate band structures for a range of h_{Se} values and track the energies of the Γ bands [Fig. 4.5(b)]. While all bands shift slightly, the lowest-lying Γ electron pocket in Fig. 4.5(a) undergoes a pronounced monotonic decrease in energy with increasing h_{Se}. Figure 4.5(c) shows the charge density isosurfaces at $\boldsymbol{k} = 0$ and orbital compositions for each band. Only the lowest-lying Γ electron pocket carries significant Se $4p$ character in addition to Fe $3d$ character, so it is most affected by the Fe-Se distances. The charge density plot suggests an antibonding configuration of Fe $3d_{x^2-y^2}$ and Se $4p_z$ orbitals, which explains the increase in pocket energy with greater overlap of Fe and Se states. Our calculation reveals a crucial connection between h_{Se} and empty electronic states.

Previous reports have predicted that Se/Te heights tune the Fe exchange constants in iron chalcogenides and hence the magnetic order [154], which is oddly absent in FeSe [155] and unknown in 1UC FeSe/SrTiO$_3$. Here, we discuss another implication of h_{Se}. As seen in Fig. 4.5(b), the Γ electron and hole pockets cross at large values of h_{Se}. Recently, Wu *et al.*

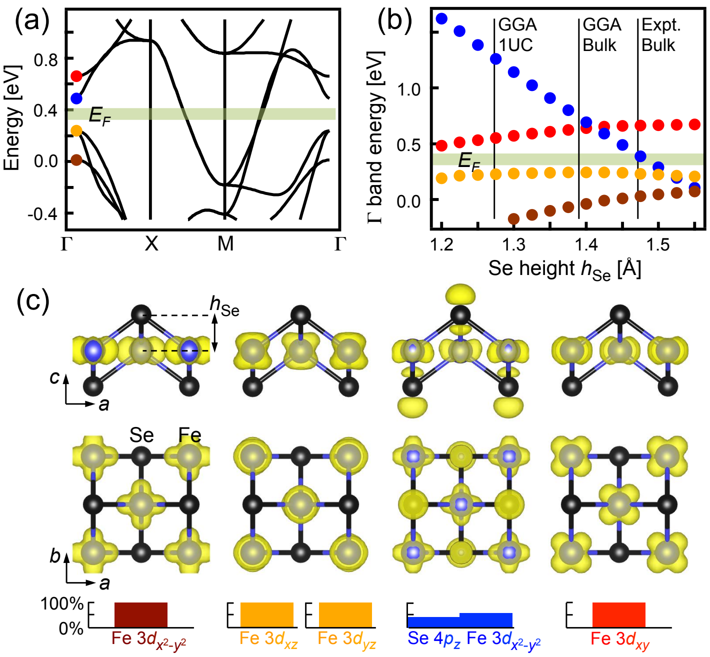

Figure 4.5: (a) Band structure of free-standing single-unit-cell (1UC) FeSe, calculated in the generalized gradient approximation (GGA). Structural parameters: lattice constant $a = 3.90$ Å, Se height $h_{\mathrm{Se}} = 1.45$ Å. (b) Energies of the five Γ bands shown in (a) vs. h_{Se} (the band represented by orange is degenerate). The GGA values of h_{Se} for 1UC FeSe ($a = 3.90$ Å fixed) and bulk FeSe ($a = 3.68$ Å relaxed) are marked, as well as the experimental value for bulk FeSe. The Fermi energy E_F expected from electron doping is marked in (a), (b). (c) Charge density isosurfaces (yellow) at $\boldsymbol{k} = 0$ for the five Γ bands, shown in two perspectives. The histograms depict the orbital compositions.

have proposed that nontrivial $\mathbb{Z}_2$ topology may be realized in 1UC $\mathrm{FeTe}_{1-x}\mathrm{Se}_x$ [156]. In particular, when the gap Δ_n between the Γ electron and hole pockets falls below 80 meV, spin-orbit coupling can invert the bands. We measure Δ_n to be 140 meV from Fig. 4.4(c); thus, 1UC FeSe/SrTiO$_3$ could possibly lie in proximity to a topological phase transition.

4.4 SUMMARY

In summary, we have quantified both the filled and empty state band structure of 1UC FeSe/SrTiO$_3$, and discovered a new Γ-centered pocket emerging around 75 meV above the Fermi level. Our work has several important implications, both for superconductivity and for predicted topological order in FeSe/SrTiO_3. First, the new Γ band will serve as an essential input for revised FRG calculations of the effective low-energy pairing interaction [140]. Second, the modest 140 meV gap we measured between filled and empty Gamma bands gives hope that inversion of these bands may be achievable, and may lead to a predicted topological phase [156]. Finally, our work introduces decay length spectroscopy as a general and complementary technique to QPI imaging, to map the absolute momentum-resolved electronic band structure of filled and empty states using STM. We suggest the use of these techniques in concert to track the Γ pocket energies in future strain engineering experiments with FeSe.

4.5 [SUPPLEMENTAL] ADDITIONAL DETAILS

Figure 4.6 presents the individual energy layers of $|g(\boldsymbol{q}, \omega)|$ that constitute the high-energy portion of Fig. 4.3(j). There is one set of rings at -20 meV that grows with increasing energy (branch 1 in Fig. 4.3(j), red in Fig. 4.6), and another set of higher intensity rings that first appears around 70 meV (branch 3 in Fig. 4.3(j), blue in Fig. 4.6).

In general, near band edge energies, both quasiparticle interference (QPI) and Bragg (lattice) signals may have weight near the reciprocal lattice vectors. Here, we illustrate in Fig. 4.7 that our data exhibit three characteristic distinctions between the Bragg and QPI signals: (1) $\boldsymbol{q}$-space extent, (2) intensity, and (3) dispersion. The Bragg peaks are only a few pixels wide in the raw data; they have large intensity; and they appear in the same $\boldsymbol{q}$-space location across all energies. Furthermore, they collapse onto a single pixel after applying drift-correction according to the *topographic* lattice simultaneously acquired (see Refs. [144, 157] for extensive details). On the other hand, the QPI signals possess a larger radius in $\boldsymbol{q}$-space; they appear at lower intensities; and they disperse/appear/disappear with energy. The QPI signal that first appears around 70 meV, corresponding to the emergence of an empty-state band, cannot be explained by an abnormally large smearing of the Bragg signal.

Figure 4.8 illustrates the azimuthal averaging procedure used to produce Fig. 4.3(j).

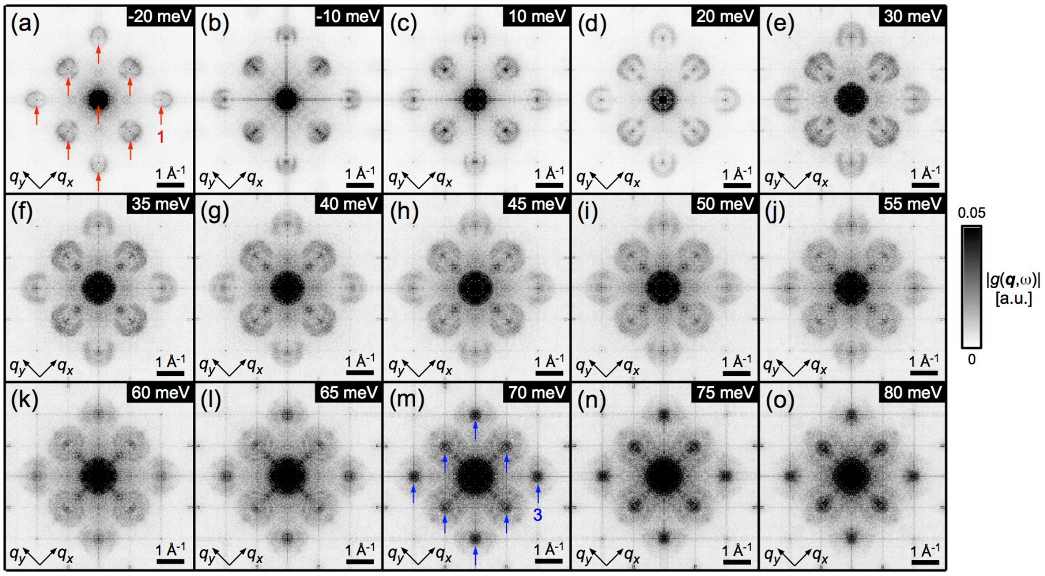

Figure 4.6: Quasiparticle interference (QPI) imaging, momentum-transfer ($\boldsymbol{q}$) space. (a-o) Fourier transform amplitudes $|g(\boldsymbol{q}, \omega)|$ of conductance maps used in Fig. 4.3(j). All images are displayed with the same color scale range. The red and blue arrows denote QPI branches 1 and 3 as discussed earlier.

Within a large radius of $\boldsymbol{G} = (2\pi/a, 0)$ encompassing the QPI signal, every pixel of $|g(\boldsymbol{q}, \omega)|$ is averaged with those having identical distance values q_r to $\boldsymbol{G}$, then displayed as a function of q_r. The resulting plot makes full use of our $\boldsymbol{q}$-space pixel resolution, but the discrete q_r values are spaced unevenly [Figs. 4.8(a), (b)]. We bin each discrete q_r value with its nearest integer pixel value to produce the final plot in Fig. 4.8(c). We additionally note that the first pixel column in Figs. 4.8(b), (c) is nearly saturated because the Bragg peak intensity is so much greater than the QPI signal.

The three bands observed in this work (M electron pocket, Γ hole pocket, Γ electron pocket) are quantified by a combination of three techniques: (1) QPI $|g(q_r, \omega)|$, (2) decay length spectroscopy $d\lambda/d\omega$, and (3) d^2I/dV^2. Figures 4.9(a)-(c) show constant energy cuts of $|g(q_r, \omega)|$, with prominent dispersing peaks due to M electron pocket scattering. These dispersing peak positions are fit to a parabola [Fig. 4.9(d)], which then serves as the guide overlaid in Fig. 4.3(j) and labeled "branch 1". Slight deviations from the parabolic fit are present

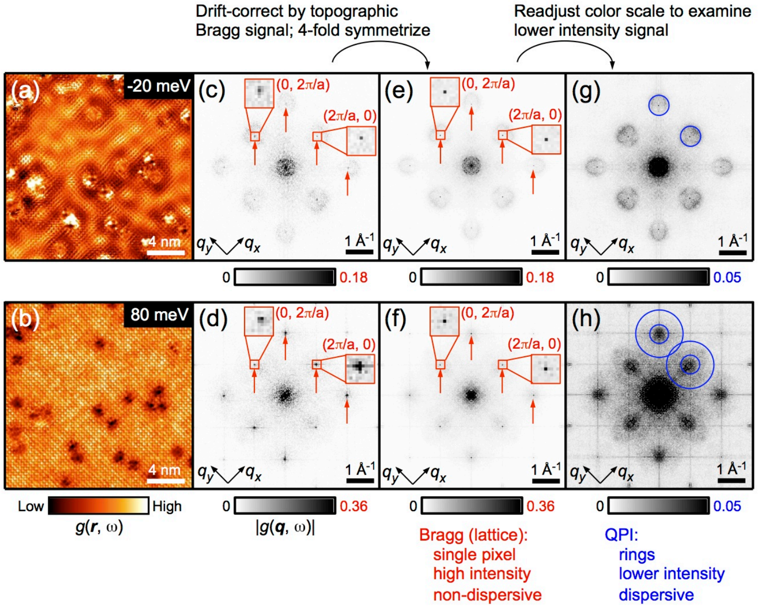

Figure 4.7: Distinct observations of Bragg signals *at* the reciprocal lattice vectors and QPI signals *around* the reciprocal lattice vectors. (a,b) Conductance maps at two energy layers, −20 meV and 80 meV, along with their Fourier transform amplitudes $|g(\boldsymbol{q}, \omega)|$ in (c), (d). (e), (f) After applying a drift-correction algorithm using parameters determined entirely from the simultaneous topographic map, the Bragg peaks appear as a non-dispersive, single-pixel entities. (g), (h) By examining lower intensities of (e), (f), QPI signals manifest as dispersive rings with larger $\boldsymbol{q}$-space radius.

within the superconducting gap energy 2Δ.

QPI branches 2 and 3 are visible in Figs. 4.9(a), (c) as emerging peaks centered about $q_r = 0$ that grow in amplitude and width away from the Fermi energy E_F. The band edge for branch 2 is difficut to fit, along either the energy or q_r axes, because its signal overlaps with that of branch 1. However, its hole-like dispersion is evident when one tracks the tail end of the dispersing peaks (green pixels in Fig. 4.8(c) within $q_r \sim 0.2$–0.3 [$2\pi/\mathrm{a}$]) and observes a change in dispersion direction near −60 meV. (A similar kink in the dispersion is visible at high energies, corresponding to the onset of branch 3). We quantify branch 2 by tunneling decay length and dI/dV measurements. Details are discussed in the main text, but here in Fig. 4.10(c), (d) the numerical derivatives $d\lambda/d\omega$ and d^2I/dV^2 and their peak fits are explicitly shown. We overlay a guide for branch 2 in Fig. 4.3(j) with its band edge informed

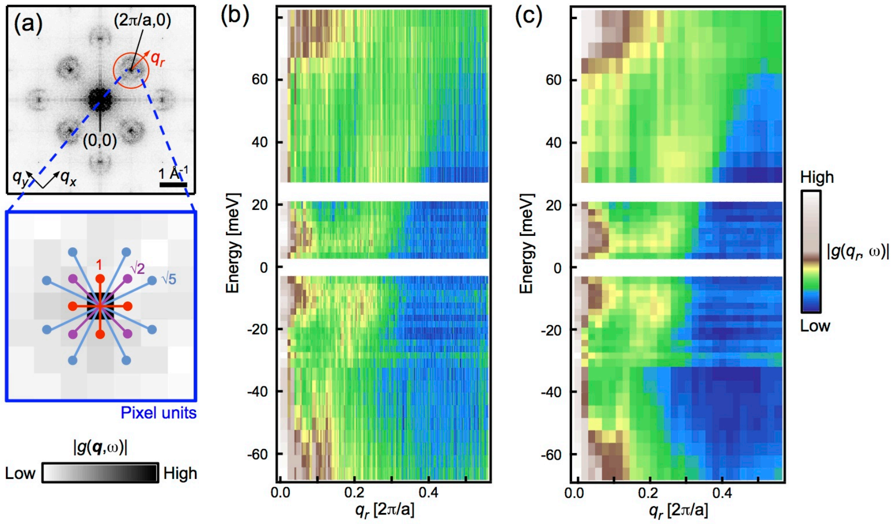

Figure 4.8: Azimuthal averaging procedure used for visualizing QPI dispersion. (a), (b) First, every pixel of $|g(\boldsymbol{q}, \omega)|$ near $\boldsymbol{G} = (2\pi/a, 0)$ is averaged with those having identical distance values q_r to $\boldsymbol{G}$, then displayed as a function of q_r. (c) Second, each discrete q_r value is binned with its nearest integer pixel value to produce the final plot shown in Fig. 4.3(j).

by these two measurements (-59 ± 5 meV and -65 ± 3 meV respectively) and its dispersion informed by angle-resolved photoemission spectroscopy (ARPES) measurements of the same pocket [49].

To capture the band edge of branch 3, we take constant-q_r cuts of $|g(q_r, \omega)|$, and fit the observed peak locations to a parabolic dispersion [Figs. 4.10(a),(b)]. The resulting fit serves as the guide for branch 3 overlaid in Fig. 4.3(j). The position of this line is further confirmed by the positive energy extrema of $d\lambda/d\omega$ and d^2I/dV^2, which yield 78 ± 5 meV and 77 ± 3 meV respectively.

A summary of the band parameters extracted from these quantitative analyses is given in Table 4.1.

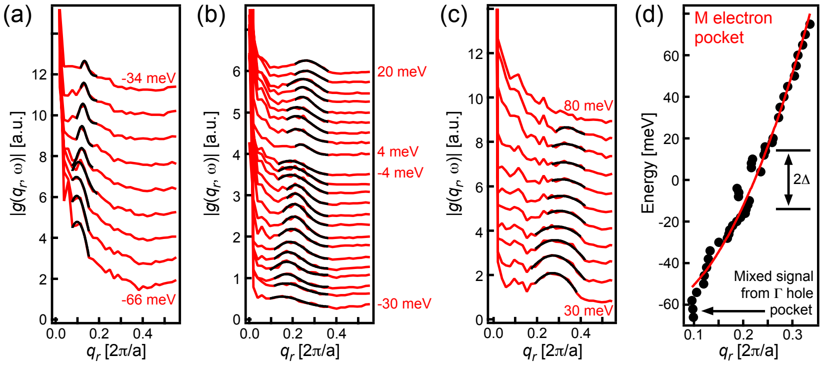

Figure 4.9: (a)-(c) Azimuthally-averaged line cuts of $|g(q_r,\omega)|$, offset in evenly-spaced energies. q_r is measured relative to $\boldsymbol{G} = (2\pi/a, 0)$. Dispersing peaks from M electron pocket scattering (branch 1 in the main text) are fit to Gaussians (black line overlays), and the extracted peak positions are fit to a parabola in (d). The superconducting gap is marked by 2Δ.

Main text figure	SM figure	Method	M electron pocket		Γ hole pocket	Γ electron pocket
			k_F $[\pi/a]$	m^*/m	ε_0 [meV]	ε_0 [meV]
3(j)	4.9, 4.10(a,b)	$\lvert g(q_r,\omega)\rvert$	0.22 ± 0.01	2.0 ± 0.1	(-60)	75 ± 3
4(b)	4.10(c)	$d\lambda/d\omega$	–	–	-59 ± 5	78 ± 5
4(c)	4.10(d)	d^2I/dV^2	–	–	-65 ± 3	77 ± 3

Table 4.1: Summary of band parameters quantified by QPI imaging $|g(q_r,\omega)|$, decay length spectroscopy $d\lambda/d\omega$, and d^2I/dV^2. k_F denotes the Fermi wave vector, m^* is the effective mass, and ε_0 is the band edge.

Finally, we present additional decay length spectroscopy measurements. Figures 4.11(a), (b) compare $\lambda(\omega)$ measurements of single-unit-cell FeSe/SrTiO$_3$ taken with a PtIr tip with two different microscopic terminations. While the absolute values of $\lambda(\omega)$ vary slightly due to differences in tip work function, the steep rises corresponding to the onset of Γ-centered pockets occur at the same energies. Figure 4.11(c) shows a calibration measurement on polycrystalline Au exhibiting a flat $\lambda(\omega)$, consistent with previous measurements on Au(111) [148].

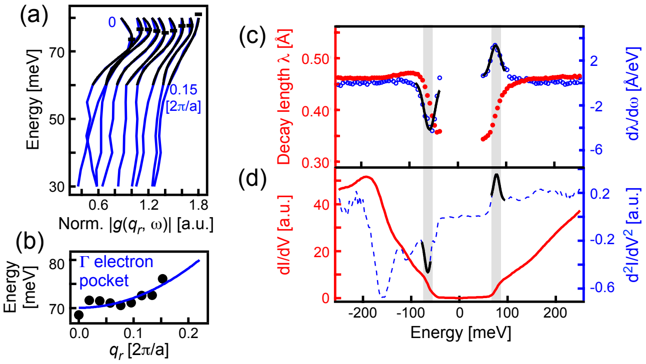

Figure 4.10: (a) Constant-q_r line cuts of $|g(q_r, \omega)|$, offset in evenly-spaced q_r values and normalized by their maximum amplitude for improved visualization. Dispersing peaks from Γ electron pocket scattering [branch 3 of Fig. 4.3(j)] are fit to Gaussians (black line overlays with horizontal bars indicating peak positions), and the resulting peak positions are fit to a parabola in (b). (c) Energy dependent decay length $\lambda(\omega)$ (red circles), repeated from Fig. 4.4(b), along with its numerical derivative (blue circles). (d) dI/dV spectrum (red solid line), repeated from Fig. 4.4(c), along with its numerical derivative (blue dashed lines). Gaussian peak fits for band edge extraction are overlaid (black solid lines), and vertical shaded bars mark their peak positions.

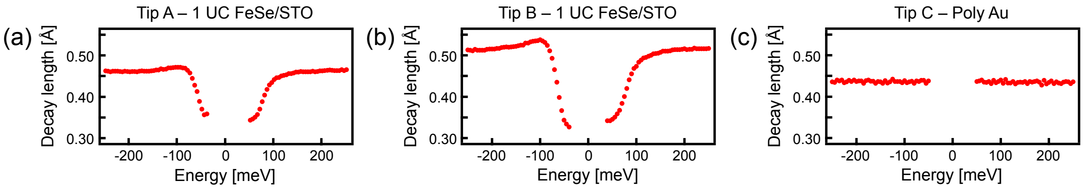

Figure 4.11: (a), (b) Energy dependent decay length $\lambda(\omega)$ of single-unit-cell (1UC) FeSe/SrTiO$_3$, taken with a PtIr tip with two different microscopic terminations (called A and B). (c) $\lambda(\omega)$ acquired on polycrystalline Au.

5

Bounds on Nanoscale Nematicity in Single-Layer FeSe/SrTiO$_3$

We use scanning tunneling microscopy (STM) and quasiparticle interference (QPI) imaging to investigate the low-energy orbital texture of single-layer FeSe/SrTiO$_3$. We develop a T-matrix model of multi-orbital QPI to disentangle scattering intensities from Fe $3d_{xz}$ and $3d_{yz}$ bands, enabling the use of STM as a nanoscale detection tool of nematicity. By sampling multiple spatial regions of a single-layer FeSe/SrTiO$_3$ film, we quantitatively exclude static xz/yz orbital ordering with domain size larger than $\delta r^2 = 20$ nm $\times$ 20 nm, xz/yz Fermi wave vector difference larger than $\delta k = 0.014\ \pi$, and energy splitting larger than $\delta E = 3.5$ meV. The lack of detectable ordering pinned around defects places qualitative constraints on models of fluctuating nematicity.

5.1 INTRODUCTION

Since the 2012 discovery of enhanced high-temperature superconductivity in single-layer FeSe/$SrTiO_3$ [1], the quest to reproduce, understand, and extend this finding remains urgent. Single-layer FeSe weakly coupled to bilayer graphene is non-superconducting down to 2.2 K [44], but when deposited on $SrTiO_3(001)$, exhibits a superconducting transition temperature T_c up to 65 K [50, 51, 52, 59] or 109 K [2]. Efforts to elucidate the microscopic mechanisms behind this transformation have presently led to divergent viewpoints [93, 95]. At the crux of the debate is whether single-layer FeSe/$SrTiO_3$ exemplifies a novel pairing mechanism involving cross-interface phonon coupling, or whether it shares a common electronic mechanism with other iron chalcogenides already seen.

Indications of the first viewpoint were brought forth by angle-resolved photoemission spectroscopy (ARPES) measurements, which revealed that the primary electronic bands possess faint “shake-off” bands offset by 100 meV [52, 53]. The replication of primary band features without momentum offset suggests an electron-boson coupling sharply peaked at $\boldsymbol{q} \sim 0$. The boson was initially hypothesized to be an O phonon mode and subsequently observed on bare $SrTiO_3(001)$ [92]. Model calculations have demonstrated that phonons can enhance spin-fluctuation-mediated pairing in FeSe [140, 52, 127]. Others have argued that phonons alone can account for a significant portion of the high T_c [80, 94].

An alternative but possibly complementary viewpoint is that electron doping underlies the primary enhancement of T_c in single-layer FeSe/$SrTiO_3$. Early experiments observed that as-grown films become superconducting only after a vacuum annealing process [50]. This procedure presumably generates interfacial O vacancies donating electron carriers [68]. More recent experiments showed that multilayer FeSe, which does not exhibit replica bands from coupling to $SrTiO_3$ phonons, can still develop superconductivity (T_c up to 48 K suggested by ARPES) when coated with K atoms [100, 101, 102, 81, 82, 83]. Two observations from these latter experiments are crucial. First, the dome-shaped evolution of T_c with doping refocuses attention on electronic (spin/orbital) mechanisms of pairing [95]. Second, the enhanced T_c emerges from a parent, bulk nematic phase, characterized in multilayer FeSe by a small orthorhombic distortion [103] and a large splitting of the Fe $3d_{xz}$ and $3d_{yz}$ bands [104, 105, 106, 107, 108].

Nematic order, defined more generally as broken rotational symmetry with preserved translational symmetry, is a hallmark of the parent phase of iron-based superconductors. Importantly, both spin and orbital fluctuations that are candidate pairing glues can condense into parent nematic order [158]. Furthermore, $\boldsymbol{q} \sim 0$ nematic fluctuations that extend beyond phase boundaries can enhance T_c [112, 113]. This mechanism operates in any pairing channel, with increased effectiveness in a 2D system [114]. Recent DFT calculations have shown that bulk and single-layer FeSe exhibit a propensity towards shearing, but that strong binding to cubic $\mathrm{SrTiO_3}$ suppresses this lattice instability [80]. It is tempting to ask whether in addition to suppressing nematic order, this binding may push the heterostructure closer to a nematic quantum critical point, with intensified fluctuations.

To investigate the possible role of nematicity, we use scanning tunneling microscopy (STM) and quasiparticle interference (QPI) imaging. By generating scattering through moderate disorder, quasiparticle attributes such as spin/orbital/valley texture, or the superconducting order parameter, are manifested in selection rules that underlie the interference patterns. STM also affords dual real- and momentum-space visualization of electronic states within nanoscale regions. Previous STM works have uncovered $C2$ electronic patterns in parent $\mathrm{Ca(Fe_{1-x}Co_x)_2As_2}$ [159, 160], LaOFeAs [161], NaFeAs [115, 162], and superconducting orthorhombic FeSe [43, 163]. In addition, remnant nematic signatures were detected in the nominally tetragonal phases of NaFeAs [115] and $\mathrm{FeSe_{0.4}Te_{0.6}}$ [116]. These latter observations motivate our present investigation. Can local disorder or anisotropic perturbations pin nanoscale patches of otherwise-fluctuating nematicity in single-layer FeSe/$\mathrm{SrTiO_3}$, signaling proximate nematic quantum criticality? Or is the heterostructure too far from a nematic phase boundary for fluctuations to persist and boost T_c?

This chapter is organized as follows: Section 5.2 presents experimental details, including QPI images acquired on single-layer FeSe/$\mathrm{SrTiO_3}$. In order to extract the low-energy orbital texture and disentangle scattering intensities involving Fe $3d_{xz}$ and $3d_{yz}$ bands, we develop a T-matrix model of multi-orbital QPI, with results shown in Sec. 5.3 and mathematical details given in Supplemental Section 5.6. In Sec. 5.4, we sample multiple spatial regions of our film, and based on our orbital-resolved QPI model, exclude static nematicity in the form of xz/yz orbital ordering. Within domains of size δr^2 = 20 nm × 20 nm, we place quantitative bounds on xz/yz Fermi wave vector difference ($\delta k \leq 0.014\ \pi$) and xz/yz pocket splitting energy ($\delta E \leq 3.5$ meV). The lack of detectable ordering pinned around impurities places qualitative constraints on models of fluctuating nematicity. A discussion and summary of results is given in Sec. 5.5. Additional details on local defect structure and fitting procedures are presented in Supplemental Sections 5.7 and 5.8.

5.2 EXPERIMENT

Films of single-layer FeSe were grown epitaxially on $SrTiO_3(001)$ following procedures outlined in Ref. [96], then imaged in a home-built STM at 4.3 K. Typical superconducting gaps observed at this temperature were ~14 meV [96]. Figs. 5.1(a)-(c) present three atomically resolved topographies of the same area, acquired with different energy set points. Each bright spot corresponds to a surface Se atom; there are no in-plane defects in this region. Our images reveal that even pristine single-layer $FeSe/SrTiO_3$ displays appreciable electronic inhomogeneity, in strong contrast to multilayer films grown on bilayer graphene [44, 43]. The electronic inhomogeneity in $FeSe/SrTiO_3$ underscores the need for nanoscale measurements of electronic structure.

To image QPI and extract local orbital information, we acquired conductance maps $g(\boldsymbol{r}, \omega) = dI/dV(\boldsymbol{r}, eV)$ over regions of the film with in-plane defects [exemplified in Figs. 5.1(d)-(f)]. A brief commentary on the defect structures is given in Supplemental Section 5.7. Figure 5.2(a) shows the Fourier transform amplitude $|g(\boldsymbol{q}, \omega)|$ of a map with ω = 20 meV. Ring-shaped intensites appear around $\boldsymbol{q}$ = 0, ($\pm\pi$, $\pm\pi$), (0, $\pm 2\pi$), and ($\pm 2\pi$, 0) due to scattering of Fermi electron pocket states. Previous works utilized ring *size* dispersion to map filled-

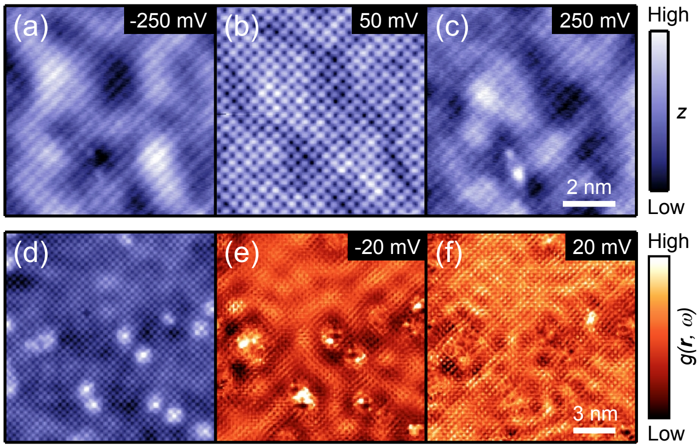

Figure 5.1: (a)-(c) Pristine region of single-layer FeSe/SrTiO$_3$. Topographies of the same area are acquired with three set points, revealing background electronic disorder: (a) -250 mV, 1.25 nA, (b) 50 mV, 250 pA, (c) 250 mV, 1 nA. (d)-(f) Defect region of single-layer FeSe/SrTiO$_3$. Topography and differential tunneling conductance maps of the same area, revealing quasiparticle interference. (d) 100 mV, 5 pA, (e) -20 mV, 200 pA, bias oscillation $V_{\mathrm{rms}} = 1.4$ mV, (f) 20 mV, 200 pA, $V_{\mathrm{rms}} = 1.4$ mV.

and empty-state band structure [96], or energy- and magnetic field-dependent ring *intensities* to infer pairing symmetry from coherence factor arguments [76]. Here, we will examine ring *anisotropy* associated with the high-$\boldsymbol{q}$ scattering channels [red and blue boxes in Fig. 5.2(a)]. We will demonstrate that (1) although all the QPI rings are derived from scattering within and between the same electron pockets, the high-$\boldsymbol{q}$ scattering channels have more stringent selection rules and hence a cleaner orbital interpretation; (2) the high-$\boldsymbol{q}$ scattering channels can be utilized to search for signatures of xz/yz orbital ordering.

Directly from the data in Fig. 5.2(a), we observe an unusual relationship between the anisotropic rings around $\boldsymbol{q} = (0, 2\pi)$ and $(2\pi, 0)$. In a single layer of FeSe, the Fe atoms are arranged in a planar square lattice, from which we define a 1-Fe unit cell (UC) [Fig. 5.2(b)] and crystal momentum transfer $\boldsymbol{q}$ [Fig. 5.2(a)]. We emphasize the distinction between the $\boldsymbol{k}$-space Brillouin zone and the $\boldsymbol{q}$-space crystal momentum transfer that is directly detected by STM imaging of QPI patterns. Including the Se atoms staggered above and below the Fe plane, the primitive UC becomes doubled. We might expect the QPI rings around $(0, 2\pi)$,

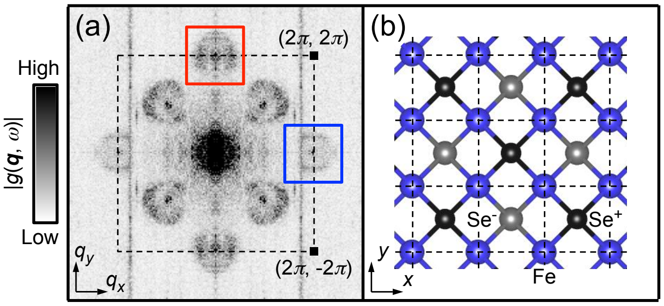

Figure 5.2: (a) Fourier transform amplitude $|g(\boldsymbol{q}, \omega)|$ of a 20 nm × 20 nm conductance map. Set point: 20 mV, 200 pA; bias oscillation $V_{\text{rms}} = 1.4$ mV. Drift-correction [144] and mirror symmetrization along the Fe-Fe axes are applied for increased signal. Note that fourfold rotational symmetrization has not been applied. (b) Crystal structure of single-layer FeSe. The black/gray Se atoms labeled $+/-$ lie above/below the plane. Dashed lines in (a) and (b) refer to the 1-Fe UC.

$(2\pi, 0)$ to be identical translations by the 2-Fe UC reciprocal lattice vector $2\boldsymbol{G} = (-2\pi, 2\pi)$. Instead, they appear to be inequivalent and related by 90° rotation. The cause and implications of this observation will be discussed in the following section.

5.3 Multi-orbital Quasiparticle Interference

We develop a model to map experimental $|g(\boldsymbol{q}, \omega)|$ patterns to the orbital characters of the scattered quasiparticles, similar in concept to Ref. [146]. In this section, we present an intuitive picture, followed by T-matrix simulations with and without xz/yz orbital ordering. Model details are given in Supplemental Section 5.6.

Since the Fermi surface (FS) of single-layer FeSe is derived from Fe $3d$ orbitals, a natural starting point is to consider a low-energy model of a square lattice of Fe atoms. Figure 5.3(a) depicts a schematic FS, consisting of single elliptical electron pockets around $\boldsymbol{k} = (0, \pi)$, $(\pi, 0)$. The hole pockets which typically appear around $(0, 0)$ in other iron-based superconductors are sunken below the Fermi energy due to electron doping from $SrTiO_3$ [49, 50, 51, 52].

Although the Se atoms positioned between next-nearest neighbor Fe atoms contribute little spectral weight to the FS, their presence alters crystal symmetry and cannot be ignored. Their staggered arrangement doubles the primitive UC, folding the electron pockets around

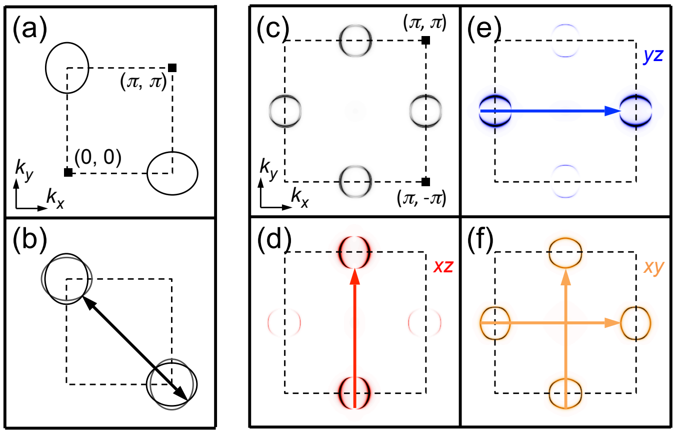

Figure 5.3: (a) Schematic Fermi surface (FS) of single-layer FeSe/SrTiO$_3$, derived from Fe 3d orbitals. The FS is composed of single elliptical electron pockets around $\boldsymbol{k}$ = (0, π), (π, 0). (b) Upon introducing the potential of staggered Se atoms, the electron pockets would naively fold onto each other (double-headed arrow); however, due to incomplete folding, they remain orbitally distinct. (c) Simulated FS of single-layer FeSe/SrTiO$_3$ and (d)-(f) its dominant orbital contributions (xz, yz, xy). The arrows mark the expected elastic scattering wave vectors which may contribute to the $\boldsymbol{q}$ = (0, 2π) and (2π, 0) scattering channels of interest.

(0, π), (π, 0) on top of each other [Fig. 5.3(b)]. However, an underappreciated fact is that the pockets do not become identical replicas. Fe 3d orbitals that are even with respect to z-reflection ($x^2{-}y^2$, xy, $3z^2{-}r^2$) cannot distinguish whether Se atoms lie above/below the plane; only odd orbitals (xz, yz) feel an effective potential of doubled periodicity [164]. In terms of tight-binding (TB) models, the only hopping terms that get folded in $\boldsymbol{k}$-space are those involving a product of odd and even orbitals [122, 165, 166].

To illustrate, we simulate the FS for single-layer FeSe/SrTiO$_3$ and show the dominant orbital contributions in Figs. 5.3(c)-5.3(f). Due to incomplete folding, the orbital textures of the pockets around (0, π) and (π, 0) remain distinct and separately dominated by xz/xy and yz/xy quasiparticles respectively.

In the presence of disorder, elastic scattering channels should peak around wave vectors $\boldsymbol{q}$ connecting FS segments with large density of states. Considering only the pockets shown in Figs. 5.3(d)-5.3(f), we anticipate the xz quasiparticles to scatter predominantly around

$\boldsymbol{q} = (0,\, 2\pi)$, the yz quasiparticles to scatter predominantly around $\boldsymbol{q} = (2\pi,\, 0)$, and the xy quasiparticles to scatter around both wave vectors. Figures 5.4(a)-5.4(c) show T-matrix calculations of the orbital-resolved, density-of-states (DOS) modulations $|\rho_{mm}(\boldsymbol{q}, \omega = 0)|$. The index m denotes the Fe $3d$ orbitals, and we assume a localized, s-wave scatterer in our simulations. Comparing simulation results to experimental QPI patterns at low energies [Fig. 5.2(a)], we observe that the elliptical rings around $\boldsymbol{q} = (0,\, 2\pi)$, $(2\pi,\, 0)$ resemble the xz- and yz-projected DOS modulations respectively. Signatures of the xy-projected DOS modulations, which involve oppositely oriented elliptical rings [Fig. 5.4(c)], appear to be suppressed in Fig. 5.2(a). Due to the in-plane orientation of xy orbitals, their wave function amplitudes at the STM tip height are likely smaller.

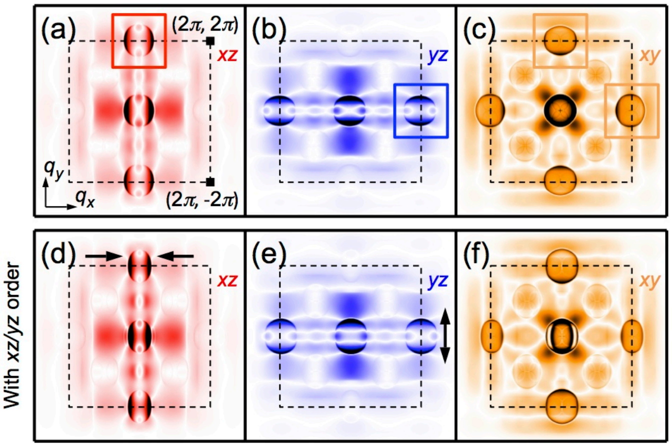

Figure 5.4: Quasiparticle interference simulations of single-layer FeSe/SrTiO$_3$. (a)-(c) Orbital-resolved, density-of-states modulations $|\rho_{mm}(\boldsymbol{q}, \omega = 0)|$ in the presence of a localized, s-wave scatterer. The boxes mark signals around $\boldsymbol{q} = (0,\, 2\pi)$, $(2\pi,\, 0)$ that are the focus of this paper. (d)-(f) $|\rho_{mm}(\boldsymbol{q}, \omega = 0)|$ with the inclusion of xz/yz orbital order. The arrows mark the resulting distortion of the rings.

The disentangling of xz/yz-derived QPI signals around $\boldsymbol{q} = (0,\, 2\pi)$, $(2\pi,\, 0)$ and the suppression of xy signals yield a straightforward prescription to detect nanoscale xz/yz orbital ordering. (In contrast, the QPI signal around $\boldsymbol{q} = (0,\, 0)$ would involve both xz and yz orbital contributions). Such orbital ordering would lead to a population imbalance of xz/yz

carriers, implying unequal Fermi pocket sizes and resulting anisotropy between the (0, 2π), (2π, 0) scattering channels. To simulate this effect, we add on-site ferro-orbital ordering to our model. Figures 5.4(d)-5.4(f) show simulation results, which demonstrate squishing of the xz ring signal around (0, 2π) and the rounding of the yz ring signal around (2π, 0). We show the xy-projected DOS modulations for completeness, although its associated tunneling amplitude is suppressed. Recent studies have also proposed orbital ordering to be bond-centered and d-wave [107, 167], but these complexities produce the same qualitative effect for QPI involving the electron pockets only.

5.4 Experimental Bounds on Nanoscale Orbital Ordering

We carried out experimental tests for xz/yz orbital ordering as follows. To account for local inhomogeneity, we sampled QPI over four distinct domains of size $\delta r^2 = 20$ nm × 20 nm (called Areas A through D in Fig. 5.5). Each domain was imaged following a separate STM tip-sample approach, and was likely separated from other domains by distances larger than our scan frame width, $\delta L = 1.5$ μm. To rule out tip anisotropy artifacts, the data from each domain were acquired with a different microscopic tip termination, modified by field emission on polycrystalline Au. Over every domain, conductance maps were acquired at low energies (± 10 meV) in order to compare scattering from xz and yz Fermi pockets.

Figures 5.5(a) and 5.5(b) show QPI images acquired over area A, cropped around $\boldsymbol{q}$ = (0, 2π) and (2π, 0). We applied Gaussian smoothing with width $\sigma = \delta q$, where $\delta q = 0.028\ \pi$ is the inherent resolution for momentum defined within a finite 20 nm × 20 nm area. To compare the xz- and yz-derived QPI rings, we took line cuts along their minor axes (arrows in Figs. 5.5(a) and 5.5(b)), where the signal intensity is the strongest. Each line cut was averaged over a width of 10 pixels. The results for the four domains and two energies are shown in Figs. 5.5(c) and 5.5(d). We determined peak locations from Gaussian fits (solid lines). The horizontal bars denote extracted peak locations with error $\pm\delta q$. The addition of a linear background is found to shift the fitted Gaussian peak locations, by an amount smaller than

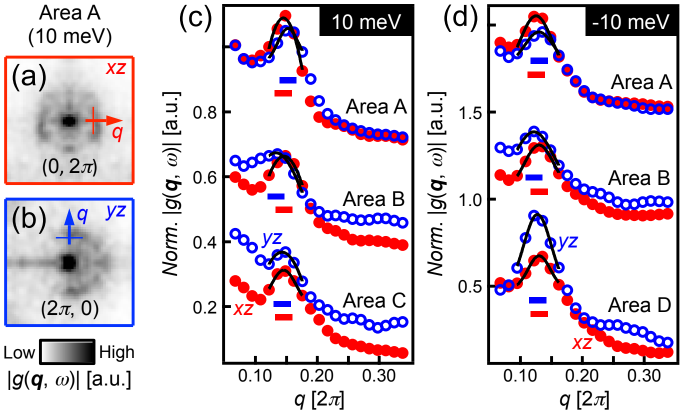

Figure 5.5: Nanoscale wave vector analysis of orbital ordering. (a), (b) Cropped quasiparticle interference images $|g(\boldsymbol{q}, \omega)|$ around (0, 2π) and (2π, 0), with arrows indicating line cuts used to compare xz/yz Fermi pocket sizes (perpendicular bars represent averaging width). (c), (d) Line cuts from conductance maps acquired over four distinct domains ($\delta r^2 = 20$ nm $\times$ 20 nm), labeled A through D, and two energies, ± 10 meV. The horizontal bars mark the peak locations determined from Gaussian fits (solid lines), with inherent resolution $\delta q = 0.028\ \pi$. For visualization, the line cuts are normalized by the Bragg peak amplitude and vertically offset.

δq (Supplemental Section 5.8). In all four areas, we observe no significant deviations between the xz- and yz-derived QPI wave vectors. We therefore exclude orbital ordering with domain size larger than $\delta r^2 = 20$ nm $\times$ 20 nm and xz/yz FS wave vector difference larger than $\delta k = \delta q/2 = 0.014\ \pi$ (the factor of two arises when changing between $\boldsymbol{q}$ space and $\boldsymbol{k}$ space).

We also determine an energy bound on xz/yz orbital ordering. Figures 5.6(a) and 5.6(b) show a simulated splitting of the xz/yz bands for reference, and Figs. 5.6(c) and 5.6(d) show the corresponding QPI dispersions measured over Area B. The dispersing peaks locations are extracted from Gaussian fits, shown in Fig. 5.6(e), and are identical within $\pm\delta q$ over the given energy range [-30 meV, 20 meV]. Due to the overlap with a sunken, zone center hole pocket [49, 96], the lower edges of the Fermi pockets are difficult to detect. Instead, we fit the dispersing peak locations to parabolas, and find their respective band edges to be -51.5 ± 3.5 meV and -49.6 ± 3.0 meV. We again bound orbital ordering with $2\Delta_{xz/yz} \leq \delta E = 3.5$ meV.

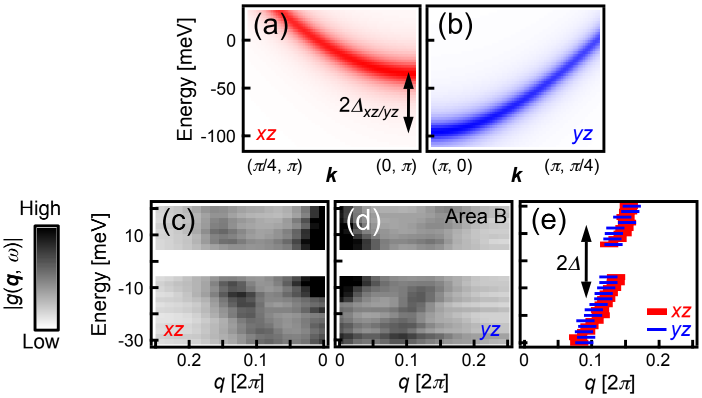

Figure 5.6: Nanoscale dispersion analysis of orbital ordering. (a), (b) Simulated pockets with xz/yz orbital ordering, revealing a split in the band edges of magnitude $2\Delta_{xz/yz} = 60$ meV. (c), (d) Experimental intensity plots of quasiparticle interference images $|g(\boldsymbol{q}, \omega)|$ acquired over Area B, cut along the arrows in Figs. 5.5(a) and 5.5(b). (e) Plot of dispersing peaks positions extracted from Gaussian fits. The width of the horizontal bars is $\pm\delta q = \pm 0.028\ \pi$. The superconducting gap magnitude is marked by 2Δ.

5.5 Discussion and Summary

We return to the central debate, whether single-layer FeSe/SrTiO$_3$ exemplifies a novel interface-phonon pairing mechanism, or whether it can be explained by an electronic mechanism common to other iron chalcogenides. Recent experiments demonstrating sizeable T_c in electron-doped multilayer FeSe [100, 101, 102, 81, 82, 83] suggest an electronic pairing mechanism in other iron chalcogenides lacking hole Fermi surfaces, distinct from a SrTiO$_3$ phonon mode. One possibility involves $\boldsymbol{q} \sim 0$ nematic fluctuations extending from the parent ordered phase. Theories have shown that such fluctuations can boost T_c effectively in any pairing channel, on both the ordered and disordered sides of the phase transition [112, 113, 114].

Moving from multilayer to single-layer FeSe/SrTiO$_3$, we face two scenarios. One scenario is that single-layer FeSe/SrTiO$_3$ remains close to a nematic phase boundary. Here, ordering is absent, but intense nematic fluctuations may be pinned by impurities. Another scenario is that single-layer FeSe/SrTiO$_3$ lies sufficiently far away from a nematic phase boundary, such that $C2$ electronic signatures are not produced even upon local perturbation. The quantitative bounds on static xz/yz orbital ordering derived from our QPI measurements favor the latter scenario. In turn, this statement would suggest that single-layer FeSe/SrTiO$_3$ is not the same as electron-doped multilayer FeSe, in which nematic fluctuations may be operative [102]. The addition of the SrTiO$_3$ substrate introduces novel effects beyond electron doping, such as possible interface phonons, that push the two systems apart in phase space.

To summarize, we have utilized STM and QPI imaging to demonstrate that the pronounced nematic order present in multilayer FeSe is suppressed in single-layer FeSe/SrTiO$_3$. More importantly, nanoscale nematic ordering is not recovered upon perturbation by anistropic defects. We arrived at our conclusions by comparing high-$\boldsymbol{q}$ scattering channels around (0, 2π) and (2π, 0), which we showed by T-matrix simulations to be separately dominated by xz and yz quasiparticles. Our work places quantitative bounds on static xz/yz orbital ordering in single-layer FeSe/SrTiO$_3$, and qualitative constraints on models of T_c enhancement by nematic fluctuations.

5.6 [Supplemental] Model of Multi-orbital Quasiparticle Interference

Model Hamiltonian: We begin with a TB model for single-layer FeSe where the low-energy bands are projected onto the five 3d orbitals of an Fe atom:

$$\tilde{H}^0 = \sum_{\boldsymbol{ij}} \sum_{mn} \tilde{t}_{mn}(|i_x - j_x|, |i_y - j_y|)\tilde{c}^\dagger_m(\boldsymbol{i})\tilde{c}_n(\boldsymbol{j}). \tag{5.1}$$

Here, $\boldsymbol{i}, \boldsymbol{j}$ index the Fe lattice sites and m, n index the five orbitals. The tilde symbol indicates that a momentum shift $\boldsymbol{Q} = (\pi, \pi)$ has been applied to the even orbitals in order to downfold the UC from two Fe atoms to one [168, 169, 165, 166]. The corresponding bare Green's function is given by

$$\tilde{\boldsymbol{G}}^0(\tilde{\boldsymbol{k}}, \omega) = \left[(\omega + i\delta)\boldsymbol{I}_{5\times5} - \tilde{\boldsymbol{H}}^0(\tilde{\boldsymbol{k}})\right]^{-1}, \tag{5.2}$$

where the bolded capital symbols are matrices and δ is a broadening (= 5 meV for all simulations).

We adapt hopping parameters $\tilde{t}_{mn}$ computed in Ref. [170], then apply rescaling to qualitatively capture the low-energy spectrum of single-layer FeSe/SrTiO$_3$ [96]. The hopping terms are given in Table 5.1, and the resulting band structure is shown in Fig. 5.7. The electron pocket around $\tilde{\boldsymbol{k}} = (0, \pi)$ remains attached to a hole pocket, but this does not affect our simulation results closer to the Fermi level. The positions of the Γ pockets above and below the Fermi energy also do not affect our simulations.

t^{mn}	0	$\hat{x}$	$\hat{y}$	$\hat{x}+\hat{y}$	$2\hat{x}$	$2\hat{x}+\hat{y}$	$\hat{x}+2\hat{y}$	$2\hat{x}+2\hat{y}$
$mn = 11$	-0.0192	−0.0538	−0.1538	0.0904	0.0077	−0.0135	0.0019	0.0135
$mn = 33$	−0.1538	0.1051		−0.0404	−0.0077			
$mn = 44$	0.0462	0.0885		0.0577	−0.0115	−0.0115		−0.0115
$mn = 55$	−0.1504	−0.0385			−0.0154	0.0077		−0.0038
$mn = 12$				0.0192		−0.0058		0.0135
$mn = 13$		−0.1362		0.0381		0.0081		
$mn = 14$		0.1304		0.0054		0.0108		
$mn = 15$		−0.0762		−0.0327				−0.0054
$mn = 34$						−0.0038		
$mn = 35$		−0.1154				−0.0077		
$mn = 45$				−0.0577				0.0038

Table 5.1: Rescaled hopping parameters for tight-binding model adapted from Ref. [170]. Here, m=1 is xz, m=2 is yz, m=3 is x^2–y^2, m=4 is xy, m=5 is $3z^2$–r^2.

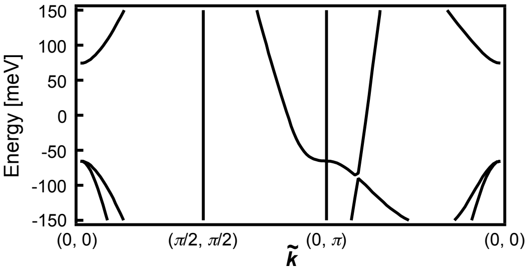

Figure 5.7: Band structure of single-layer FeSe/SrTiO$_3$ in the 1-Fe Brillouin zone. The tilde symbol indicates that a momentum shift $\boldsymbol{Q} = (\pi, \pi)$ has been applied to the even orbitals to downfold the unit cell from two Fe atoms to one. Adapted from Ref. [170], with rescaled hopping parameters to match the pocket edges measured in Ref. [96].

Fermi surface simulations: Computing the FS of single-layer FeSe/SrTiO$_3$ [Figs. 5.3(c)-5.3(f)] from our TB model requires that we restore the original crystal symmetry (with a 2-Fe UC) induced by staggered Se atoms. To do so, we transform the lattice operators with a site-dependent sign factor [165]:

$$c_m^\dagger(\boldsymbol{i}) = (-p_m)^{-i_x - i_y}\tilde{c}_m^\dagger(\boldsymbol{i}). \tag{5.3}$$

Here, $p_m = \pm 1$ for orbitals that are even/odd with respect to z-reflection. This transformation is equivalent to undoing the downfolding operation applied in Eq. 5.1 and shifting the even orbitals by $-\boldsymbol{Q}$ in momentum space:

$$c_m^\dagger(\boldsymbol{k}) = \begin{cases} \tilde{c}_m^\dagger(\boldsymbol{k}), & p_m = -1, \\ \tilde{c}_m^\dagger(\boldsymbol{k_Q}), & p_m = +1, \end{cases} \tag{5.4}$$

where $\boldsymbol{k_Q} = \boldsymbol{k} - \boldsymbol{Q}$. The orbital components of the FS are given by

$$A_{mm}^0(\boldsymbol{k}, \omega = 0) = \begin{cases} \tilde{A}_{mm}^0(\boldsymbol{k}, 0), & p_m = -1, \\ \tilde{A}_{mm}^0(\boldsymbol{k_Q}, 0), & p_m = +1, \end{cases} \tag{5.5}$$

where $\tilde{A}_{mm}^0(\tilde{\boldsymbol{k}}, \omega) = -\mathrm{Im}\, \tilde{G}_{mm}^0(\tilde{\boldsymbol{k}}, \omega)/\pi$. Further insights on (1) the connection between Eq. 5.5 and ARPES-measured band structures, (2) common misconceptions of whether spectroscopic probes measure quasiparticles closer to the 1-Fe or 2-Fe Brillouin zone description, and (3) proper folding of the superconducting pairing structure, are given in Refs. [122, 165, 166].

Quasiparticle intereference simulations: To generate QPI, we introduce a localized, s-wave scatterer at $\boldsymbol{i} = (0, 0)$ of uniform strength $V = 1$ eV in all orbital channels. The resulting impurity Green's function is given by

$$\tilde{\boldsymbol{G}}(\tilde{\boldsymbol{k}}, \tilde{\boldsymbol{k}}', \omega) = \tilde{\boldsymbol{G}}^0(\tilde{\boldsymbol{k}}, \omega)\boldsymbol{T}(\omega)\tilde{\boldsymbol{G}}^0(\tilde{\boldsymbol{k}}', \omega), \tag{5.6}$$

for $\tilde{\boldsymbol{k}} \neq \tilde{\boldsymbol{k}}'$, and the T-matrix is momentum-independent:

$$\boldsymbol{T}(\omega) = \left[\boldsymbol{I}_{5\times 5} - V \int \frac{d^2\tilde{k}}{(2\pi)^2} \tilde{\boldsymbol{G}}^0(\tilde{\boldsymbol{k}}, \omega)\right]^{-1} V. \tag{5.7}$$

Since STM measures local density of states in real space, we additionally transform lattice operators $\tilde{c}_m^\dagger(\boldsymbol{i})$ into continuum operators $\psi_m^\dagger(\boldsymbol{r})$:

$$\psi_m^\dagger(\boldsymbol{r}) = \sum_{\boldsymbol{i}} (-p_m)^{-i_x - i_y} \phi_m^*(\boldsymbol{r} - \boldsymbol{i}) \tilde{c}_m^\dagger(\boldsymbol{i}). \tag{5.8}$$

The first factor on the right recovers the proper crystal symmetry (2-Fe UC) due to staggered Se atoms [Eq. 5.3]. The second factor on the right, ϕ_m, is the Wannier function associated with orbital m at site $\boldsymbol{i}$. This factor captures nonlocal tunneling contributions [171]. For simplicity, we approximate the Wannier functions at the STM tip height with a square cutoff in momentum space: $\phi_m(\boldsymbol{k}) = 1$ for k_x, $k_y \in$ [-1.5π, 1.5π], and $\phi_m(\boldsymbol{k}) = 0$ otherwise. In real space, this corresponds to a characteristic tunneling width of 0.67 ($a_{\text{Fe-Fe}}$), which is neeeded to reproduce experimental QPI patterns. Figure 5.8 illustrates qualitative differences between simulations with (continuum model) and without (lattice model) non-local tunneling.

From Eq. 5.8, we obtain the continuum impurity Green's function:

$$\mathcal{G}_{mm}(\boldsymbol{k}, \boldsymbol{k'}, \omega) = \begin{cases} \tilde{G}_{mm}(\boldsymbol{k}, \boldsymbol{k'}, \omega)\phi_m^*(\boldsymbol{k})\phi_m(\boldsymbol{k'}), & p_m = -1, \\ \tilde{G}_{mm}(\boldsymbol{k_Q}, \boldsymbol{k'_Q}, \omega)\phi_m^*(\boldsymbol{k})\phi_m(\boldsymbol{k'}), & p_m = +1. \end{cases} \tag{5.9}$$

Only diagonal elements are shown for brevity. Finally, the orbital projections of the DOS modulations are given by

$$\rho_{mm}(\boldsymbol{q}, \omega) = \frac{i}{2\pi} \int \frac{d^2k}{(2\pi)^2} \left[\mathcal{G}_{mm}(\boldsymbol{k}, \boldsymbol{k} + \boldsymbol{q}, \omega) - \mathcal{G}_{mm}^*(\boldsymbol{k}, \boldsymbol{k} - \boldsymbol{q}, \omega)\right]. \tag{5.10}$$

Figs. 5.4(a)-(c) show plots of $|\rho_{mm}(\boldsymbol{q}, 0)|$ for the xz, yz, and xy orbitals.

Orbital ordering: To simulate on-site, ferro-orbital ordering, we include the following

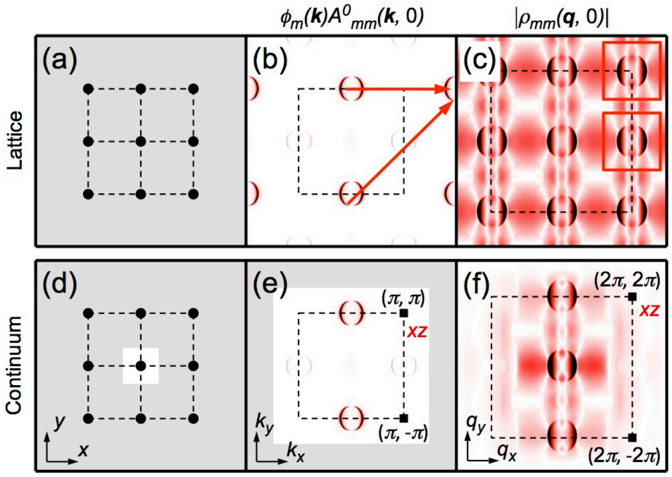

Figure 5.8: (a) Lattice model, in which the Green's function has nonzero weight restricted to discrete lattice points; i.e., the Wannier functions are given by $\phi(\boldsymbol{r} - \boldsymbol{i}) = \delta(\boldsymbol{r} - \boldsymbol{i})$. (b) In momentum space, $\phi_m(\boldsymbol{k}) = 1$, such that there is no cutoff for states involved in scattering. Shown here is $\phi_m(\boldsymbol{k})A^0_{mm}(\boldsymbol{k}, \omega = 0)$ for the xz orbital. (c) Consequently, additional ring intensities arise in $|\rho_{mm}(\boldsymbol{q}, 0)|$ around $\boldsymbol{q} = (2\pi, 0), (2\pi, 2\pi)$ (arrows in (b), boxes in (c)) that are not observed experimentally. (d) Continuum model, which incorporates nonlocal effects due to a finite Wannier function width (white square). (e) We model the experimental data with Wannier functions of the form $\phi_m(\boldsymbol{k}) = 1$ for k_x, $k_y \in$ [-1.5π, 1.5π], and $\phi_m(\boldsymbol{k}) = 0$ otherwise (white square). (f) As a result, there are fewer scattering channels.

term [172] in our TB Hamiltonian [Eq. 5.1]:

$$\tilde{H}^0_{xz/yz} = \Delta_{xz/yz} \sum_{\boldsymbol{i}} \left[\tilde{c}^\dagger_{xz}(\boldsymbol{i})\tilde{c}_{xz}(\boldsymbol{i}) - \tilde{c}^\dagger_{yz}(\boldsymbol{i})\tilde{c}_{yz}(\boldsymbol{i})\right]. \tag{5.11}$$

A value of $\Delta_{xz/yz} = 30$ meV was used for Figs. 5.4(d)-(f) and 5.6(a)-(b).

Superconductivity: The inclusion of superconductivity does not change the QPI orbital texture. Following Ref. [123], we introduce superconductivity in band space, but compute scattering in orbital space. From the normal-state TB Hamiltonian [Eq. 5.1], we define bands $\tilde{\boldsymbol{\epsilon}}(\tilde{\boldsymbol{k}}) = \tilde{\boldsymbol{U}}(\tilde{\boldsymbol{k}})\tilde{\boldsymbol{H}}^0(\tilde{\boldsymbol{k}})\tilde{\boldsymbol{U}}^\dagger(\tilde{\boldsymbol{k}})$, where $\tilde{\boldsymbol{U}}(\tilde{\boldsymbol{k}})$ represents a unitary transformation. The Green's function in the superconducting state is then given by

$$\tilde{\boldsymbol{G}}^0_{\text{sc}}(\tilde{\boldsymbol{k}}, \omega) = \left[(\omega + i\delta)\boldsymbol{I}_{10\times 10} - \tilde{\boldsymbol{H}}^0_{\text{sc}}(\tilde{\boldsymbol{k}})\right]^{-1}, \tag{5.12}$$

where $\tilde{\boldsymbol{H}}^0_{\mathrm{sc}}(\tilde{\boldsymbol{k}})$ has the following form in Nambu representation:

$$\tilde{\boldsymbol{H}}^0_{\mathrm{sc}}(\tilde{\boldsymbol{k}}) = \begin{pmatrix} \tilde{\boldsymbol{U}}^\dagger(\tilde{\boldsymbol{k}})\tilde{\boldsymbol{\epsilon}}(\tilde{\boldsymbol{k}})\tilde{\boldsymbol{U}}(\tilde{\boldsymbol{k}}) & \tilde{\boldsymbol{U}}^\dagger(\tilde{\boldsymbol{k}})\boldsymbol{\Delta}(\tilde{\boldsymbol{k}})\tilde{\boldsymbol{U}}^*(-\tilde{\boldsymbol{k}}) \\ \tilde{\boldsymbol{U}}^T(-\tilde{\boldsymbol{k}})\boldsymbol{\Delta}^*(\tilde{\boldsymbol{k}})\tilde{\boldsymbol{U}}(\tilde{\boldsymbol{k}}) & -\tilde{\boldsymbol{U}}^T(-\tilde{\boldsymbol{k}})\tilde{\boldsymbol{\epsilon}}(-\tilde{\boldsymbol{k}})\tilde{\boldsymbol{U}}^*(-\tilde{\boldsymbol{k}}) \end{pmatrix}. \tag{5.13}$$

We model isotropic gaps in band space: $\boldsymbol{\Delta}(\tilde{\boldsymbol{k}}) = \Delta\boldsymbol{I}_{5\times5}$, with $\Delta = 14$ meV based on our dI/dV measurements. (Recent ARPES measurements have detected small gap anisotropy [79]). We also take the impurity potential of a localized, non-magnetic, s-wave scatterer:

$$\boldsymbol{V} = \begin{pmatrix} V\boldsymbol{I}_{5\times5} & 0 \\ 0 & -V\boldsymbol{I}_{5\times5} \end{pmatrix}. \tag{5.14}$$

Figure 5.9 shows QPI simulations with the inclusion of superconductivity, at energy $\omega =$ 10 meV. There is little difference compared with the normal-state calculations, without or with xz/yz orbital ordering.

Anisotropic scatterer: In an angular momentum expansion of the T-matrix, the leading component should be s-wave; i.e., intraorbital scattering, with $V_{mn} = V_{mm}\delta_{mn}$, should dominate. V_{mm} can in general vary with orbital, but this simply modifies the relative weights of the orbital-resolved DOS modulations. In Fig. 5.10, we illustrate this effect in the case of a $C2$ scatterer ($V_{xz,xz} \neq V_{yz,yz}$). Tuning the strengths of $V_{xz,xz}$ and $V_{yz,yz}$ tunes the intensity of the $\boldsymbol{q} = (0,\, 2\pi)$ and $(2\pi,\, 0)$ scattering channels respectively; however, the scattering wave vectors remain unchanged and are a more robust measure of orbital ordering. On the other hand, the $\boldsymbol{q} \sim (0,\, 0)$ channel will display anisotropies related to the scattering potential, so we do not analyze it.

Equivalent ten-orbital formulation: We derive an equivalent formulation of the continuum impurity Green's function for ten-orbital TB models, such as those in Refs. [173, 172]. The ten $3d$ orbitals come from the two inequivalent Fe atoms (A and B) of the primitive UC: $(xy)^A$, $(x^2-y^2)^A$, $(ixz)^A$, $(iyz)^A$, $(z^2)^A$, $(xy)^B$, $(x^2-y^2)^B$, $(-ixz)^B$, $(-iyz)^B$, $(z^2)^B$.

We begin with the real-space representation of the continuum impurity Green's function

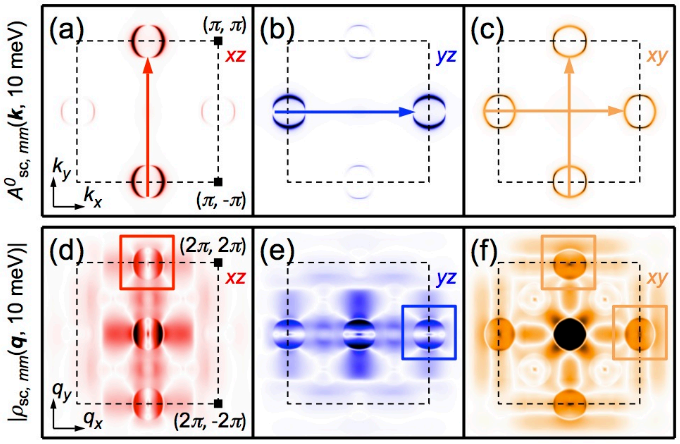

With *xz/yz* order

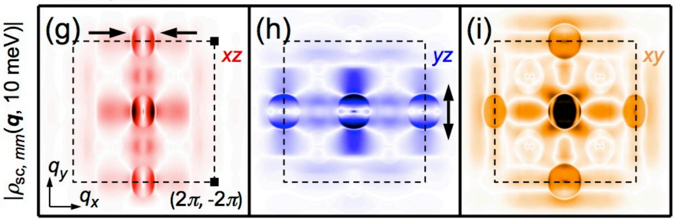

Figure 5.9: Quasiparticle interference simulations in the superconducting state, with isotropic gaps of 14 meV on all bands. (a)-(c) Orbital-resolved spectral function $A^0_{\mathrm{sc},mm}(\boldsymbol{q}, 10\ \mathrm{meV})$. (d)-(f) Orbital-resolved density-of-states modulations $|\rho_{\mathrm{sc},mm}(\boldsymbol{q}, 10\ \mathrm{meV})|$ in the presence of a localized, non-magnetic, s-wave scatterer. (g)-(i) Same as (d)-(f), but including xz/yz orbital ordering ($\Delta_{xz/yz} = 30$ meV).

[Eq. 5.9] for a five-orbital TB model:

$$\mathcal{G}_{mn}(\boldsymbol{r}, \boldsymbol{r'}, \omega) = \sum_{\boldsymbol{ij}} (-p_m)^{-i_x - i_y} (-p_n)^{j_x + j_y} \phi^*_m(\boldsymbol{r} - \boldsymbol{i}) \phi_n(\boldsymbol{r'} - \boldsymbol{j}) \tilde{G}_{mn}(\boldsymbol{i}, \boldsymbol{j}, \omega). \tag{5.15}$$

Here, $\tilde{G}_{mn}(\boldsymbol{i}, \boldsymbol{j}, \omega)$ is the lattice impurity Green's function, given in momentum space by Eq. 5.6. Next, we decompose the Fe lattice into two sublattices:

$$\begin{cases} A = \{\boldsymbol{i} : i_x + i_y = \mathrm{odd}\}, \\ B = \{\boldsymbol{i} : i_x + i_y = \mathrm{even}\}. \end{cases} \tag{5.16}$$

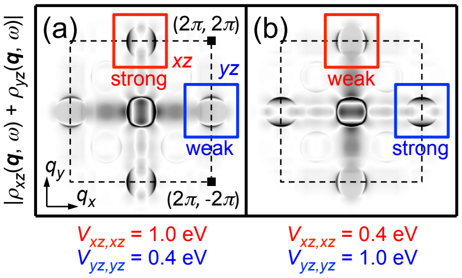

Figure 5.10: QPI simulations in the presence of a localized, anisotropic scatterer. While the relative intensities of the xz/yz scattering channels around $\boldsymbol{q} = (0,\, 2\pi)$ and $(2\pi,\, 0)$ are modified, their wave vectors remain unchanged.

For diagonal terms ($m = n$), the sum in Eq. 5.15 can be split into four contributions:

$$\sum_{\boldsymbol{i},\boldsymbol{j}} (...)(-p_m)^{-i_x - i_y + j_x + j_y} = \sum_{\boldsymbol{i}\in A,\boldsymbol{j}\in A} (...)(+1) + \sum_{\boldsymbol{i}\in A,\boldsymbol{j}\in B} (...)(-p_m) \tag{5.17}$$

$$+ \sum_{\boldsymbol{i}\in B,\boldsymbol{j}\in A} (...)(-p_m) + \sum_{\boldsymbol{i}\in B,\boldsymbol{j}\in B} (...)(+1). \tag{5.18}$$

Taking the Fourier transform of Eq. 5.17 yields

$$\mathcal{G}_{mm}(\boldsymbol{k},\boldsymbol{k'},\omega) = \big[\tilde{\mathbb{G}}_{m,m}(\boldsymbol{k},\boldsymbol{k'},\omega) + p_m\tilde{\mathbb{G}}_{m+5,m}(\boldsymbol{k},\boldsymbol{k'},\omega) + p_m\tilde{\mathbb{G}}_{m,m+5}(\boldsymbol{k},\boldsymbol{k'},\omega) \tag{5.19}$$

$$+ \tilde{\mathbb{G}}_{m+5,m+5}(\boldsymbol{k},\boldsymbol{k'},\omega)\big]\phi^*_m(\boldsymbol{k})\phi_m(\boldsymbol{k'}). \tag{5.20}$$

Here, m runs from 1 through 5, $\mathcal{G}_{mm}(\boldsymbol{k},\boldsymbol{k'},\omega)$ is derived from a five-orbital TB model, and $\tilde{\mathbb{G}}_{mn}(\boldsymbol{k},\boldsymbol{k'},\omega)$ is the lattice Green's function for a ten-orbital TB model. The p_m factors appear because of minus signs present in the orbital definitions of $(-ixz)^B$, $(-iyz)^B$. The middle terms in Eq. 5.19, which mix orbitals m and $m+5$, represent intraorbital basis site interference. Importantly, the sum of these terms are non-zero for a finite Wannier function width. These crucial terms, which have not been considered in previous ten-orbital QPI calculations of Fe-SCs [123], are required in order to reconcile five-orbital and ten-orbital QPI calculations in the presence of non-local tunneling.

Joint density of states: Figure 5.11 demonstrates that our T-matrix simulations can be qualitatively approximated by calculating the joint DOS separately for each orbital:

$$\rho_{mm}(\boldsymbol{q},\omega) \sim \int d^2k A^0_{mm}(\boldsymbol{k},\omega) A^0_{mm}(\boldsymbol{k}+\boldsymbol{q},\omega)\phi^*_m(\boldsymbol{k})\phi_m(\boldsymbol{k}+\boldsymbol{q}). \tag{5.21}$$

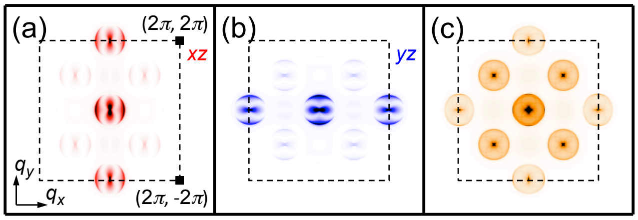

Figure 5.11: Quasiparticle interference simulations derived from calculating the joint density of states separately for each orbital.

5.7 [Supplemental] Symmetry Breaking in Local Defect Structures

In NaFeAs [115, 162], multilayer FeSe [43], and $\mathrm{Ca(Fe_{1x}Co_{x})_2As_2}$ [160], the dominant atomic-scale defects have been shown to pin larger electronic dimers that are unidirectional within nanoscale domains and aligned along one Fe-Fe axis, providing evidence of local nematic ordering. Here we search for a similar effect in single-layer FeSe/$\mathrm{SrTiO_3}$.

A closer inspection of Fig. 5.1(e) reveals a dominant in-plane defect that appears as adjacent bright and dark atoms along the crystalline Fe-Se axes [Fig. 5.12], and exists along all four orientations, like impurities observed in LiFeAs [174, 175]. These defects are similar in their atomic-scale structure and Fe-Se orientation to the dominant defects in NaFeAs [115, 162] and multilayer FeSe [43]. However, the defects observed in single-layer FeSe/$\mathrm{SrTiO_3}$ do not show the larger Fe-Fe electronic dimers. Furthermore, in Sec. 5.4 we considered four different nanoscale domains (20 nm × 20 nm), each containing several such randomly-oriented defects, but our nanoscale wave vector and dispersion analyses found no significant difference in electronic response between the Fe-Fe axes. The chance that the im-

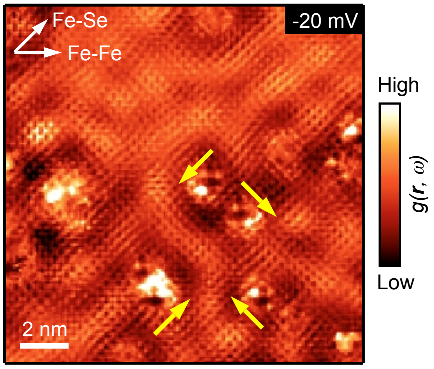

Figure 5.12: (color online) Differential tunneling conductance map revealing dominant type of anisotropic impurities (reproduced from Fig. 5.1(e)). The defects are directed along the crystalline Fe-Se axes and appear in four possible orientations (yellow arrows). Set point: -20 mV, 200 pA, bias oscillation $V_{\mathrm{rms}} = 1.4$ mV.

purity orientations would exactly balance in all four sampled regions is small.

5.8 [Supplemental] Fitting Details

Here we detail the fitting procedures used to derive wave vector bounds on nanoscale orbital ordering [Figs. 5.5 and 5.6]. We performed Gaussian fits using the iterative Levenberg-Marquardt algorithm implemented by Igor Pro. Fit errors were estimated from residuals and represent one standard deviation of the fit coefficient from its true value, assuming independent and identically-distributed Gaussian noise. As seen in Table 5.2, the fit errors (δq_0) for q_0 are insignificant compared to the data resolution δq. Note that σ_q gives the correlation length of the QPI patterns, rather than the uncertainty in its wavevector.

Since there is a sizeable slope in the line cuts, we also performed Gaussian fitting with linear background for comparison [Fig. 5.13 and Table 5.2]. We find that the q_0 values are shifted by amounts smaller than the data resolution δq. The leading error is therefore the data resolution δq, which we report as short horizontal blue and red bars in Figs. 5.5(c) and (d).

Line cut label	Gaussian plus constant background		Gaussian plus linear background	
	$q_0 \pm \delta q_0$ $[2\pi]$	$\sigma_q \pm \delta\sigma_q$ $[2\pi]$	$q_0 \pm \delta q_0$ $[2\pi]$	$\sigma_q \pm \delta\sigma_q$ $[2\pi]$
Area A, 10 meV, xz	0.145±0.002	0.08±0.70	0.1506±0.0007	0.021±0.01
Area A, 10 meV, yz	0.152±0.001	0.017±0.004	0.1584±0.0004	0.0238±0.0006
Area B, 10 meV, xz	0.146±0.001	0.08±0.60	0.1518±0.0006	0.0233±0.0009
Area B, 10 meV, yz	0.133±0.002	0.05±0.04	0.139±0.002	0.027±0.003
Area C, 10 meV, xz	0.1456±0.0005	0.021±0.004	0.148±0.003	0.029±0.004
Area C, 10 meV, yz	0.1429±0.0009	0.1±0.5	0.152±0.001	0.017±0.001
Area A, −10 meV, xz	0.125±0.001	0.026±0.009	0.1307±0.0008	0.021±0.001
Area A, −10 meV, yz	0.130±0.002	0.02±0.01	0.1363±0.0004	0.0257±0.006
Area B, −10 meV, xz	0.1300±0.0003	0.023±0.002	0.1324±0.0006	0.0228±0.0008
Area B, −10 meV, yz	0.1217±0.0007	0.033±0.007	0.1281±0.0009	0.022±0.001
Area D, −10 meV, xz	0.130±0.001	0.018±0.003	0.1361±0.0009	0.023±0.001
Area D, −10 meV, yz	0.1275±0.0006	0.022±0.004	0.129±0.001	0.025±0.002

Table 5.2: Comparison of fit parameters between (1) Gaussians with constant background, $g = g_0 + A\exp(-(q-q_0)^2/(2\sigma_q^2))$ [Figs. 5.5(c)-(d)], and (2) Gaussians with linear background, $g = g_0 + mx + A\exp(-(q-q_0)^2/(2\sigma_q^2))$ [Fig. 5.13]. As reference, the data resolution $\delta q = 0.014$ 2π.

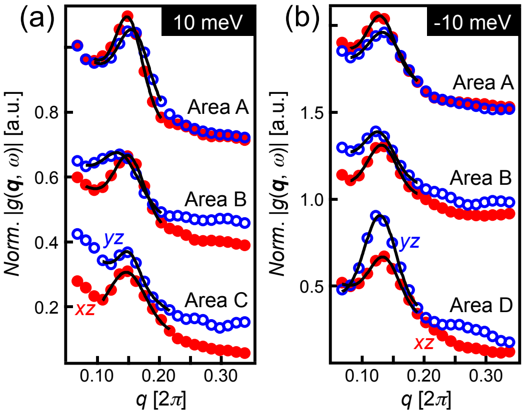

Figure 5.13: Line cuts from conductance maps, reproduced from Figs. 5.5(c)-(d). The solid lines denote Gaussian fits with linear background. Fit parameters are recorded in Table 5.2.

6

Dumbbell Defects in FeSe Films: A Scanning Tunneling Microscopy and First-Principles Investigation

The properties of iron-based superconductors (Fe-SCs) can be varied dramatically with the introduction of dopants and atomic defects. As a pressing example, FeSe, parent phase of the highest-T_c Fe-SC, exhibits prevalent defects with atomic-scale “dumbbell” signatures as imaged by scanning tunneling microscopy (STM). These defects spoil superconductivity when their concentration exceeds 2.5%. Resolving their chemical identity is prerequisite to applications such as nanoscale patterning of superconducting/non-superconducting regions in FeSe, as well as fundamental questions such as the mechanism of superconductivity and the path by which the defects destroy it. We use STM and density functional theory to characterize and identify the dumbbell defects. In contrast to previous speculations about Se adsorbates or substitutions, we find that an Fe-site vacancy is the most energetically favorable defect in Se-rich conditions, and reproduces our observed STM signature. Our calculations shed light more generally on the nature of Se capping, the removal of Fe vacancies via annealing, and their ordering into a $\sqrt{5}\times\sqrt{5}$ superstructure in FeSe and related alkali-doped compounds.

6.1 INTRODUCTION

FeSe, a member of the iron-based superconductors (Fe-SCs) with the simplest stoichiometry, lies at the vanguard of high-T_c materials. On one hand, its anomalous parent phase, with no static magnetic order [155], poses a fresh theoretical challenge [118, 119, 176, 177]. On the other hand, its plain, 2D-layered structure lends itself to bottom-up, nanoscale engineering of its electronic properties. As a striking example, monolayer FeSe interfaced with $SrTiO_3$ [1] exhibits an order-of-magnitude enhancement in its transition temperature T_c (up to 109 K [2]) compared to its bulk value (8 K [3]). Similar T_c boosts up to 48 K have also been attained by depositing K adatoms [100, 101], opening the door to all kinds of adatom modifications of FeSe.

More generally, defects in Fe-SCs are crucial to control T_c [178, 179], raise the critical current J_c through vortex pinning [180, 181], and also serve as microscopic probes of pairing symmetry [182, 183]. Furthermore, defect effects are typically enhanced in 2D systems. An ultimate goal is to control precise placement of atomic defects, possibly through scanning probe lithography, as has been achieved with hydrogenated graphene [184], P dopants in Si [185], and Mn dopants in GaAs [186]. To similarly pattern nanostructures in FeSe, an atomistic understanding of defect formation in this material is needed.

As an intriguing and urgent example, FeSe films grown by molecular beam epitaxy (MBE) exhibit prevalent defects with atomic-scale “dumbbell” signatures as imaged by scanning tunneling microscopy (STM) (also called geometric dimers in Ref. [187]). They consist of two bright lobes on adjacent top-layer Se sites [Figs. 6.1(d)-(f)]. Their concentration is highly tunable, increasing with excess Se flux and decreasing with substrate temperature. Importantly, superconductivity emerges only when their concentration falls below 2.5% [44]. Despite the structural simplicity of FeSe, it is still unknown whether these dumbbell defects are Se adsorbates, antisites, interstitials, or some other type of defect. Their identity is crucial to determine whether or not they can be engineered to define superconducting/non-superconducting regions in FeSe for nanoscale applications.

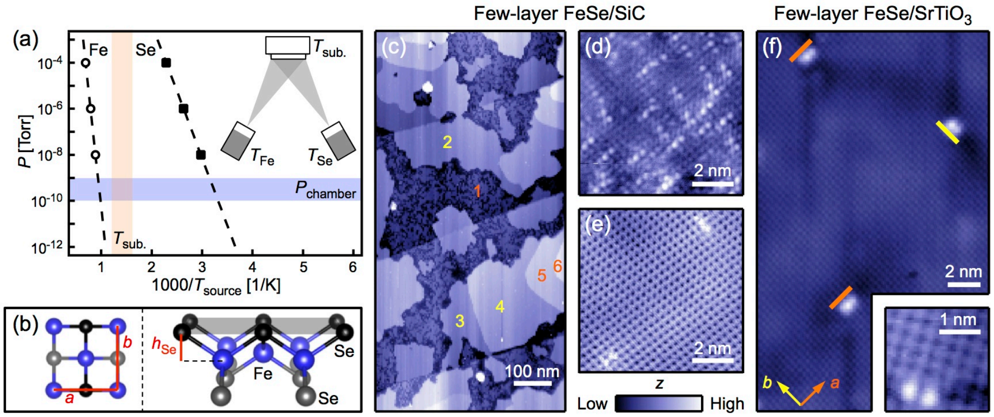

Figure 6.1: (a) Sublimation curves for elemental Fe and Se, reproduced from Ref. [188]. Shaded horizontal and vertical bars mark typical chamber pressures ($10^{-10}$$-$$10^{-9}$ T) and typical substrate temperatures (350$-$550 °C). The inset schematic illustrates FeSe growth via molecular beam epitaxy. (b) Crystal structure of a single layer of FeSe, viewed from the top and side. The shaded plane marks top-layer Se atoms imaged by scanning tunneling microscopy. (c)-(e) Topographic images of few-layer FeSe/SiC. (c) FeSe exhibits island growth on SiC. Numbers indicate unit cell thicknesses. Set point: 4 V, 5 pA; T = 79 K. (d) Dumbbell defects in few-layer FeSe/SiC. Set point: 10 mV, 100 pA; T = 84 K. (e) Same film as in (d), but after annealing at $\sim$450 °C for 2.5 h. Set point: 10 mV, 5 pA; T = 83 K. (f) Dumbbell defects in few-layer FeSe/SrTiO$_3$. Orange and yellow bars mark two possible orientations of the dumbbells. Set point: 100 mV, 5 pA; T = 6.8 K. For inset: 100 mV, 5 pA; T = 6.2 K.

Here we present an STM characterization of dumbbell defects and an exhaustive first-principles theoretical investigation of up to 11 candidate defect configurations that could appear under Se-rich conditions. Using density functional theory (DFT), we find that Fe vacancies have the lowest formation energy. Furthermore, our modeling shows that they perturb orbitals on neighboring Se sites, producing dumbbell signatures when imaged by STM. Based on nudged elastic band calculations and 2D random walk simulations, we explain how

Fe vacancies can diffuse to the edge of terraces during vacuum annealing, consistent with experimental observations of reduced dumbbell density after annealing. We further discuss implications for Se capping of FeSe films for *ex-situ* applications. We also connect our results to previous questions of vacancy ordering in FeSe and related alkali-doped compounds.

6.2 METHODS

Films of FeSe were deposited via MBE on 6H-SiC(0001) and $SrTiO_3(001)$ substrates, following established recipes [43, 44, 1, 96]. The greater volatility of one element (Se) over the other (Fe) motivates two conditions for stoichiometric growth [44]: First, by setting the substrate temperature between the source temperatures, $T_{\mathrm{Fe}} > T_{\mathrm{substrate}} > T_{\mathrm{Se}}$, impinging Fe with temperature $\sim T_{\mathrm{Fe}}$ will be adsorbed with sticking coefficient close to unity, while impinging Se can stick only if they bind to free Fe on the substrate [Fig. 6.1(a)]. Second, to compensate for high Se losses and to mitigate excess Fe clustering, typical molar flux ratios $\Phi_{\mathrm{Se}}/\Phi_{\mathrm{Fe}}$ range from 5 to 20.

Post growth, the films were transfered *in situ* to a homebuilt STM and imaged at liquid nitrogen/helium temperatures. From Figs. 6.1(d)-(f), we enumerate several characteristics of the dumbbell defects: First, their prevalence over any other kinds of defects suggests they are energetically favorable. In few-layer FeSe, this observation is independent of substrate, SiC [Figs. 6.1(c)-(e)] or $SrTiO_3$ [Fig. 6.1(f)]. (We note that single-layer FeSe/$SrTiO_3$, with vastly different superconducting properties, exhibits a different set of defects [96, 117]). Similar dumbbell defects have also been imaged in FeSe crystals grown by vapor transport [163, 189] and in $(Li_{1-x}Fe_xOH)FeSe$ crystals grown by hydrothermal ion exchange [190, 191]. Second, the dumbbells are aligned along both the a and b axes of the 2-Fe unit cell [Figs. 6.1(d)-(f)], pointing to their independence from a structural orthorhombic distortion [103] and electronic nematic state in FeSe [104, 105, 106, 107] that break 90° rotational symmetry. Third, our STM measurements up to $T = 84$ K with bias voltages $10-100$ mV demonstrate that the dumbbell signatures persist well above the superconducting state. Fourth, the dumbbell defects can be removed upon annealing, leaving behind pristine FeSe [Fig. 6.1(e)].

We performed DFT calculations using `VASP` [152, 151]. We used the PBE exchange-correlation functional [150], and the projector augmented wave (PAW) method, with Fe $4s$, $3d$ and Se $4s$, $4p$ electrons treated as valence. An energy cutoff of 450 eV and Methfessel-Paxton smearing [153] with $\sigma = 0.1$ eV were employed. We modeled defects within freestanding monolayer and bilayer FeSe supercells (details in Table 6.1), with full relaxation of internal atomic coordinates (corresponding to a magnitude of the force per atom < 0.025 eV/Å). To reproduce the experimental c-axis value, we included van der Waals corrections in the bilayer calculations using the DFT-D2 method [192], with dispersion potential parameters taken from Ref. [193] (tested for bulk FeSe and FeTe).

	Monolayer	Bilayer	Bulk (expt.)
Functional:	GGA	GGA/DFT-D2	
Supercell size:	4×4	3×3	
BZ sampling:	2×2×1	4×4×1	
a=b [Å]:	3.69	3.64	3.7707
c [Å]:		5.47	5.521
h_{Se} [Å]:	1.38	1.40	1.472
$c_{\mathrm{supercell}}$ [Å]:	20	25	

Table 6.1: Relaxed parameters of monolayer and bilayer FeSe supercells used to simulate defect configurations. a, b, c are the crystal lattice constants for a 2-Fe unit cell, h_{Se} is the internal Se height, and $c_{\mathrm{supercell}}$ includes vacuum regions. Experimental values are based on X-ray powder diffraction [46].

6.3 RESULTS

Given the correlation of dumbbell defects with excess Se flux, we examine candidate defects in which $N_{\mathrm{Se}} > N_{\mathrm{Fe}}$. Although the dumbbell signature is centered above an Fe site, we explore all possible binding sites for completeness. We begin with isolated Se adatoms as the simplest class of Se-rich defects. Among three adsorption sites (see Section 6.5), the hollow site in FeSe, directly above a bottom-layer Se atom, is most stable [Fig. 6.2(a)-(b)]. We compute the binding energy as

$$E_{\text{adatom}} = E(D) - E(0) - E_{\text{Se}}, \tag{6.1}$$

where $E(D)$ is the DFT total energy of the system including the adatom, $E(0)$ is the total energy of pristine FeSe within the same supercell, and E_{Se} is the energy of an isolated Se atom. We find that $E_{\text{adatom}} = -3.14$ eV (-3.02 eV) for monolayer (bilayer) FeSe, which suggests chemisorption. Examining the relaxed structure [Fig. 6.2(b)], we observe that the Se adatom can come within bonding distance of neighboring Fe atoms and distort their equilibrium positions. Importantly, given that T_c in Fe-SCs is highly sensitive to the Fe-Se/As height [194], our result points to a microscopic explanation of why Se is a poor capping material.

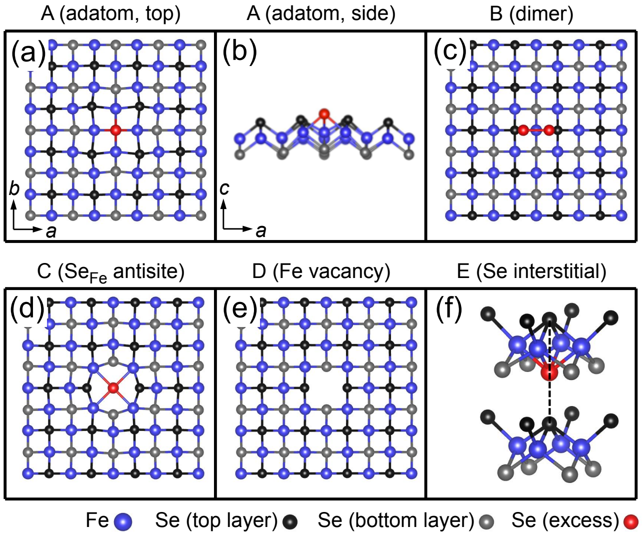

Figure 6.2: Relaxed defect structures. For the interstitial configuration (f), only a fraction of the bilayer FeSe 3×3 supercell is shown for clarity. Fe atoms are violet and top/bottom Se atoms are black/gray. Excess Se atoms are colored red for distinction.

We next examine adsorbed Se_2 dimers. We find that among four possible adsorption geometries (see Section 6.5), two are nearly degenerate, one of which has the Se_2 molecule centered above an Fe site [Fig. 6.2(c)]. Furthermore, with binding energy defined as

$$E_{\text{dimer}} = E(D) - E(0) - E_{\text{Se}_2}, \tag{6.2}$$

where E_{Se_2} is the energy of an isolated Se_2 molecule, we calculate $E_{\text{dimer}} = -0.39$ eV (-0.69 eV) for monolayer (bilayer) FeSe. These values suggest that Se_2 dimers are weakly physisorbed and may have short adsorption lifetimes. We contrast this result to the case of GaAs(001)-(2×4), where surface dangling bonds can stabilize adsorbed As_2 dimers or As_4 tetramers with calculated binding energies up to -1.6 eV [195]. Such dangling bonds are absent in the top layer of FeSe. As a side note, our DFT calculations suggest that adsorption can be enhanced if two surface dimers cluster into Se_4, but this would produce an unobserved four-lobe STM topographic signature.

Alternatively, some studies have proposed that a perturbation at the Fe site (either an unknown repulsive potential [196] or Se subsitution [75]) could affect the orbitals on neighbouring Se atoms and generate a dumbbell signature. We consider three possibilities: Se_{Fe} antisites, Fe-site vacancies, and Se interstitials, perhaps binding to a surface-layer Fe atom from below. As seen in Fig. 6.2(d), the antisite configuration in the monolayer supercell produces pronounced distortions of nearby atoms. Fe atoms are pulled closer to the antisite, and Se atoms are pushed away. Figure 6.2(e) shows an Fe vacancy. Figure 6.2(f) shows the most stable Se interstitial configuration, where the excess Se atom lies beneath a top-layer Se site, not an Fe site.

To compare formation energies E_F among the aforementioned defects with variable stoichiometry, we include the energetic costs of incorporating n_{Fe} (n_{Se}) additional Fe (Se) atoms from a reservoir into the defect:

$$E_f = E(D) - E(0) - n_{\text{Fe}}\mu_{\text{Fe}} - n_{\text{Se}}\mu_{\text{Se}}. \tag{6.3}$$

Assuming quasi-equilibrium growth of FeSe and no bulk Fe or Se precipitation, we impose the following constraints on the chemical potentials: (i) $\mu_{\mathrm{Fe}} + \mu_{\mathrm{Se}} = \mu_{\mathrm{FeSe}}$; (ii) $\mu_{\mathrm{Fe}} < \mu_{\mathrm{Fe}}^{\mathrm{bulk}}$; (iii) $\mu_{\mathrm{Se}} < \mu_{\mathrm{Se}}^{\mathrm{bulk}}$. Eq. (6.3) then yields

$$E_f = E(D) - E(0) - n_{\mathrm{Fe}}\mu_{\mathrm{FeSe}} - (n_{\mathrm{Se}} - n_{\mathrm{Fe}})\mu_{\mathrm{Se}}, \tag{6.4}$$

where $\mu_{\mathrm{FeSe}} - \mu_{\mathrm{Fe}}^{\mathrm{bulk}} < \mu_{\mathrm{Se}} < \mu_{\mathrm{Se}}^{\mathrm{bulk}}$. Figures 6.3(a), (b) show results for monolayer and bilayer FeSe supercells. In both cases the Fe vacancy possesses the lowest formation energy by a margin of at least -0.5 eV within estimated μ_{Se} ranges.

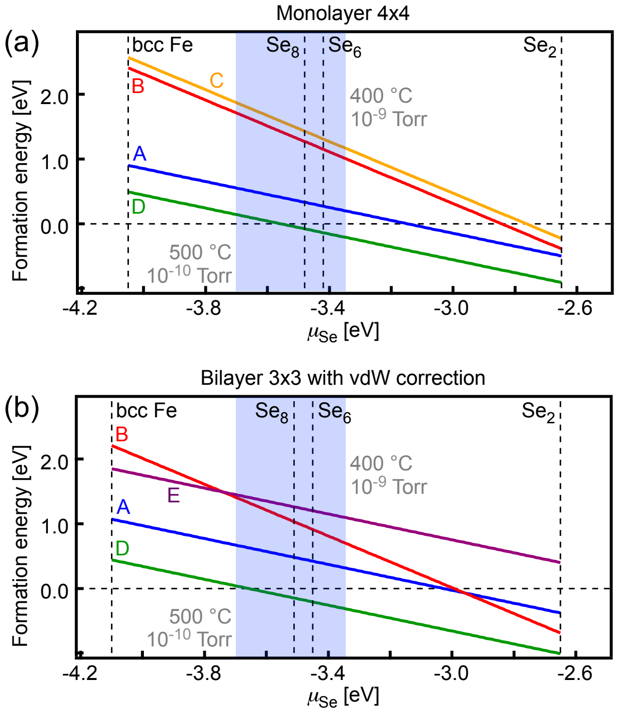

Figure 6.3: Formation energies of defect configurations in the (a) 4×4 supercell monolayer and (b) 3×3 supercell bilayer FeSe. Capital letters correspond to labeled defects in Fig. 6.2. Assuming no condensation of bulk Fe (body-centered cubic) or Se (Se_6 and Se_8 rings), chemical potential values μ_{Se} are restricted between the dashed lines labeled bcc Fe and $\mathrm{Se}_6/\mathrm{Se}_8$. μ_{Se} is set to zero for an isolated Se atom. Alternatively, shaded blue regions mark estimated μ_{Se} values at typical substrate temperatures and Se partial pressures, using ideal gas approximations and tabulated thermodynamic quantities (see Section 6.6).

Having identified the Fe vacancy as the lowest-energy, Se-rich defect of FeSe, we considered whether it can produce a dumbbell signature. Figures 6.4(a), (b) show a charge density isosurface, integrated from the Fermi energy up to 50 meV. For improved accuracy, we increased the BZ sampling to 8×8×1 and used tetrahedron smearing with Blöchl corrections [197]. Due to the missing Fe atom, orbitals on neighboring Se atoms protrude further out. We simulate an STM topography by tracing the height of the charge density isosurface and applying Gaussian smoothing to approximate a finite tip radius. As seen in Fig. 6.4(c), the two protruding Se orbitals appear as bright lobes of a dumbbell, matching the experimental image [Fig. 6.4(d)].

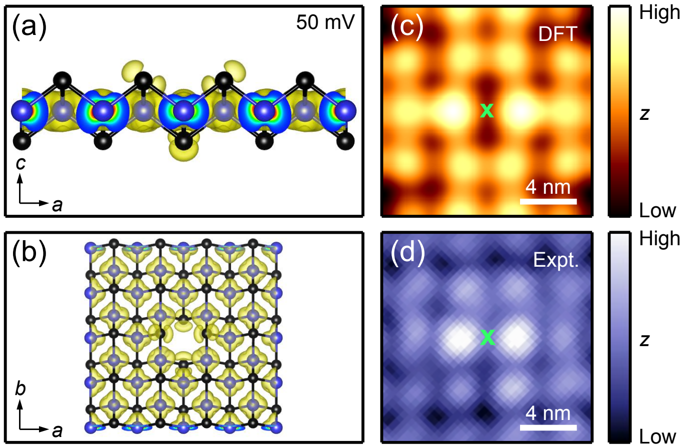

Figure 6.4: (a), (b) Charge density isosurfaces for the Fe vacancy defect configuration, integrated from the Fermi energy up to 50 meV. (c) Simulated STM topography of the Fe vacancy site, marked by a green “x”; the neighboring Se atoms exhibit brighter lobes, producing a dumbbell signature. (d) Experimental topography (single-layer FeSe/$SrTiO_3$) for comparison. Set point: 50 mV, 500 pA; T = 5 K.

If the dumbbell defects are Fe vacancies, they must also be capable of diffusing to the edge of typical film terraces at high temperatures, as implied by Fig. 6.1(e). To elucidate this process, we performed nudged elastic band calculations to find the minimum energy path associated with Fe vacancy hopping [198, 199]. We used a smaller $4/\sqrt{2} \times 4/\sqrt{2} \times 1$ supercell with $4 \times 4 \times 1$ BZ sampling. We computed seven intermediate images, each relaxed with total force per atom (tangential and chain) < 0.025 eV/Å.

Figure 6.5 shows the relative energy along the diffusion path, with insets depicting initial, transition, and final states. In the transition state, two neighboring Se atoms (circled in blue) are pushed above and below the plane, suggesting that vacancy diffusion may be easier on the surface than in the bulk, as expected. We calculate the diffusion rate as

$$\Gamma = \nu \exp\left[-\frac{E_B}{k_B T}\right], \tag{6.5}$$

where ν is the attempt frequency and $E_B = 1.69$ eV is the barrier height. From Vineyard transition-rate theory [200, 201] (see Section 6.8),

$$\nu = \left(\frac{k_B T}{2\pi m_{\mathrm{Fe}}}\right)^{1/2} \left[\int_{x_i}^{x_B} dx \exp\left[-\frac{E(x)}{k_B T}\right]\right]^{-1}, \tag{6.6}$$

where m_{Fe} is the mass of an Fe atom and x_i (x_B) is the initial-state (transition-state) position of the hopping Fe atom. Then for a random walk over a 2D lattice, the root-mean-square distance traveled after time t is

$$x_{\mathrm{rms}} = d_{\text{Fe-Fe}}\sqrt{\Gamma t}, \tag{6.7}$$

where $d_{\text{Fe-Fe}} = a/\sqrt{2}$. If we anneal at 450 °C for 2.5 h [Fig. 6.1(e)], we estimate x_{rms} to be 950 Å. This distance exceeds typical film island dimensions [Fig. 6.1(c)], thereby explaining how dumbbell defects are removed upon annealing.

6.4 DISCUSSION

We draw a final connection between dumbbell defects and Fe vacancies. At large dumbbell concentrations, Song *et al.* [44] found that the defects ordered into a $\sqrt{5}\times\sqrt{5}$ superstructure. Similarly, electron diffraction measurements of FeSe crystals, nanosheets, and nanowires have revealed various types of Fe-vacancy order, including $\sqrt{5}\times\sqrt{5}\times 1$ [202]. Given that the Fe vacancy is the thermodynamically most stable defect, the closest packing of these vacan-

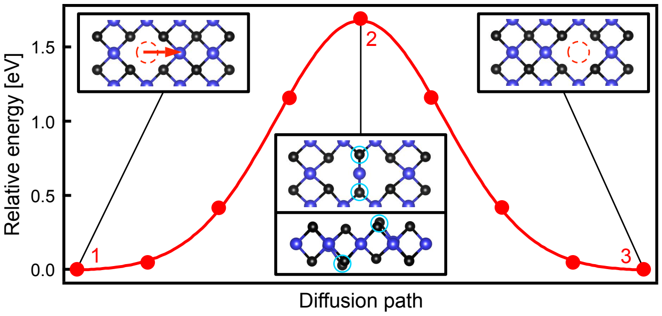

Figure 6.5: Nudged elastic band calculation for nearest-neighbor hopping of an Fe vacancy. The diffusion barrier height is 1.69 eV. Insets depict (1) initial, (2) transition, and (3) final states.

cies would lead to a $\sqrt{5}\times\sqrt{5}$ arrangement, because any closer packing would produce multivacancy defects (two or more nearest neighbor Fe atoms mising), which would likely destabilize the crystal altogether. This argument provides an explanation of the $\sqrt{5}\times\sqrt{5}$ pattern (see Section 6.9 for additional calculations).

The identification of the $\sqrt{5}\times\sqrt{5}$ dumbbell superstructure with Fe-vacancy order has further significance. Investigations of the related compound $A_x\mathrm{Fe}_{2-y}\mathrm{Se}_2$ (A = alkali metal), with enhanced T_c up to 32 K [203, 204], have been complicated by mesoscale phase separation into multiple Fe-vacancy reconstructions [205, 206, 207, 208, 209]. Our calculations suggest that Fe vacancy order is not a pathological feature of $A_x\mathrm{Fe}_{2-y}\mathrm{Se}_2$, but a phenomenon intrinsic to FeSe grown under excess Se flux. The crucial distinction is that in the latter case, Fe vacancies can be removed upon annealing, while in the former, Fe vacancy diffusion may be hindered by the buffer A_x layers. This additional flexibility in FeSe may afford better control of stoichiometric (superconducting) and ordered vacancy (non-superconducting) phases for nanoscale patterning.

In conclusion, we have established the chemical identity of dumbbell defects that appear in MBE-grown FeSe under excess Se flux and suppress superconductivity with concentrations greater than 2.5%. Our DFT calculations show that Fe vacancies (1) are energetically most favorable, (2) produce dumbbell signatures consistent with STM images, and (3) can diffuse to the edge of typical film islands with vacuum annealing. These atomistic insights lay the foundation towards controlling precise placements of such defects. We also reiterate that Se may be a poor choice of capping material to perform *ex-situ* measurements due to induced distortions within the underlying FeSe. Finally, we suggest a broader, microscopic connection between dumbbell defect phenomenology in FeSe and mesoscale phase separation in $A_x\mathrm{Fe}_{2-y}\mathrm{Se}_2$.

6.5 [Supplemental] Additional Defect Configurations

Figure 6.6 shows all defect configurations examined in this work, which fall into five categories: (A) Se adatoms, (B) Se_2 dimers, (C) $\mathrm{Se}_{\mathrm{Fe}}$ antisites, (D) Fe vacancies, and (E) Se interstitials. All defects were simulated within both monolayer and bilayer FeSe supercells, except for (C), where in the case of a bilayer FeSe supercell, the $\mathrm{Se}_{\mathrm{Fe}}$ antisite could not be held in its place during structural relaxation, and (E1) and (E2), which are not defined for monolayer FeSe. Their corresponding formation energies are plotted in Fig. 6.7. The most stable configuration for each defect category is enclosed in a red box in Fig. 6.6. Configurations that are laterally centered at an Fe site, consistent with the STM dumbbell signature, are marked by a black horizontal bar.

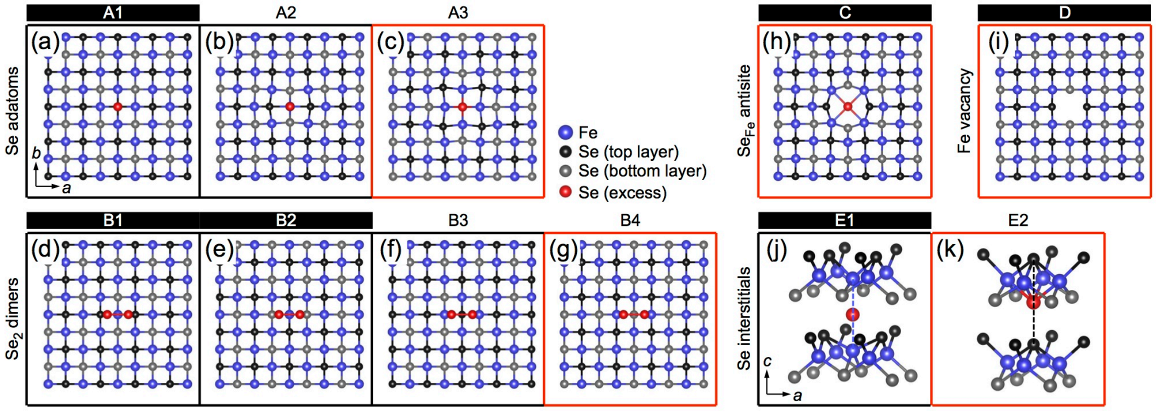

Figure 6.6: Additional relaxed defect structures. (j), (k) Only a fraction of the bilayer FeSe 3×3 supercell is shown for clarity. Fe atoms are violet and top/bottom Se atoms are black/gray. Excess Se atoms are colored red for distinction.

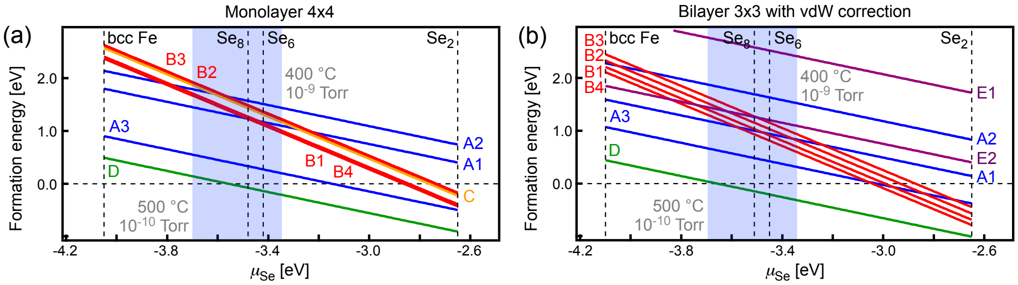

Figure 6.7: Formation energies of defect configurations in the (a) 4×4 supercell monolayer and (b) 3×3 supercell bilayer FeSe. Reproduced from Fig. 6.3, with additional defect structures shown in Fig. 6.6.

6.6 [SUPPLEMENTAL] SELENIUM CHEMICAL POTENTIAL

Following Ref. [210], we estimate the experimental chemical potential of Se using ideal gas approximations and tabulated thermodynamic quantities. Under fixed temperature T and pressure p, the chemical potential of an ideal gas of Se_2 molecules is related to the Gibbs free energy as

$$\mu_{\mathrm{Se}}(T,p) = \frac{G_{\mathrm{Se}_{2(g)}}(T,p)}{2N}, \tag{6.8}$$

where N is the number of Se_2 molecules. First, we compute $G_{\mathrm{Se}_{2(g)}}$ at standard conditions ($T^\circ = 298.15$ K, $p^\circ = 1$ bar),

$$G_{\mathrm{Se}_{2(g)}}(T^\circ, p^\circ) = H_{\mathrm{Se}_{2(g)}}(T^\circ, p^\circ) - T^\circ S_{\mathrm{Se}_{2(g)}}(T^\circ, p^\circ), \tag{6.9}$$

using enthalpy $H_{\mathrm{Se}_{2(g)}}(T^\circ, p^\circ)$ and entropy $S_{\mathrm{Se}_{2(g)}}(T^\circ, p^\circ)$ values derived from thermochemistry references. Next, we extrapolate to desired temperatures using reference heat capacity data,

$$G_{\mathrm{Se}_{2(g)}}(T, p^\circ) = H_{\mathrm{Se}_{2(g)}}(T^\circ, p^\circ) + \int_{T^\circ}^{T} dT' C_{p^\circ,\mathrm{Se}_{2(g)}}(T') - T\left[S_{\mathrm{Se}_{2(g)}}(T^\circ, p^\circ) + \int_{T^\circ}^{T} dT' \frac{C_{p^\circ,\mathrm{Se}_{2(g)}}(T')}{T'}\right], \tag{6.10}$$

and desired pressures using ideal gas relationships,

$$G_{\mathrm{Se}_{2(g)}}(T,p) = G_{\mathrm{Se}_{2(g)}}(T,p^\circ) + Nk_BT\ln\left(\frac{p}{p^\circ}\right). \tag{6.11}$$

We make some practical remarks on estimating $\mu_{\mathrm{Se}}(T,p)$:

(1) To maintain consistency with DFT calculations and total energies (E) defined in VASP, we set $\mu_{\mathrm{Se}}(0\text{ K},p) = E_{\mathrm{Se}} = 0$ for an isolated Se *atom*.

(2) Based on the chosen reference, we compute $H_{\mathrm{Se}_{2(g)}}(T^\circ,p^\circ)$ in a two-step process:

$$\begin{cases} 2\mathrm{Se}_{(g)}(0\text{ K},p^\circ) \to 2\mathrm{Se}_{(g)}(T^\circ,p^\circ), & \Delta H_1 = 2(\tfrac{5}{2}k_BT^\circ),\ \text{ideal monoatomic gas,} \\ 2\mathrm{Se}_{(g)}(T^\circ,p^\circ) \to \mathrm{Se}_{2(g)}(T^\circ,p^\circ), & \Delta H_2 = 2(-165.520 \pm 0.250)\text{ kJmol}^{-1},\ \text{p. 53 of Ref. [211].} \end{cases} \tag{6.12}$$

(3) From p. 40 of Ref. [211], $S_{\mathrm{Se}_{2(g)}}(T^\circ,p^\circ) = 247.380 \pm 0.400\text{ JK}^{-1}\text{mol}^{-1}$.

(4) From p. 63 of Ref. [211], $C_{p^\circ,\mathrm{Se}_{2(g)}}(T) = a + bT + cT^2 + dT^{-1} + eT^{-2}$, where $a = 1.93485 \times 10\text{ JK}^{-1}\text{mol}^{-1}$, $b = 1.24903 \times 10^{-2}\text{ JK}^{-2}\text{mol}^{-1}$, $c = -2.07010 \times 10^{-6}\text{ JK}^{-3}\text{mol}^{-1}$, $d = 1.09846 \times 10^{4}\text{ Jmol}^{-1}$, and $e = -1.60249 \times 10^{6}\text{ JKmol}^{-1}$. These values are valid from $T =$ 298 K to 1300 K.

(5) We choose T to be the substrate temperature and p to be the Se partial pressure in the chamber, based on quasi-equilibrium growth assumptions suggested for similar III-V semiconductor MBE processes [212, 213]. For $T = 400$ °C and $p = 10^{-9}$ T, we find that $\mu_{\mathrm{Se}} = -3.35$ eV. For $T = 500$ °C and $p = 10^{-10}$ T, we find that $\mu_{\mathrm{Se}} = -3.70$ eV.

6.7 [SUPPLEMENTAL] SIMULATED BIAS-DEPENDENT TOPOGRAPHY

Figure 6.8 shows STM topographic simulations of an Fe vacancy with different imaging biases V, carried out by integrating the charge density from the Fermi energy to eV. We note that experimental FeSe bands exhibits orbital-dependent renormalization with an average factor $1/z = 1/6$ relative to LDA/GGA-calculated bands [214, 106, 172], precluding a more detailed *ab-initio* analysis of STM defect signatures.

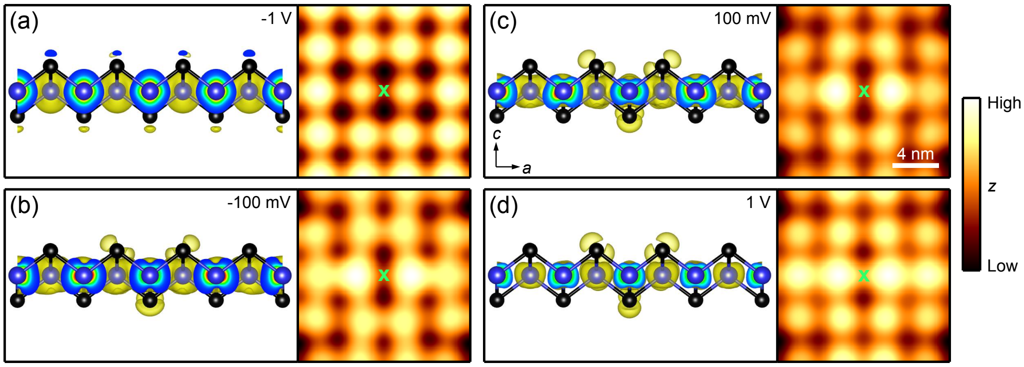

Figure 6.8: Charge density isosurfaces and simulated STM topographies of an Fe vacancy, calculated for different imaging biases. The Fe vacancy site is marked by a green "x."

6.8 [SUPPLEMENTAL] VINEYARD TRANSITION-RATE THEORY

The classical probability distribution for an ensemble of identical, non-interacting particles moving in a 1D potential $\Phi(x)$ is given by

$$p(x, v) = \rho_0 \left(\frac{m}{2\pi k_B T} \right)^{1/2} \exp \left[-\frac{\Phi(x)}{k_B T} - \frac{mv^2}{2k_B T} \right], \tag{6.13}$$

where m is the particle mass, v is its velocity, and ρ_0 is a normalization constant. We consider a finite spatial region in phase space, $x \in [x_i, x_f]$, with a potential barrier peaked at $x_B \in (x_i, x_f)$. The average transition rate $\Gamma_{x_i \to x_f}$ is given by I/Q, where I is the phase space current across the barrier and Q is the number of states in $[x_i, x_B]$ [200]. From Eq. (6.13), we find that

$$Q = \int_{x_i}^{x_B} dx \int_{-\infty}^{\infty} dv p(x, v) = \rho_0 \int_{x_i}^{x_B} dx \exp \left[-\frac{\Phi(x)}{k_B T} \right] \tag{6.14}$$

and

$$I = \int_0^{\infty} dv v p(x_B, v) = \rho_0 \exp \left[-\frac{\Phi(x_B)}{k_B T} \right] \left(\frac{k_B T}{2\pi m} \right)^{1/2}, \tag{6.15}$$

which yields

$$\Gamma_{x_i \to x_f} = \left(\frac{k_B T}{2\pi m} \right)^{1/2} \left[\int_{x_i}^{x_B} dx \exp\left[-\frac{\Phi(x)}{k_B T} \right] \right]^{-1} \exp\left[-\frac{\Phi(x_B)}{k_B T} \right]. \tag{6.16}$$

In our application to an Fe atom hopping to a neighboring vacant site in FeSe, we take $m = m_{\mathrm{Fe}}$, and $\Phi(x)$ to be the DFT total energy E along the diffusion path, parameterized by the position x of the moving Fe atom [215].

6.9 [Supplemental] $\sqrt{5}\times\sqrt{5}$ Vacancy Order

We show that a $\sqrt{5}\times\sqrt{5}$ ordering of Fe vacancies in FeSe is thermodynamically stable under excess Se flux. Following the same reasoning in the main text, the formation energy of $\mathrm{Fe}_{1-x}\mathrm{Se}$, where $0 \leq x \leq 1$, is given by

$$E_f = E(\mathrm{Fe}_{1-x}\mathrm{Se}) - E(\mathrm{FeSe}) + x(\mu_{\mathrm{FeSe}} - \mu_{\mathrm{Se}}). \tag{6.17}$$

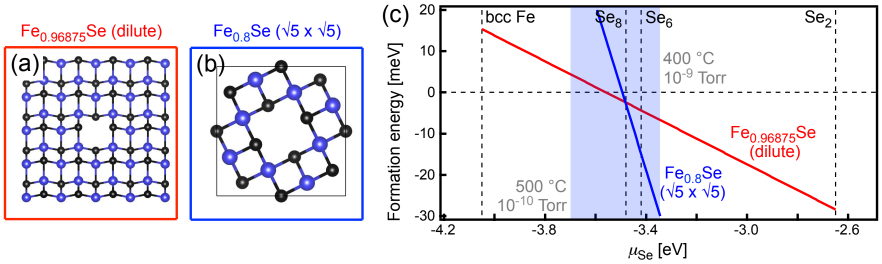

Figure 6.9: Formation energies of $\mathrm{Fe}_{1-x}\mathrm{Se}_x$ for two concentrations of Fe vacancies: (a) $x = 0.03125$ (dilute), and (b) $x = 0.2$ ($\sqrt{5}\times\sqrt{5}$ order). (c) Assuming no condensation of bulk Fe (body-centered cubic) or Se (Se_6 and Se_8 rings), chemical potential values μ_{Se} are restricted between the dashed lines labeled bcc Fe and $\mathrm{Se}_6/\mathrm{Se}_8$. μ_{Se} is set to zero for an isolated Se atom. Alternatively, shaded blue regions mark estimated μ_{Se} values at typical substrate temperatures and Se partial pressures, using ideal gas approximations and tabulated thermodynamic quantities.

We consider two concentrations:

(1) Dilute: $x = 0.03125$. This value corresponds to one Fe vacancy in a monolayer 4×4 supercell [Fig. 6.9(a)].

(2) $\sqrt{5}\times\sqrt{5}$ Fe vacancy order: $x = 0.2$. For this DFT calculation, we use a monolayer $\sqrt{5}\times\sqrt{5}$ supercell [Fig. 6.9(b)] with 5×5×1 BZ sampling.

Figure 6.9(c) demonstrates that within a narrow range of viable μ_{Se} values, the $\sqrt{5}\times\sqrt{5}$ Fe vacancy superstructure is more energetically favorable compared to a dilute Fe vacancy.

References

[1] Q.-Y. Wang, Z. Li, W.-H. Zhang, Z.-C. Zhang, J.-S. Zhang, W. Li, H. Ding, Y.-B. Ou, P. Deng, K. Chang, J. Wen, C.-L. Song, K. He, J.-F. Jia, S.-H. Ji, Y.-Y. Wang, L.-L. Wang, X. Chen, X.-C. Ma, and Q.-K. Xue, Chin. Phys. Lett. **29**, 037402 (2012).

[2] J.-F. Ge, Z.-L. Liu, C. Liu, C.-L. Gao, D. Qian, Q.-K. Xue, Y. Liu, and J.-F. Jia, Nat. Mater. **14**, 285 (2015).

[3] F.-C. Hsu, J.-Y. Luo, K.-W. Yeh, T.-K. Chen, T.-W. Huang, P. M. Wu, Y.-C. Lee, Y.-L. Huang, Y.-Y. Chu, D.-C. Yan, and M.-K. Wu, Proc. Natl. Acad. Sci. **105**, 14262 (2008).

[4] O. Pietzsch, A. Kubetzka, D. Haude, M. Bode, and R. Wiesendanger, Rev. Sci. Instrum. **71**, 424 (2000).

[5] S. Meckler, M. Gyamfi, O. Pietzsch, and R. Wiesendanger, Rev. Sci. Instrum. **80**, 023708 (2009).

[6] E. Main, *Investigating Atomic Scale Disordered Stripes in the Cuprate Superconductors with Scanning Tunneling Microscopy*, Ph.D. thesis, Harvard University (2011).

[7] R. Wiesendanger, Rev. Mod. Phys. **81**, 1495 (2009).

[8] M. Bode, Rep. Prog. Phys. **66**, 523 (2003).

[9] M. Cavallini and F. Biscarini, Rev. Sci. Instrum. **71**, 4457 (2000).

[10] S. F. Ceballos, G. Mariotto, S. Murphy, and I. V. Shvets, Surf. Sci. **523**, 131 (2003).

[11] I. Shvets, R. Wiesendanger, D. Bürgler, G. Tarrach, H.-J. Güntherodt, and J. Coey, J. Appl. Phys. **71**, 5489 (1992).

[12] A. Li Bassi, C. S. Casari, D. Cattaneo, F. Donati, S. Foglio, M. Passoni, C. E. Bottani, P. Biagioni, A. Brambilla, M. Finazzi, F. Ciccacci, and L. Duò, Appl. Phys. Lett. **91**, 173120 (2007).

[13] A. Kubetzka, M. Bode, O. Pietzsch, and R. Wiesendanger, Phys. Rev. Lett. **88**, 057201 (2002).

[14] G. Rodary, J.-C. Girard, L. Largeau, C. David, O. Mauguin, and Z.-Z. Wang, Appl. Phys. Lett. **98**, 082505 (2011).

[15] M. Corbetta, S. Ouazi, J. Borme, Y. Nahas, F. Donati, H. Oka, S. Wedekind, D. Sander, and J. Kirschner, Jpn. J. Appl. Phys. **51**, 030208 (2012).

[16] A. Schlenhoff, S. Krause, G. Herzog, and R. Wiesendanger, Appl. Phys. Lett. **97**, 083104 (2010).

[17] J. P. Ibe, P. P. Bey, S. L. Brandow, R. A. Brizzolara, N. A. Burnham, and D. P. Dilella, J. Vac. Sci. Technol. A **8**, 3750 (1990).

[18] F. Bastiman, A. G. Cullis, M. Hopkinson, and K. J. Briston, J. Vac. Sci. Technol. B **28**, 371 (2010).

[19] C. Chen, *Introduction to Scanning Tunneling Microscopy*, 2nd ed. (2007).

[20] T. Iijima and K. Yasuda, Jpn. J. Appl. Phys. **27**, 1546 (1988).

[21] P. J. Bryant, H. Kim, Y. Zheng, and R. Yang, Rev, Sci. Instrum. **58**, 1115 (1987).

[22] A. I. Oliva, A. Romero G., J. L. Peña, E. Anguiano, and M. Aguilar, Rev. Sci. Instrum. **67**, 1917 (1996).

[23] M. Passoni, F. Donati, A. Li Bassi, C. Casari, and C. Bottani, Phys. Rev. B **79**, 045404 (2009).

[24] T. Kimura, Y. Tomioka, H. Kuwahara, A. Asamitsu, M. Tamura, and Y. Tokura, Science **274**, 1698 (1996).

[25] Q. Li, K. E. Gray, and J. F. Mitchell, Phys. Rev. B **59**, 9357 (1999).

[26] J. F. Mitchell, J. E. Millburn, M. Medarde, D. N. Argyriou, and J. D. Jorgensen, J. Appl. Phys. **85**, 4352 (1999).

[27] J. F. Mitchell, D. N. Argyriou, A. Berger, K. E. Gray, R. Osborn, and U. Welp, J. Phys. Chem. B **105**, 10731 (2001).

[28] U. Welp, A. Berger, V. K. Vlasko-Vlasov, H. You, K. E. Gray, and J. F. Mitchell, J. Appl. Phys. **89**, 6621 (2001).

[29] M. Konoto, T. Kohashi, K. Koike, T. Arima, Y. Kaneko, T. Kimura, and Y. Tokura, Phys. Rev. Lett. **93**, 107201 (2004).

[30] X. Huang, O. Mryasov, D. Novikov, and A. Freeman, Phys. Rev. B **62**, 13318 (2000).

[31] R. Saniz, M. Norman, and A. Freeman, Phys. Rev. Lett. **101**, 236402 (2008).

[32] Z. Sun, Q. Wang, J. F. Douglas, H. Lin, S. Sahrakorpi, B. Barbiellini, R. S. Markiewicz, A. Bansil, A. V. Fedorov, E. Rotenberg, H. Zheng, J. F. Mitchell, and D. S. Dessau, Sci. Rep. **3**, 3167 (2013).

[33] F. Loviat, H. M. Rønnow, C. Renner, G. Aeppli, T. Kimura, and Y. Tokura, Nanotechnol. **18**, 044020 (2007).

[34] H. M. Rønnow, C. Renner, G. Aeppli, T. Kimura, and Y. Tokura, Nature **440**, 1025 (2006).

[35] F. Massee, S. D. Jong, Y. Huang, W. K. Siu, I. Santoso, A. Mans, A. T. Boothroyd, D. Prabhakaran, R. Follath, A. Varykhalov, L. Patthey, M. Shi, J. B. Goedkoop, and M. S. Golden, Nat. Phys. **7**, 978 (2011).

[36] S. Santis, B. Bryant, M. Warner, H. Wang, T. Kimura, Y. Tokura, C. Renner, A. Bianconi, and G. Aeppli, J. Supercond. Nov. Magn. **20**, 531 (2007).

[37] B. Bryant, C. Renner, Y. Tokunaga, Y. Tokura, and G. Aeppli, Nat. Commun. **2**, 212 (2011).

[38] D. Dessau, T. Saitoh, C.-H. Park, Z.-X. Shen, P. Villella, N. Hamada, Y. Moritomo, and Y. Tokura, Phys. Rev. Lett. **81**, 192 (1998).

[39] N. Mannella, W. L. Yang, X. J. Zhou, H. Zheng, J. F. Mitchell, J. Zaanen, T. P. Devereaux, N. Nagaosa, Z. Hussain, and Z.-X. Shen, Nature **438**, 474 (2005).

[40] J. Bardeen, Phys. Rev. Lett. **6**, 57 (1961).

[41] R. Wiesendanger, H.-J. Güntherodt, G. Güntherodt, R. J. Gambino, and R. Ruf, Phys. Rev. Lett. **65**, 247 (1990).

[42] H. Okamoto, J. Phase Equilib. **12**, 383.

[43] C.-L. Song, Y.-L. Wang, P. Cheng, Y.-P. Jiang, W. Li, T. Zhang, Z. Li, K. He, L. Wang, J.-F. Jia, H.-H. Hung, C. Wu, X. Ma, X. Chen, and Q.-K. Xue, Science **332**, 1410 (2011).

[44] C.-L. Song, Y.-L. Wang, Y.-P. Jiang, Z. Li, L. Wang, K. He, X. Chen, X.-C. Ma, and Q.-K. Xue, Phys. Rev. B **84**, 020503 (2011).

[45] J. Simonin, Phys. Rev. B **33**, 7830 (1986).

[46] A. E. Böhmer, F. Hardy, F. Eilers, D. Ernst, P. Adelmann, P. Schweiss, T. Wolf, and C. Meingast, Phys. Rev. B **87**, 180505 (2013).

[47] M. Schmidbauer, A. Kwasniewski, and J. Schwarzkopf, Acta. Crystallogr. B **68**, 8 (2012).

[48] T. Zhang, P. Cheng, W.-J. Li, Y.-J. Sun, G. Wang, X.-G. Zhu, K. He, L. Wang, X. Ma, X. Chen, Y. Wang, Y. Liu, H.-Q. Lin, J.-F. Jia, and Q.-K. Xue, Nat. Phys. **6**, 104 (2010).

[49] D. Liu, W. Zhang, D. Mou, J. He, Y.-B. Ou, Q.-Y. Wang, Z. Li, L. Wang, L. Zhao, S. He, Y. Peng, X. Liu, C. Chen, L. Yu, G. Liu, X. Dong, J. Zhang, C. Chen, Z. Xu, J. Hu, X. Chen, X. Ma, Q. Xue, and X. J. Zhou, Nat. Commun. **3**, 931 (2012).

[50] S. He, J. He, W. Zhang, L. Zhao, D. Liu, X. Liu, D. Mou, Y.-B. Ou, Q.-Y. Wang, Z. Li, L. Wang, Y. Peng, Y. Liu, C. Chen, L. Yu, G. Liu, X. Dong, J. Zhang, C. Chen, Z. Xu, X. Chen, X. Ma, Q. Xue, and X. J. Zhou, Nat. Mater. **12**, 605 (2013).

[51] S. Tan, Y. Zhang, M. Xia, Z. Ye, F. Chen, X. Xie, R. Peng, D. Xu, Q. Fan, H. Xu, J. Jiang, T. Zhang, X. Lai, T. Xiang, J. Hu, B. Xie, and D. Feng, Nat. Mater. **12**, 634 (2013).

[52] J. J. Lee, F. T. Schmitt, R. G. Moore, S. Johnston, Y.-T. Cui, W. Li, M. Yi, Z. K. Liu, M. Hashimoto, Y. Zhang, D. H. Lu, T. P. Devereaux, D.-H. Lee, and Z.-X. Shen, Nature **515**, 245 (2014).

[53] R. Peng, H. C. Xu, S. Y. Tan, H. Y. Cao, M. Xia, X. P. Shen, Z. C. Huang, C. H. P. Wen, Q. Song, T. Zhang, B. P. Xie, X. G. Gong, and D. L. Feng, Nat. Commun **5**, 5044 (2014).

[54] W. Zhang, Z. Li, F. Li, H. Zhang, J. Peng, C. Tang, Q. Wang, K. He, X. Chen, L. Wang, X. Ma, and Q.-K. Xue, Phys. Rev. B **89**, 060506 (2014).

[55] R. Peng, X. P. Shen, X. Xie, H. C. Xu, S. Y. Tan, M. Xia, T. Zhang, H. Y. Cao, X. G. Gong, J. P. Hu, B. P. Xie, and D. L. Feng, Phys. Rev. Lett. **112**, 107001 (2014).

[56] W.-H. Zhang, Y. Sun, J.-S. Zhang, F.-S. Li, M.-H. Guo, Y.-F. Zhao, H.-M. Zhang, J.-P. Peng, Y. Xing, H.-C. Wang, T. Fujita, A. Hirata, Z. Li, H. Ding, C.-J. Tang, M. Wang, Q.-Y. Wang, K. He, S.-H. Ji, X. Chen, J.-F. Wang, Z.-C. Xia, L. Li, Y.-Y. Wang, J. Wang, L.-L. Wang, M.-W. Chen, Q.-K. Xue, and X.-C. Ma, Chin. Phys. Lett. **31**, 017401 (2014).

[57] L. Z. Deng, B. Lv, Z. Wu, Y. Y. Xue, W. H. Zhang, F. S. Li, L. L. Wang, X. C. Ma, Q. K. Xue, and C. W. Chu, Phys. Rev. B **90**, 214513 (2014).

[58] Y. Sun, W. Zhang, Y. Xing, F. Li, Y. Zhao, Z. Xia, L. Wang, X. Ma, Q.-K. Xue, and J. Wang, Sci. Rep. **4**, 6040 (2014).

[59] Z. Zhang, Y.-H. Wang, Q. Song, C. Liu, R. Peng, K. Moler, D. Feng, and Y. Wang, Sci. Bull. **60**, 1301 (2015).

[60] Y.-T. Cui, R. G. Moore, A.-M. Zhang, Y. Tian, J. J. Lee, F. T. Schmitt, W.-H. Zhang, W. Li, M. Yi, Z.-K. Liu, M. Hashimoto, Y. Zhang, D.-H. Lu, T. P. Devereaux, L.-L. Wang, X.-C. Ma, Q.-M. Zhang, Q.-K. Xue, D.-H. Lee, and Z.-X. Shen, Phys. Rev. Lett. **114**, 037002 (2015).

[61] Y. C. Tian, W. H. Zhang, F. S. Li, Y. L. Wu, Q. Wu, F. Sun, G. Y. Zhou, L. Wang, X. Ma, Q.-K. Xue, and J. Zhao, Phys. Rev. Lett. **116**, 107001 (2016).

[62] F. Li, H. Ding, C. Tang, J. Peng, Q. Zhang, W. Zhang, G. Zhou, D. Zhang, C.-L. Song, K. He, S. Ji, X. Chen, L. Gu, L. Wang, X.-C. Ma, and Q.-K. Xue, Phys. Rev. B **91**, 220503 (2015).

[63] W. Zhao, C.-Z. Zhang, J. Jiang, J. Moodera, and M. Chan, Bull. Am. Phys. Soc. **61**, B11.00011 (2016).

[64] Y. Zhu, C.-F. Tsai, and H. Wang, Supercond. Sci. Technol. **26**, 025009 (2013).

[65] I. Bozovic and C. Ahn, Nat. Phys. **10**, 892 (2014).

[66] I. Božović, Nat. Phys. **12**, 22 (2016).

[67] Y. Lin, A. E. Becerra-Toledo, F. Silly, K. R. Poeppelmeier, M. R. Castell, and L. D. Marks, Surf. Sci. **605**, L51 (2011).

[68] J. Bang, Z. Li, Y. Y. Sun, A. Samanta, Y. Y. Zhang, W. Zhang, L. Wang, X. Chen, X. Ma, Q.-K. Xue, and S. B. Zhang, Phys. Rev. B **87**, 220503 (2013).

[69] M. Kawasaki, K. Takahashi, T. Maeda, R. Tsuchiya, M. Shinohara, O. Ishiyama, T. Yonezawa, M. Yoshimoto, and H. Koinuma, Science **266**, 1540 (1994).

[70] T. Ohnishi, K. Shibuya, M. Lippmaa, D. Kobayashi, H. Kumigashira, M. Oshima, and H. Koinuma, Appl. Phys. Lett. **85**, 272 (2004).

[71] J. G. Connell, B. J. Isaac, G. B. Ekanayake, D. R. Strachan, and S. S. A. Seo, Appl. Phys. Lett. **101**, 251607 (2012).

[72] T. Berlijn, H.-P. Cheng, P. J. Hirschfeld, and W. Ku, Phys. Rev. B **89**, 020501 (2014).

[73] F. Li, Q. Zhang, C. Tang, C. Liu, J. Shi, C. Nie, G. Zhou, Z. Li, W. Zhang, C.-L. Song, K. He, S. Ji, S. Zhang, L. Gu, L. Wang, X.-C. Ma, and Q.-K. Xue, ArXiv e-prints (2015), arXiv:1512.05203 [cond-mat.supr-con] .

[74] N. Li, Z. Li, H. Ding, S. Ji, X. Chen, and Q.-K. Xue, Appl. Phys. Express **6**, 113101 (2013).

[75] Z. Li, J.-P. Peng, H.-M. Zhang, W.-H. Zhang, H. Ding, P. Deng, K. Chang, C.-L. Song, S.-H. Ji, L. Wang, K. He, X. Chen, Q.-K. Xue, and X.-C. Ma, J. Phys. Condens. Matter **26**, 265002 (2014).

[76] Q. Fan, W. H. Zhang, X. Liu, Y. J. Yan, M. Q. Ren, R. Peng, H. C. Xu, B. P. Xie, J. P. Hu, T. Zhang, and D. L. Feng, Nat. Phys. **11**, 946 (2015).

[77] N. Erdman, K. R. Poeppelmeier, M. Asta, O. Warschkow, D. E. Ellis, and L. D. Marks, Nature **419**, 55 (2002).

[78] R. Herger, P. R. Willmott, O. Bunk, C. M. Schlepütz, B. D. Patterson, and B. Delley, Phys. Rev. Lett. **98**, 076102 (2007).

[79] Y. Zhang, J. J. Lee, R. G. Moore, W. Li, M. Yi, M. Hashimoto, D. H. Lu, T. P. Devereaux, D.-H. Lee, and Z.-X. Shen, ArXiv e-prints (2015), arXiv:1512.06322 [cond-mat.supr-con] .

[80] S. Coh, M. L. Cohen, and S. G. Louie, New J. Phys. **17**, 073027 (2015).

[81] C. Tang, C. Liu, G. Zhou, F. Li, H. Ding, Z. Li, D. Zhang, Z. Li, C. Song, S. Ji, K. He, L. Wang, X. Ma, and Q.-K. Xue, Phys. Rev. B **93**, 020507 (2016).

[82] C. Tang, D. Zhang, Y. Zang, C. Liu, G. Zhou, Z. Li, C. Zheng, X. Hu, C. Song, S. Ji, K. He, X. Chen, L. Wang, X. Ma, and Q.-K. Xue, Phys. Rev. B **92**, 180507 (2015).

[83] C.-L. Song, H.-M. Zhang, Y. Zhong, X.-P. Hu, S.-H. Ji, L. Wang, K. He, X.-C. Ma, and Q.-K. Xue, ArXiv e-prints (2015), arXiv:1511.02007 [cond-mat.supr-con] .

[84] W. Li, Y. Zhang, J. J. Lee, H. Ding, M. Yi, Z. Li, P. Deng, K. Chang, S.-K. Mo, M. Hashimoto, D. H. Lu, X. Chen, R. G. Moore, Q.-K. Xue, and Z.-X. Shen, (2015), arXiv:1509.01892 .

[85] I. I. Mazin, D. J. Singh, M. D. Johannes, and M. H. Du, Phys. Rev. Lett. **101**, 057003 (2008).

[86] K. Kuroki, S. Onari, R. Arita, H. Usui, Y. Tanaka, H. Kontani, and H. Aoki, Phys. Rev. Lett. **101**, 087004 (2008).

[87] S. Onari and H. Kontani, Phys. Rev. Lett. **103**, 177001 (2009).

[88] L. Boeri, O. V. Dolgov, and A. A. Golubov, Phys. Rev. Lett. **101**, 026403 (2008).

[89] H. Oh, S. Coh, and M. L. Cohen, J. Phys. Condens. Matter **27**, 335504 (2015).

[90] N. Choudhury, E. J. Walter, A. I. Kolesnikov, and C.-K. Loong, Phys. Rev. B **77**, 134111 (2008).

[91] Y. Xie, H.-Y. Cao, Y. Zhou, S. Chen, H. Xiang, and X.-G. Gong, Sci. Rep. **5**, 10011 (2015).

[92] Z. Wang, S. McKeown Walker, A. Tamai, Z. Ristic, F. Y. Bruno, A. de la Torre, S. Riccò, N. C. Plumb, M. Shi, P. Hlawenka, J. Sánchez-Barriga, A. Varykhalov, T. K. Kim, M. Hoesch, P. D. C. King, W. Meevasana, U. Diebold, J. Mesot, M. Radovic, and F. Baumberger, ArXiv e-prints (2015), arXiv:1506.01191 [cond-mat.str-el] .

[93] D.-H. Lee, Chin. Phys. B **24**, 117405 (2015).

[94] L. Rademaker, Y. Wang, T. Berlijn, and S. Johnston, New J. Phys. **18**, 022001 (2016).

[95] I. I. Mazin, Nat. Mater. **14**, 755 (2015).

[96] D. Huang, C.-L. Song, T. A. Webb, S. Fang, C.-Z. Chang, J. S. Moodera, E. Kaxiras, and J. E. Hoffman, Phys. Rev. Lett. **115**, 017002 (2015).

[97] X. F. Lu, N. Z. Wang, H. Wu, Y. P. Wu, D. Zhao, X. Z. Zeng, X. G. Luo, T. Wu, W. Bao, G. H. Zhang, F. Q. Huang, Q. Z. Huang, and X. H. Chen, Nat. Mater. **14**, 325 (2015).

[98] L. Zhao, A. Liang, D. Yuan, Y. Hu, D. Liu, J. Huang, S. He, B. Shen, Y. Xu, X. Liu, L. Yu, G. Liu, H. Zhou, Y. Huang, X. Dong, F. Zhou, Z. Zhao, C. Chen, Z. Xu, and X. J. Zhou, ArXiv e-prints (2015), arXiv:1505.06361 [cond-mat.supr-con] .

[99] X. H. Niu, R. Peng, H. C. Xu, Y. J. Yan, J. Jiang, D. F. Xu, T. L. Yu, Q. Song, Z. C. Huang, Y. X. Wang, B. P. Xie, X. F. Lu, N. Z. Wang, X. H. Chen, Z. Sun, and D. L. Feng, Phys. Rev. B **92**, 060504 (2015).

[100] Y. Miyata, K. Nakayama, K. Sugawara, T. Sato, and T. Takahashi, Nat. Mater. **14**, 775 (2015).

[101] C. H. P. Wen, H. C. Xu, C. Chen, Z. C. Huang, Y. J. Pu, Q. Song, B. P. Xie, M. Abdel-Hafiez, D. A. Chareev, A. N. Vasiliev, R. Peng, and D. L. Feng, ArXiv e-prints (2015), arXiv:1508.05848 [cond-mat.supr-con] .

[102] Z. R. Ye, C. F. Zhang, H. L. Ning, W. Li, L. Chen, T. Jia, M. Hashimoto, D. H. Lu, Z.-X. Shen, and Y. Zhang, ArXiv e-prints (2015), arXiv:1512.02526 [cond-mat.supr-con] .

[103] T. M. McQueen, A. J. Williams, P. W. Stephens, J. Tao, Y. Zhu, V. Ksenofontov, F. Casper, C. Felser, and R. J. Cava, Phys. Rev. Lett. **103**, 057002 (2009).

[104] T. Shimojima, Y. Suzuki, T. Sonobe, A. Nakamura, M. Sakano, J. Omachi, K. Yoshioka, M. Kuwata-Gonokami, K. Ono, H. Kumigashira, A. E. Böhmer, F. Hardy, T. Wolf, C. Meingast, H. v. Löhneysen, H. Ikeda, and K. Ishizaka, Phys. Rev. B **90**, 121111 (2014).

[105] K. Nakayama, Y. Miyata, G. N. Phan, T. Sato, Y. Tanabe, T. Urata, K. Tanigaki, and T. Takahashi, Phys. Rev. Lett. **113**, 237001 (2014).

[106] M. D. Watson, T. K. Kim, A. A. Haghighirad, N. R. Davies, A. McCollam, A. Narayanan, S. F. Blake, Y. L. Chen, S. Ghannadzadeh, A. J. Schofield, M. Hoesch, C. Meingast, T. Wolf, and A. I. Coldea, Phys. Rev. B **91**, 155106 (2015).

[107] P. Zhang, T. Qian, P. Richard, X. P. Wang, H. Miao, B. Q. Lv, B. B. Fu, T. Wolf, C. Meingast, X. X. Wu, Z. Q. Wang, J. P. Hu, and H. Ding, Phys. Rev. B **91**, 214503 (2015).

[108] Y. Zhang, M. Yi, Z.-K. Liu, W. Li, J. J. Lee, R. G. Moore, M. Hashimoto, N. Masamichi, H. Eisaki, S. K. Mo, Z. Hussain, T. P. Devereaux, Z.-X. Shen, and D. H. Lu, (2015), arXiv:1503.01556 .

[109] M. C. Rahn, R. A. Ewings, S. J. Sedlmaier, S. J. Clarke, and A. T. Boothroyd, Phys. Rev. B **91**, 180501 (2015).

[110] Q. Wang, Y. Shen, B. Pan, Y. Hao, M. Ma, F. Zhou, P. Steffens, K. Schmalzl, T. R. Forrest, M. Abdel-Hafiez, X. Chen, D. A. Chareev, A. N. Vasiliev, P. Bourges, Y. Sidis, H. Cao, and J. Zhao, Nat. Mater. **15** (2015).

[111] Q. Wang, Y. Shen, B. Pan, X. Zhang, K. Ikeuchi, K. Iida, A. D. Christianson, H. C. Walker, D. T. Adroja, M. Abdel-Hafiez, X. Chen, D. A. Chareev, A. N. Vasiliev, and J. Zhao, ArXiv e-prints (2015), arXiv:1511.02485 [cond-mat.supr-con] .

[112] R. M. Fernandes and J. Schmalian, Supercond. Sci. Tech. **25**, 084005 (2012).

[113] H. Yamase and R. Zeyher, Phys. Rev. B **88**, 180502 (2013).

[114] S. Lederer, Y. Schattner, E. Berg, and S. A. Kivelson, Phys. Rev. Lett. **114**, 097001 (2015).

[115] E. P. Rosenthal, E. F. Andrade, C. J. Arguello, R. M. Fernandes, L. Y. Xing, X. C. Wang, C. Q. Jin, A. J. Millis, and A. N. Pasupathy, Nat. Phys. **10**, 225 (2014).

[116] U. R. Singh, S. C. White, S. Schmaus, V. Tsurkan, A. Loidl, J. Deisenhofer, and P. Wahl, Sci. Adv. **1** (2015).

[117] D. Huang, T. A. Webb, S. Fang, C.-L. Song, C.-Z. Chang, J. S. Moodera, E. Kaxiras, and J. E. Hoffman, ArXiv e-prints (2015), arXiv:1509.07110 [cond-mat.supr-con] .

[118] J. K. Glasbrenner, I. I. Mazin, H. O. Jeschke, P. J. Hirschfeld, R. M. Fernandes, and R. Valentí, Nat. Phys. **11**, 953 (2015).

[119] F. Wang, S. A. Kivelson, and D.-h. Lee, Nat. Phys. **11**, 959 (2015).

[120] P. J. Hirschfeld, M. M. Korshunov, and I. I. Mazin, Rep. Prog. Phys. **74**, 124508 (2011).

[121] W. Ku, T. Berlijn, and C.-C. Lee, Phys. Rev. Lett. **104**, 216401 (2010).

[122] C.-H. Lin, T. Berlijn, L. Wang, C.-C. Lee, W.-G. Yin, and W. Ku, Phys. Rev. Lett. **107**, 257001 (2011).

[123] S. Chi, S. Johnston, G. Levy, S. Grothe, R. Szedlak, B. Ludbrook, R. Liang, P. Dosanjh, S. A. Burke, A. Damascelli, D. A. Bonn, W. N. Hardy, and Y. Pennec, Phys. Rev. B **89**, 104522 (2014).

[124] I. I. Mazin, Phys. Rev. B **84**, 024529 (2011).

[125] T. A. Maier, S. Graser, P. J. Hirschfeld, and D. J. Scalapino, Phys. Rev. B **83**, 100515 (2011).

[126] A. Kreisel, Y. Wang, T. A. Maier, P. J. Hirschfeld, and D. J. Scalapino, Phys. Rev. B **88**, 094522 (2013).

[127] X. Chen, S. Maiti, A. Linscheid, and P. J. Hirschfeld, Phys. Rev. B **92**, 224514 (2015).

[128] P. J. Hirschfeld, D. Altenfeld, I. Eremin, and I. I. Mazin, Phys. Rev. B **92**, 184513 (2015).

[129] T. Pereg-Barnea and M. Franz, Phys. Rev. B **78**, 020509 (2008).

[130] R. Beaird, I. Vekhter, and J.-X. Zhu, Phys. Rev. B **86**, 140507 (2012).

[131] Z. R. Ye, Y. Zhang, F. Chen, M. Xu, J. Jiang, X. H. Niu, C. H. P. Wen, L. Y. Xing, X. C. Wang, C. Q. Jin, B. P. Xie, and D. L. Feng, Phys. Rev. X **4**, 031041 (2014).

[132] Z.-X. Li, F. Wang, H. Yao, and D.-H. Lee, ArXiv e-prints arXiv:1512.06179 [cond-mat.supr-con] .

[133] P. T. Dumitrescu, M. Serbyn, R. T. Scalettar, and A. Vishwanath, ArXiv e-prints (2015), arXiv:1512.08523 [cond-mat.supr-con] .

[134] H. Miao, T. Qian, X. Shi, P. Richard, T. K. Kim, M. Hoesch, L. Y. Xing, X.-C. Wang, C.-Q. Jin, J.-P. Hu, and H. Ding, Nat. Commun. **6**, 6056 (2015).

[135] P. Zhang, P. Richard, N. Xu, Y.-M. Xu, J. Ma, T. Qian, A. V. Fedorov, J. D. Denlinger, G. D. Gu, and H. Ding, Appl. Phys. Lett. **105**, 172601 (2014).

[136] Z.-H. Liu, P. Richard, N. Xu, G. Xu, Y. Li, X.-C. Fang, L.-L. Jia, G.-F. Chen, D.-M. Wang, J.-B. He, T. Qian, J.-P. Hu, H. Ding, and S.-C. Wang, Phys. Rev. Lett. **109**, 037003 (2012).

[137] Y. J. Song, J. B. Hong, B. H. Min, and Y. S. Kwon, J. Korean. Phys. Soc. **59**, 312 (2011).

[138] I. I. Mazin, Nature **464**, 183 (2010).

[139] F. Wang, F. Yang, M. Gao, Z.-Y. Lu, T. Xiang, and D.-H. Lee, Europhys. Lett. **93**, 57003 (2011).

[140] Y.-Y. Xiang, F. Wang, D. Wang, Q.-H. Wang, and D.-H. Lee, Phys. Rev. B **86**, 134508 (2012).

[141] J. E. Hoffman, K. McElroy, D.-H. Lee, K. Lang, H. Eisaki, S. Uchida, and J. C. Davis, Science **297**, 1148 (2002).

[142] J. A. Stroscio, R. M. Feenstra, and A. P. Fein, Phys. Rev. Lett. **57**, 2579 (1986).

[143] U. Chatterjee, M. Shi, A. Kaminski, A. Kanigel, H. Fretwell, K. Terashima, T. Takahashi, S. Rosenkranz, Z. Li, H. Raffy, A. Santander-Syro, K. Kadowaki, M. Norman, M. Randeria, and J. Campuzano, Phys. Rev. Lett. **96**, 107006 (2006).

[144] M. J. Lawler, K. Fujita, J. Lee, A. R. Schmidt, Y. Kohsaka, C. K. Kim, H. Eisaki, S. Uchida, J. C. Davis, J. P. Sethna, and E.-A. Kim, Nature **466**, 347 (2010).

[145] W.-C. Lee, C. Wu, D. P. Arovas, and S.-C. Zhang, Phys. Rev. B **80**, 245439 (2009).

[146] I. Zeljkovic, Y. Okada, C.-Y. Huang, R. Sankar, D. Walkup, W. Zhou, M. Serbyn, F. Chou, W.-F. Tsai, H. Lin, A. Bansil, L. Fu, and M. Z. Hasan, Nat. Phys. **10**, 572 (2014).

[147] C. Zhang, Y. Chen, A. Johnson, M.-Y. Li, J.-K. Huang, L.-J. Li, and C.-K. Shih, arXiv:1412.8487v1 .

[148] Y. Zhang, V. W. Brar, F. Wang, C. Girit, Y. Yayon, M. Panlasigui, A. Zettl, and M. F. Crommie, Nat. Phys. **4**, 627 (2008).

[149] J. Tersoff and D. R. Hamann, Phys. Rev. Lett. **50**, 1998 (1983).

[150] J. P. Perdew, K. Burke, and M. Ernzerhof, Phys. Rev. Lett. **77**, 3865 (1996).

[151] G. Kresse and J. Furthmuller, Phys. Rev. B **54**, 11169 (1996).

[152] G. Kresse and J. Furthmiiller, Comp. Mater. Sci. **6**, 15 (1996).

[153] M. Methfessel and A. T. Paxton, Phys. Rev. B **40**, 3616 (1989).

[154] C.-Y. Moon and H. J. Choi, Phys. Rev. Lett. **104**, 057003 (2010).

[155] S. Medvedev, T. M. McQueen, I. A. Troyan, T. Palasyuk, M. I. Eremets, R. J. Cava, S. Naghavi, F. Casper, V. Ksenofontov, G. Wortmann, and C. Felser, Nat. Mater. **8**, 630 (2009).

[156] X. Wu, S. Qin, Y. Liang, H. Fan, and J. Hu, arXiv:1412.3375v1 .

[157] I. Zeljkovic, E. J. Main, T. L. Williams, M. C. Boyer, K. Chatterjee, W. D. Wise, Y. Yin, M. Zech, A. Pivonka, T. Kondo, T. Takeuchi, H. Ikuta, J. Wen, Z. Xu, G. D. Gu, E. W. Hudson, and J. E. Hoffman, Nat. Mater. **11**, 585 (2012).

[158] R. M. Fernandes, A. V. Chubukov, and J. Schmalian, Nat. Phys. **10**, 97 (2014).

[159] T.-M. Chuang, M. P. Allan, J. Lee, Y. Xie, N. Ni, S. L. Bud'ko, G. S. Boebinger, P. C. Canfield, and J. C. Davis, Science **327**, 181 (2010).

[160] M. P. Allan, T.-M. Chuang, F. Massee, Y. Xie, N. Ni, S. L. Bud'ko, G. S. Boebinger, Q. Wang, D. S. Dessau, P. C. Canfield, M. S. Golden, and J. C. Davis, Nat. Phys. **9**, 220 (2013).

[161] X. Zhou, C. Ye, P. Cai, X. Wang, X. Chen, and Y. Wang, Phys. Rev. Lett. **106**, 087001 (2011).

[162] P. Cai, W. Ruan, X. Zhou, C. Ye, A. Wang, X. Chen, D.-H. Lee, and Y. Wang, Phys. Rev. Lett. **112**, 127001 (2014).

[163] S. Kasahara, T. Watashige, T. Hanaguri, Y. Kohsaka, T. Yamashita, Y. Shimoyama, Y. Mizukami, R. Endo, H. Ikeda, K. Aoyama, T. Terashima, S. Uji, T. Wolf, H. von Löhneysen, T. Shibauchi, and Y. Matsuda, PNAS **111**, 16309 (2014).

[164] L. Moreschini, P.-H. Lin, C.-H. Lin, W. Ku, D. Innocenti, Y. J. Chang, A. L. Walter, K. S. Kim, V. Brouet, K.-W. Yeh, M.-K. Wu, E. Rotenberg, A. Bostwick, and M. Grioni, Phys. Rev. Lett. **112**, 087602 (2014).

[165] C.-H. Lin, C.-P. Chou, W.-G. Yin, and W. Ku, ArXiv e-prints (2014), arXiv:1403.3687 [cond-mat.supr-con] .

[166] Y. Wang, T. Berlijn, P. J. Hirschfeld, D. J. Scalapino, and T. A. Maier, Phys. Rev. Lett. **114**, 107002 (2015).

[167] K. Jiang, J. Hu, H. Ding, and Z. Wang, (2015), arXiv:1508.00588 .

[168] P. A. Lee and X.-G. Wen, Phys. Rev. B **78**, 144517 (2008).

[169] W. Lv and P. Phillips, Phys. Rev. B **84**, 174512 (2011).

[170] S. Graser, T. A. Maier, P. J. Hirschfeld, and D. J. Scalapino, New J. Phys. **11**, 025016 (2009).

[171] A. Kreisel, P. Choubey, T. Berlijn, W. Ku, B. M. Andersen, and P. J. Hirschfeld, Phys. Rev. Lett. **114**, 217002 (2015).

[172] S. Mukherjee, A. Kreisel, P. J. Hirschfeld, and B. M. Andersen, Phys. Rev. Lett. **115**, 026402 (2015).

[173] H. Eschrig and K. Koepernik, Phys. Rev. B **80**, 104503 (2009).

[174] S. Grothe, S. Chi, P. Dosanjh, R. Liang, W. N. Hardy, S. A. Burke, D. A. Bonn, and Y. Pennec, Phys. Rev. B **86**, 174503 (2012).

[175] T. Hanaguri, K. Kitagawa, K. Matsubayashi, Y. Mazaki, Y. Uwatoko, and H. Takagi, Phys. Rev. B **85**, 214505 (2012).

[176] A. V. Chubukov, R. M. Fernandes, and J. Schmalian, Phys. Rev. B **91**, 201105 (2015).

[177] R. Yu and Q. Si, Phys. Rev. Lett. **115**, 116401 (2015).

[178] Y. Kamihara, T. Watanabe, M. Hirano, and H. Hosono, J. Am. Chem. Soc **130**, 3296 (2008).

[179] K.-W. Yeh, T.-W. Huang, Y. lin Huang, T.-K. Chen, F.-C. Hsu, P. M. Wu, Y.-C. Lee, Y.-Y. Chu, C.-L. Chen, J.-Y. Luo, D.-C. Yan, and M.-K. Wu, Europhys. Lett. **84**, 37002 (2008).

[180] Y. Yin, M. Zech, T. L. Williams, X. F. Wang, G. Wu, X. H. Chen, and J. E. Hoffman, Phys. Rev. Lett. **102**, 097002 (2009).

[181] C.-L. Song, Y. Yin, M. Zech, T. Williams, M. M. Yee, G.-F. Chen, J.-L. Luo, N.-L. Wang, E. W. Hudson, and J. E. Hoffman, Phys. Rev. B **87**, 214519 (2013).

[182] A. V. Balatsky, I. Vekhter, and J.-X. Zhu, Rev. Mod. Phys. **78**, 373 (2006).

[183] S. Kashiwaya and Y. Tanaka, Rep. Prog. Phys. **63**, 1641 (2000).

[184] P. Sessi, J. R. Guest, M. Bode, and N. P. Guisinger, Nano Lett. **9**, 4343 (2009).

[185] B. Weber, S. Mahapatra, H. Ryu, S. Lee, A. Fuhrer, T. C. G. Reusch, D. L. Thompson, W. C. T. Lee, G. Klimeck, L. C. L. Hollenberg, and M. Y. Simmons, Science **335**, 64 (2012).

[186] D. Kitchen, A. Richardella, J.-M. Tang, M. E. Flatté, and A. Yazdani, Nature **442**, 436 (2006).

[187] C.-L. Song, Y.-L. Wang, Y.-P. Jiang, L. Wang, K. He, X. Chen, J. E. Hoffman, X.-C. Ma, and Q.-K. Xue, Phys. Rev. Lett. **109**, 137004 (2012).

[188] *Evaporation Guide for the Elements*, Oxford Vacuum Science (2008).

[189] T. Watashige, Y. Tsutsumi, T. Hanaguri, Y. Kohsaka, S. Kasahara, A. Furusaki, M. Sigrist, C. Meingast, T. Wolf, H. v. Löhneysen, T. Shibauchi, and Y. Matsuda, Phys. Rev. X **5**, 031022 (2015).

[190] Z. Du, X. Yang, H. Lin, D. Fang, G. Du, J. Xing, H. Yang, X. Zhu, and H.-H. Wen, ArXiv e-prints (2015), arXiv:1506.04645 [cond-mat.supr-con] .

[191] Y. J. Yan, W. H. Zhang, M. Q. Ren, X. Liu, X. F. Lu, N. Z. Wang, X. H. Niu, Q. Fan, J. Miao, R. Tao, B. P. Xie, X. H. Chen, T. Zhang, and D. L. Feng, ArXiv e-prints (2015), arXiv:1507.02577 [cond-mat.supr-con] .

[192] S. Grimme, J. Comput. Chem. **27**, 1787 (2006).

[193] F. Ricci and G. Profeta, Phys. Rev. B **87**, 184105 (2013).

[194] H. Okabe, N. Takeshita, K. Horigane, T. Muranaka, and J. Akimitsu, Phys. Rev. B **81**, 205119 (2010).

[195] C. G. Morgan, P. Kratzer, and M. Scheffler, Phys. Rev. Lett. **82**, 4886 (1999).

[196] P. Choubey, T. Berlijn, A. Kreisel, C. Cao, and P. J. Hirschfeld, Phys. Rev. B **90**, 134520 (2014).

[197] P. E. Blöchl, O. Jepsen, and O. K. Andersen, Phys. Rev. B **49**, 16223 (1994).

[198] G. Mills, H. Jónsson, and G. K. Schenter, Surf. Sci. **324**, 305 (1995).

[199] H. Jónsson, G. Mills, and K. W. Jacobsen, in *Classical and Quantum Dynamics in Condensed Phase Simulations*, edited by B. J. Berne, G. Ciccotti, and D. F. Coker (World Scientific, 1998) p. 385.

[200] G. H. Vineyard, J. Phys. Chem. Solids **3**, 121 (1957).

[201] K. C. Pandey and E. Kaxiras, Phys. Rev. Lett. **66**, 915 (1991).

[202] T.-K. Chen, C.-C. Chang, H.-H. Chang, A.-H. Fang, C.-H. Wang, W.-H. Chao, C.-M. Tseng, Y.-C. Lee, Y.-R. Wu, M.-H. Wen, H.-Y. Tang, F.-R. Chen, M.-J. Wang, M.-K. Wu, and D. Van Dyck, Proc. Natl. Acad. Sci. **111**, 63 (2014).

[203] J. Guo, S. Jin, G. Wang, S. Wang, K. Zhu, T. Zhou, M. He, and X. Chen, Phys. Rev. B **82**, 180520 (2010).

[204] A. F. Wang, J. J. Ying, Y. J. Yan, R. H. Liu, X. G. Luo, Z. Y. Li, X. F. Wang, M. Zhang, G. J. Ye, P. Cheng, Z. J. Xiang, and X. H. Chen, Phys. Rev. B **83**, 060512 (2011).

[205] Z. Wang, Y. J. Song, H. L. Shi, Z. W. Wang, Z. Chen, H. F. Tian, G. F. Chen, J. G. Guo, H. X. Yang, and J. Q. Li, Phys. Rev. B **83**, 140505 (2011).

[206] A. Ricci, N. Poccia, G. Campi, B. Joseph, G. Arrighetti, L. Barba, M. Reynolds, M. Burghammer, H. Takeya, Y. Mizuguchi, Y. Takano, M. Colapietro, N. L. Saini, and A. Bianconi, Phys. Rev. B **84**, 060511 (2011).

[207] W. Li, H. Ding, P. Deng, K. Chang, C. Song, K. He, L. Wang, X. Ma, J.-p. Hu, X. Chen, and Q.-k. Xue, Nat. Phys. **8**, 126 (2011).

[208] W. Li, H. Ding, Z. Li, P. Deng, K. Chang, K. He, S. Ji, L. Wang, X. Ma, J.-P. Hu, X. Chen, and Q.-K. Xue, Phys. Rev. Lett. **109**, 057003 (2012).

[209] X. Ding, D. Fang, Z. Wang, H. Yang, J. Liu, Q. Deng, G. Ma, C. Meng, Y. Hu, and H.-H. Wen, Nat. Commun. **4**, 1897 (2013).

[210] K. Reuter and M. Scheffler, Phys. Rev. B **65**, 035406 (2001).

[211] Åke Olin, B. Noläng, L.-O. Öhman, E. Osadchii, and E. Rosén, *Chemical Thermodynamics of Selenium*, Vol. 7 (Nuclear Energy Agency, 2005).

[212] P. Kratzer, C. G. Morgan, and M. Scheffler, Phys. Rev. B **59**, 15246 (1999).

[213] J. Tersoff, M. D. Johnson, and B. G. Orr, Phys. Rev. Lett. **78**, 282 (1997).

[214] J. Maletz, V. B. Zabolotnyy, D. V. Evtushinsky, S. Thirupathaiah, A. U. B. Wolter, L. Harnagea, A. N. Yaresko, A. N. Vasiliev, D. A. Chareev, A. E. Böhmer, F. Hardy, T. Wolf, C. Meingast, E. D. L. Rienks, B. Büchner, and S. V. Borisenko, Phys. Rev. B **89**, 220506 (2014).

[215] E. Kaxiras and K. C. Pandey, Phys. Rev. B **47**, 1659 (1993)